

Exact Quantum Dynamical Calculations of Rovibrational Spectra Using Massively  
Parallel Computers

by

Corey A. Petty, B.S.

A Dissertation

In

CHEMISTRY

Submitted to the Graduate Faculty  
of Texas Tech University in  
Partial Fulfillment of  
the Requirements for  
the Degree of

DOCTOR OF PHILOSOPHY

Dr. L. William (Bill) Poirier  
Chairperson of the Committee

Dr. Jorge A. Morales

Dr. Thomas L. Gibson

Dr. Mark Sheridan  
Dean of the Graduate School

August 2014

©2014, Corey A. Petty

## ACKNOWLEDGEMENTS

This work was largely supported by both a research grant (CHE-1012662) and a CRIF MU instrumentation grant (CHE-0840493) from the National Science Foundation. Additional support from The Robert A. Welch Foundation (D-1523) is also acknowledged, as well as from the Office of Advanced Scientific Computing Research, Mathematical, Information, and Computational Sciences Division of the US Department of Energy under contract DE-FG03-02ER25534. I also gratefully acknowledge the following entities for providing access and technical support for their respective computing clusters: the Texas Tech University High Performance Computing Center, for use of the Hrothgar facility; NSF CHE-0840493 and the Texas Tech University Department of Chemistry and Biochemistry, for use of the Robinson cluster; Carlos Rosales-Fernandez and the Texas Advanced Computing Center, for use of the LoneStar facility. Calculations presented in this dissertation were performed using the *ScalIT* suite of parallel codes.

Personally, I would like to thank my friends and family for creating an environment of love and support to fuel me. I would also like to thank my group members for the engaging conversations that helped me grasp the difficult concepts I have worked with. I would like to thank my advisor, Dr. Bill Poirier, for his countless hours of tutelage and guidance. Without his endless patience, I would have been hard pressed to complete this achievement. He is truly the perfect model of an advisor. Finally, I would like to thank my wife, Erin Oliver Petty, for taking care of the day-to-day minutia during my late hours of work, without an iota of irritation or complaint.

## TABLE OF CONTENTS

Acknowledgements . . . . .	ii
Abstract . . . . .	v
List of Tables . . . . .	vi
List of Figures . . . . .	vii
Acronyms . . . . .	viii
Glossary . . . . .	ix
1. Introduction . . . . .	1
1.1 Overview of Research Conducted . . . . .	2
1.2 Motivation . . . . .	3
2. Rovibrational Theory and Background . . . . .	5
3. Methods and Codes . . . . .	8
3.1 Phase Space Optimized Discrete Variable Representation . . . . .	9
3.2 The <b>A</b> -matrix Form . . . . .	11
3.3 Sparse Iterative Solvers . . . . .	12
3.4 Preconditioned Inexact Spectral Transform (PIST) . . . . .	13
3.4.1 Spectral Transform . . . . .	13
3.4.2 Optimal Separable Basis (OSB)+Wyatt Preconditioning . . . . .	14
3.5 Parallelization . . . . .	16
4. High Lying Rovibrational States of HO <sub>2</sub> . . . . .	18
4.1 Introduction . . . . .	18
4.2 Rovibrational Calculations for Triatomic AB <sub>2</sub> Molecules . . . . .	23
4.3 <i>J</i> -shifting Strategies . . . . .	25
4.4 Computational Details . . . . .	27
4.5 Results and Discussion . . . . .	32
4.5.1 Rovibrational Eigenstates . . . . .	32
4.5.2 <i>J</i> -shifting Results for <i>J</i> = 50 . . . . .	36
4.5.3 Wavefunction Analysis of a <i>J</i> = 120 Rovibrational Bound State . . . . .	45
4.6 Summary and Concluding Remarks . . . . .	49
5. <i>J</i> -shifting Strategies as Applied to the HO <sub>2</sub> Molecule . . . . .	56

5.1	Introduction . . . . .	56
5.2	Theory and Background . . . . .	57
5.3	Results and Discussion . . . . .	61
5.4	Summary and Concluding Remarks . . . . .	65
6.	Vibrational States of the Neon Tetramer . . . . .	75
6.1	Introduction . . . . .	75
6.2	Theory and Background . . . . .	76
6.2.1	Rovibrational Calculations for Tetra-atomic $A_4$ Molecules .	76
6.2.2	Symmetry . . . . .	78
6.3	Computational Details and Potential Energy Surface . . . . .	80
6.4	Results and Discussion . . . . .	83
6.5	Summary and Concluding Remarks . . . . .	84
7.	Concluding Remarks . . . . .	86
	References . . . . .	88
	Appendices . . . . .	94
A.	Standalone Guide to Using <i>ScalIT</i> . . . . .	95
A.1	Introduction . . . . .	95
A.2	The “ <b>A</b> Matrix” Form, and <i>ScalIT</i> Methodology . . . . .	95
A.3	Using <i>ScalIT</i> . . . . .	99
A.4	Applications . . . . .	101
A.5	Conclusion . . . . .	103

## ABSTRACT

We perform highly accurate rovibrational spectra calculations on the HO<sub>2</sub> and Ne<sub>4</sub> systems using *ScalIT*, an exact quantum dynamics software suite designed to perform such calculations across a massive number of computer processors in a straightforward manner. HO<sub>2</sub> calculations are performed up to the dissociation threshold, corresponding to a total angular momentum value,  $J \leq 130$ . A series of theory-based  $J$ -shifting (JS) schemes are also introduced and applied to a representative set of  $J$  values of HO<sub>2</sub>. The results are compared to both the previously mentioned exact values calculated, and experimentally derived vibrational-state-dependent JS results [J. Phys. Chem. A. **110**, 3246, (2006)]. One of the introduced methods, the modified effective potential (modEP) scheme, outperforms all others in all regimes, and appears to be resistant to Coriolis-coupling effects. The modEP scheme is used as an analysis tool to shed structural insight on the dynamics of Coriolis-coupled eigenstate wave functions of HO<sub>2</sub>. The vibrational spectrum for Ne<sub>4</sub> is calculated for all possible permutation inversion symmetries, and the physically real states are identified.

## LIST OF TABLES

4.1	HO <sub>2</sub> calculation parameters . . . . .	28
4.2	HO <sub>2</sub> basis sizes . . . . .	29
4.3	HO <sub>2</sub> $J = 10$ states and comparison with previous results . . . . .	34
4.4	HO <sub>2</sub> $J = 20$ states and comparison with previous results . . . . .	35
4.5	HO <sub>2</sub> $J = 30$ states and comparison with previous results . . . . .	37
4.6	HO <sub>2</sub> $J = 40$ states and comparison with previous results . . . . .	38
4.7	HO <sub>2</sub> $J = 50$ even parity states with $J$ -shifting (JS) comparison . . . . .	39
4.8	HO <sub>2</sub> $J = 50$ odd parity states and comparison with previous results . . . . .	40
4.9	Lowest-lying 125 rovibrational states of $J = 50$ HO <sub>2</sub> with even parity . . . . .	53
4.10	HO <sub>2</sub> $J = 60, 70, 80$ states . . . . .	54
4.11	HO <sub>2</sub> $J = 90, 100, 110, 120$ states . . . . .	55
5.1	Table summarizing the various attributes of each JS method . . . . .	62
5.2	RMS errors in JS methods for HO <sub>2</sub> . . . . .	67
5.3	$J = 10$ HO <sub>2</sub> JS method comparison . . . . .	68
5.4	$J = 50$ HO <sub>2</sub> JS method comparison . . . . .	69
5.5	$J = 100$ HO <sub>2</sub> JS method comparison . . . . .	70
6.1	G <sub>4</sub> character table . . . . .	79
6.2	S <sub>4</sub> to G <sub>4</sub> correlation table for identical particle tetra-atomics . . . . .	79
6.3	Lennard-Jones and basis set parameters for Ne <sub>4</sub> calculations . . . . .	81
6.4	Ne <sub>4</sub> vibrational states and symmetry labels . . . . .	85

## LIST OF FIGURES

2.1	Triatomic molecule ABC in Jacobi coordinates. . . . .	5
3.1	<b>ScalIT</b> workflow . . . . .	10
3.2	Pictorial representation of a A-type matrix . . . . .	12
3.3	OSB preconditioning pictorial . . . . .	16
3.4	Block Jacobi diagonalization parallel efficiency . . . . .	17
4.1	Line plot of all $J$ states . . . . .	43
4.2	HO <sub>2</sub> JS error comparison at $J = 50$ with even parity . . . . .	45
4.3	Probability distributions of $K$ for two HO <sub>2</sub> $J = 120$ even parity states	47
4.4	Calculated rotational energy shifts as a function of $K$ for HO <sub>2</sub> $J = 120$ .	48
5.1	Plot of JS errors for HO <sub>2</sub> . . . . .	71
5.2	Plot of $J = 10$ HO <sub>2</sub> JS errors by vibrational band . . . . .	72
5.3	Plot of $J = 50$ HO <sub>2</sub> JS errors by vibrational band . . . . .	73
5.4	Plot of $J = 100$ HO <sub>2</sub> JS errors by vibrational band . . . . .	74
6.1	Diatom–Diatom diagram of a tetra-atomic molecule . . . . .	76
6.2	Effective 1D radial potentials for Ne <sub>4</sub> (or any L-J tetramer) in Jacobi coordinates . . . . .	82
A.1	Model of an AB <sub>2</sub> molecule as described by Jacobi coordinates. . . . .	96
A.2	<b>A</b> matrix form . . . . .	97

## ACRONYMS

- DOF** degree of freedom. 9, 60, 76, 80, 89–91, 96
- DOS** density of states. 14–16, 21, 50, 76, 83, 84, 92, 93, 96, 97
- DVR** Discrete Variable Representation. 9, 11, 27, 28, 30, 82, 89, 93, 94
- HC** helicity conserving. 19, 22, 36, 41–43, 49, 51, 56–58, 60
- JS** *J*-shifting. 18, 19, 22, 23, 25–27, 29, 36, 39, 41–46, 51, 52, 56–74, 86
- OSB** Optimal Separable Basis. 14–16, 92, 94
- OSBW** OSB+Wyatt. 16, 92, 95
- PES** potential energy surface. 9, 20, 21, 26, 27, 29, 32, 41, 48, 50, 51, 57, 59, 60, 75, 80, 93, 94, 96, 97
- PIST** Preconditioned Inexact Spectral Transform. 13, 32, 91, 95
- PSODVR** Phase Space Optimized DVR. 9–11, 25, 27–29, 31, 81, 83, 93, 94, 96
- QD** quantum dynamics. 1–4, 8, 9, 16, 19–22, 50–52, 76, 86
- QMR** quasiminimal residual. 8, 14, 15, 30, 32, 92, 95, 96
- RSD** rotational state dependent. 19, 22, 23, 26, 27, 29, 36, 39, 43–46, 48, 51, 52, 60–62, 65
- VSD** vibrational state dependent. 19, 22, 23, 25, 26, 29, 36, 39, 41, 44, 45, 51, 59–63, 65, 66

## GLOSSARY

**Coriolis coupling** The coupling between rotational and vibrational degrees of freedom, manifested as non-zero elements in the off-diagonal blocks of the molecular Hamiltonian.

**electronic state or electronic structure** Arrangement of electrons with an atom, molecule, or system of molecules, as allowed by the laws of quantum mechanics for fixed energies. Electronic states occur at discrete energies, whose values vary from one molecular geometry to another. This variation gives rise to the potential energy surfaces.

**Householder's** Householder's algorithm is a method for solving a system of linear equations that falls in the "direct" methods category. Such methods require storage of the full matrix into memory and are typically useful for dense matrices.

**internal energy** Molecular energy in a form that is "internal" to the molecule, *i.e.* associated with vibrational and rotational motion rather than translation.

**Krylov subspace methods** A genre of methods in linear algebra for iteratively solving large systems of linear equations for a small number of eigenvalues. These methods avoid matrix-matrix operations, and instead work with the products of successive matrix-vector products, thereby saving on memory requirements and computational effort.

**molecular geometry** The relative positions of the atomic nuclei as situated in three-dimensional physical space, for a molecule or system of molecules, often described by a set of bond lengths and bond angles. The molecular geometry is unaffected by overall spatial translations and rotations. A change in molecular geometry is therefore associated with internal vibrational and rotational motion, and (for a system of molecules) with relative translation and rotation.

**potential energy surface (PES)** Geometric surface on which the potential energy of a set of atomic nuclei in a molecular system is plotted as a function of the coordinates representing the molecular geometries of the system. A given potential energy surface corresponds to a given electronic state, generally varying adiabatically from one molecular geometry to another.

**quantum dynamics** Accounting for the intermolecular and intramolecular motions of quantum states of molecules that occur in the elementary steps of chemical and photophysical change (*e.g.* molecular collisions, photo emission/absorption, activated complex dissociation, etc.) In particular, the motions of atomic nuclei are treated accurately, using the laws of quantum rather than classical mechanics.

**rovibrational states** Refers to the combined vibration-rotation quantum states of a molecule, for which variable excitations in both the rotational and vibrational motions are simultaneously considered, but for which the electronic state is always the same.

**tunneling** Inherently quantum phenomenon in which a chemical reaction can occur even when the total energy is below the transition state barrier value. In this case, the reactants are said to “tunnel” through the barrier to form products. Requires a quantum dynamical treatment, *i.e.* tunneling does not occur at all in classical trajectory simulations.

CHAPTER 1  
INTRODUCTION

Rovibrational states of small molecules are relevant for many practical applications in chemistry, such as spectroscopy, reaction rates, and equilibrium partition functions. Calculation of such quantities depends on highly accurate knowledge of the rovibrational eigenstates and energy levels. In many instances, experimental data is either difficult, or impossible, to obtain; theoretical computation becomes the only means available to acquire said information. Although the advent of modern computing power has made such calculations obtainable for small molecules, the exponential scaling (with system size) of such calculations can lead to extraordinary requirements of computational effort for larger molecules—and even for small molecules, if large rotational excitations are required. This motivates the development of efficient numerical algorithms. Over the years, Poirier and coworkers have developed a set of just such algorithms to perform calculations to an arbitrary degree of accuracy. Moreover, these algorithms have been recently generalized into a set of codes for massively parallel computing platforms, called *ScalIT* (for Scalable Iteration).

Accurate rovibrational spectroscopy calculations require the theory of quantum dynamics (QD) and, in particular, the use of basis sets and matrices to represent the quantum Hamiltonian operators. These matrix representations are then diagonalized to compute eigenstate wavefunctions and energy levels. Due to the inherent large size of multidimensional rovibrational Hamiltonian matrices, direct diagonalization methods tend to be unfeasible, leading one to use sparse matrix techniques instead—In particular, iterative matrix-vector product schemes with preconditioners.<sup>1–4</sup> *ScalIT* accommodates such calculations, but has been written to be even more general and multifaceted; it is capable of being applied to systems outside the realm of rovibrational spectroscopy, such as molecular scattering applications, or indeed, any other eigenvalue or linear solver type application used to solve linear partial differential equations. However, the scope of this dissertation is limited to rovibrational spectroscopy of molecules.

## 1.1 Overview of Research Conducted

The first research project conducted for this dissertation was an exact quantum dynamical calculation of the rovibrational states of the HO<sub>2</sub> molecule, an important radical in combustion chemistry. In particular, all bound vibrational (total angular momentum  $J = 0$ ) states were obtained, as well as selected rovibrational states up to a rotational excitation of  $J = 120$ , nearly the highest value for which bound states exist. Because full Coriolis coupling is employed and because the largest  $J$  value is so high, these calculations are notoriously difficult.<sup>5</sup> Indeed, to the knowledge of the author, exact rovibrational state calculations for HO<sub>2</sub> have never previously been performed beyond  $J = 50$ .<sup>6-9</sup> Yet, we were able to perform these calculations using *ScalIT* at comparatively low computational cost, and to a high degree of accuracy ( $\sim 10^{-6}$  eV). This project will be discussed in Chapter 4.

The HO<sub>2</sub> molecule is known to be “floppy”, meaning its dynamics exhibit strong coupling between rotational and vibrational motion. Often in practice, the vibrational problem is solved exactly and approximations are made to obtain higher rovibrational energies derived from the explicitly computed vibrational eigenenergies. Such a procedure may be legitimate for non-floppy molecules, but can lead to highly inaccurate predictions for floppy molecules. Nevertheless, there is a strong desire to have such approximation methods available, as they greatly reduce computational cost. As the second project of this dissertation, therefore, we have used our exact HO<sub>2</sub> rovibrational state results to assess the accuracy of several widely used approximation methods of this type. We also introduce a new approximation method of our own.<sup>10</sup> This method is introduced in Chapter 4, and then discussed in much further detail in Chapter 5.

The third and final research project of this dissertation encompasses the investigation of the rovibrational spectroscopy of Van der Waals clusters, specifically the neon tetramer (Ne<sub>4</sub>). A previous *ScalIT* study has already provided a comprehensive rovibrational analysis of neon trimer (Ne<sub>3</sub>),<sup>11</sup> though such a study has never previously been performed for Ne<sub>4</sub>. In this dissertation we restrict ourselves to the vibrational states. In future, however, we hope to extend these calculations to the rovibrational states of Ne<sub>4</sub>, as well as to the neon pentamer. Van der Waals clusters provide a challenging test case for exact QD methods, due to their intrinsically floppy

nature and long-range interactions, among other reasons.<sup>12</sup> The broader goal of such research is to yield rovibrational energies of larger Ne clusters than previously studied, which will serve both computational and scientific purposes. Computationally, it will test the scalability of *ScalIT* across massively parallel computing platforms, using the implicit scalable nature of  $\text{Ne}_n$  systems thus establishing the efficacy of *ScalIT* for real world, relevant problems. Scientifically, it will directly address the problem of liquid-solid phase changes in rare gas clusters thus resolving a long-standing debate in the field of cluster science. Chapter 6 will detail this project.

## 1.2 Motivation

Computational techniques have recently seen a great boost in performance with regards to physical applications; this is due to advances in the availability of computational resources. In particular, advances in massively parallel computation are engendering a revolution in the field of computational chemistry. At the same time, the emergence of “black-box” computational chemistry codes has rapidly brought the tools of this field to a much broader range of chemists. One area that has thus far resisted this trend, however, is computational QD. Due to the extreme difficulty of the many body systems intrinsically involved in chemistry, as well as the quantum dynamical properties inherent in their scale, the majority of theoretical chemists use a varying number of approximations to solve dynamical problems. These approximations follow a trend of becoming more crude as the system size and complexity grow and, as such, results from these models may become more and more unreliable. It therefore stands to reason that extending the applicability of exact quantum dynamical calculations deserves attention, because these serve as a reliable rubric for evaluating the approximate methodologies.

Quantum effects have been shown to have great importance for many systems of interest to modern scientists. Tunneling, zero point energies, molecular spectra, resonance lifetimes, and scattering cross sections are important phenomena in chemical applications. This has led to a development of theoretical machinery to handle systems with innate quantum behavior. Although there has been a proliferation of numerical methods being produced throughout the scientific community, exact QD methods have taken a backseat. This is partially due to the exponential scaling of

computational effort with the dimensionality of the system, making such calculations *computationally expensive*. However, this is also due to the *theoretical and algorithmic complexity* that has traditionally characterized such calculations, making them inaccessible to most chemists. Consequently, the most accurate of calculations, which form a standard for comparison, are not being performed. Although theoretically exact QD calculations can be performed to an arbitrary degree of accuracy, in practice, one is limited drastically by the amount of computational resources available. Typically, the size of a current calculations are limited to only a few atoms (3-4). The advent of scalable algorithms takes advantages of the massively parallel computers creating a new horizon for quantum dynamicists, albeit these algorithms must be efficiently implemented if any progress is to be made on this front.

All of these considerations have informed the development of ***ScalIT***, and informed our efforts both to push the limit of system size and/or excitation energy to the limit of our available resources, and also, to make the ***ScalIT*** codes as easy to use as possible for non-experts. In fact, this latter goal underscores what was in reality a fourth research project, engaged in throughout my graduate tenure: simplification of the ***ScalIT*** codes, and clarification and expansion of the ***ScalIT*** documentation.

CHAPTER 2  
ROVIBRATIONAL THEORY AND BACKGROUND

For the sake of simplicity, in this chapter, we will restrict ourselves to only laying the foundation for triatomics. The underlying theory for tetra-atomics is the same, but the added atom adds a substantial amount of practical difficulty, which is to be explained in Chapter 6. The general framework of exact rovibrational calculations can be thought of as a three step process.<sup>13</sup> First, an appropriate coordinate system is chosen; in the case of triatomics, Jacobi coordinates are generally used. An example of a triatomic molecule ABC in Jacobi coordinates can be seen in Figure 2.1. Second, the Hamiltonian must be expressed in the framework of the chosen coordinates and basis set. Third, the Hamiltonian matrix is constructed and diagonalized.

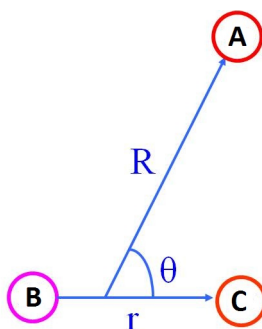


**Figure 2.1:** Triatomic molecule ABC in Jacobi coordinates.

Within the Born-Oppenheimer approximation, the full dimensional rovibrational Hamiltonian for a triatomic molecule ABC in body-fixed reference frame and Jacobi coordinates is expressed as:

$$\hat{H} = -\frac{1}{2\mu_R} \frac{\partial^2}{\partial R^2} + \frac{1}{2\mu_R R^2} (\vec{J} - \vec{j})^2 - \frac{1}{2\mu_r} \frac{\partial^2}{\partial r^2} + \frac{1}{2\mu_r r^2} \vec{j}^2 + V(R, r, \theta) \quad (2.1)$$

where  $\vec{r}$  is the vector between atom B and C,  $\vec{R}$  is the vector between A and the center of mass of BC,  $\theta$  is the angle between vectors  $\vec{R}$  and  $\vec{r}$ ,  $\vec{J}$  is the total angular momentum operator,  $\vec{j}$  is the angular momentum operator associated with vector  $\vec{r}$ ,

and  $\mu_R, \mu_r$  are the reduced masses:

$$\begin{aligned}\mu_r &= \frac{m_B m_C}{m_B + m_C} \\ \mu_R &= \frac{m_A m_{BC}}{m_A + m_{BC}} = \frac{m_A (m_B + m_C)}{m_A + m_B + m_C}\end{aligned}\quad (2.2)$$

In Equation 2.2,  $m_A, m_B$  and  $m_C$  are the masses for atoms A, B, and C, respectively. The  $z$  axis of the body-fixed frame is taken to be either along the vector  $\vec{R}$  or  $\vec{r}$ . Please note that all equations written herein are in atomic units, where  $\hbar = 1$ . The solution of the Hamiltonian of Equation 2.1 yields three good quantum numbers:  $J$ , the total angular momentum,  $M$ , the projection of total angular momentum along space-fixed  $Z$  axis, and  $\epsilon$ , the total parity. The first two quantum numbers mentioned are associated with rotational symmetry, whereas the last is associated with inversion symmetry. The wavefunctions for bound rovibrational states can be expanded in a basis with respect to these three good quantum numbers  $(J, M, \epsilon)$  as follows:<sup>9</sup>

$$\Psi^{JM\epsilon}(R, r, \theta; \alpha, \beta, \gamma) = \sum_{v_1, v_2, j, K} C_{v_1, v_2, j, K}^{JM\epsilon} \cdot \phi_{v_1}(R) \cdot \psi_{v_2}(r) \cdot Y_{jK}^{JM\epsilon}(\alpha, \beta, \gamma, \theta) \quad (2.3)$$

where the parity-adapted angular functions  $Y_{jK}^{JM\epsilon}(\alpha, \beta, \gamma, \theta)$  are given as:

$$\begin{aligned}Y_{jK}^{JM\epsilon}(\alpha, \beta, \gamma, \theta) &= \sqrt{\frac{2J+1}{16\pi^2(1+\delta_{K0})}} [D_{KM}^J(\alpha, \beta, \gamma) \cdot \Theta_{j,k}(\theta) + \\ &\quad \epsilon(-1)^J \cdot D_{-KM}^J(\alpha, \beta, \gamma) \cdot \Theta_{j,-K}(\theta)]\end{aligned}\quad (2.4)$$

Here  $D_{KM}^J$  are the usual Wigner rotation matrices,<sup>14</sup>  $\Theta_{j,K}(\theta)$  are the normalized associated Legendre polynomials,  $(\alpha, \beta, \gamma)$  are the Euler angles, and  $K$  is the projection of the total angular momentum along the body-fixed  $z$  axis. Functions  $\phi_{v_1}(R)$  and  $\psi_{v_2}(r)$  in Equation 2.3 are basis functions describing the coordinates  $R$  and  $r$ , respectively.

In this basis representation, we maintain the good quantum numbers  $(J, M, \epsilon)$  for all triatomic molecules. We then generate individual  $(J, M, \epsilon)$  blocks of the matrix representation of the full rovibrational Hamiltonian. However, in some cases there

are additional system dependent symmetries that can also be exploited for further simplification. In the cases of  $A_2B$  and  $A_4$  molecular systems, such as the  $HO_2$  and  $Ne_4$  systems that we will study in detail, the permutation of identical atoms yields further symmetry. This will be defined in detail in Sections 4.2 and 6.2.2 for  $HO_2$  and  $Ne_4$ , respectively.

In general, one chooses the body-fixed  $z$  axis so that  $K$  is an approximately good quantum number. This means that inter- $K$  coupling, known as Coriolis coupling, manifesting as off-diagonal blocks in the Hamiltonian matrix, are small. If this condition is satisfied, it means that vibrational and rotational motions are largely separable, so that the approximations alluded to in Section 1.1 become reasonably accurate. Note that most of the work presented in this dissertation is exact, meaning that all Coriolis coupling is accounted for exactly, and therefore the choice of  $z$  axis does not in principle influence the final computed results. However, in Section 4.3 and Chapter 5 we will be comparing with various approximation methods, for which the choice of  $z$  axis certainly does matter.

CHAPTER 3  
METHODS AND CODES

As the “*ScalIT*” acronym—which stands for “Scalable Iteration”—implies, *ScalIT* is a collection of software modules designed to scale large sparse iterative matrix manipulations across supercomputers with tens or hundreds of thousands of cores. It has primarily been envisioned as a cyberinfrastructure tool for true massively parallel, distributed-memory QD calculations.<sup>1–4</sup> In this context, *ScalIT* represents a very substantive—and notoriously difficult—advance beyond existing small-scale parallelization strategies, which either confine themselves to (essentially trivial) shared-memory parallelization within a single compute node, or apply the  $K$ -block strategy discussed in Section 4.1 and again in more detail in Chapter 5.<sup>15–21</sup>

The *ScalIT* codes are written in Fortran 90 and in level 2 MPI. The modular design renders it relatively easy for code developers to single out individual software components, as needed for specific functionality. Thus, other expert QD users are free to incorporate *ScalIT*'s sparse matrix–vector product routines into their own Lanczos,<sup>22</sup> quasiminimal residual (QMR)<sup>23</sup>, filter diagonalization,<sup>24</sup> or time-dependent wavepacket codes, thereby introducing massively parallel functionality into these other methods. Efforts along these lines are already underway.

On the other hand, an equally important goal of the *ScalIT* project is to bring accurate QD calculations within the purview of the broader chemical dynamics community, who do not necessarily have computational expertise in this area, but are nevertheless desirous of accurate dynamical results. For the benefit of these non-expert users, the *ScalIT* codes were designed to be very easy to use when performing certain standard computations (more so, e.g., than most electronic structure codes)—even as they provide excellent numerical performance (especially vis-à-vis parallel scalability). One such standard computation is the accurate calculation of any or all bound rovibrational eigenstates (energy levels and wavefunctions) for arbitrary triatomic molecules. By now, *ScalIT* has been successfully applied in this “non-expert” fashion to a number of highly challenging triatomic systems,<sup>11;25–27</sup>—including those such as SO<sub>2</sub> and Ar<sub>3</sub> for which all atoms are “heavy.” In all such cases, *ScalIT* has

been able to reliably compute the rovibrational eigenstates to high accuracy, within a reasonable time frame, on modestly-sized computing clusters.

**ScalIT** is split up into three (optionally four) main steps which pragmatically resembles the way one would attack solving a QD problem numerically: (1) Creating Phase Space Optimized DVR (PSODVR) functions from the supplied potential energy surface (PES), (2) constructing the rovibrational Hamiltonian, (3) diagonalizing a window of eigenstates within the spectrum, and (4) optionally constructing plotable wavefunctions from the calculated states. A simple representational workflow can be seen in Figure 3.1. The following sections detail the specific default algorithms associated with the **ScalIT** package.

For the benefit of the prospective non-expert **ScalIT** user—e.g., experimentalists interested in performing their own accurate rovibrational spectroscopy calculations, or *ab initio* practitioners looking to quickly validate triatomic PESs as these undergo development—we present a practical, step-by-step user’s guide in Appendix A.

### 3.1 Phase Space Optimized Discrete Variable Representation

The radial basis functions,  $\phi_{v_1}(R)$  and  $\psi_{v_2}(r)$  in Equation 2.3 are typically represented by a Discrete Variable Representation (DVR) basis set and grid<sup>28;29</sup>. The DVR has seen a lot of popularity among rovibrational calculations in the recent past, which is due to the fact that local operators, *e.g.*, the potential energy, are diagonal in this representation. For multidimensional applications, the DVR is a direct product basis representation which gives rise to a block structured Hamiltonian of a certain kind (to be discussed shortly), with the level of sparsity greatly increasing with dimensionality. A Potential Optimized DVR, which spaces out DVR grid points non-uniformly, can increase the efficiency of the representation—especially the PSODVR, which has been shown to reduce the number of basis functions typically by a factor of 3 per degree of freedom (DOF). However, a substantially greater reduction is observed for long-range attractive systems such as Van der Waals clusters.

PSODVR theory requires that first effective radial potentials are created via the minimization of  $V(R, r, \theta)$  with respect to all other coordinates:

$$V_R(R) = \min[V(R, r, \theta)]_{r, \theta}, \quad V_r(r) = \min[V(R, r, \theta)]_{R, \theta}. \quad (3.1)$$

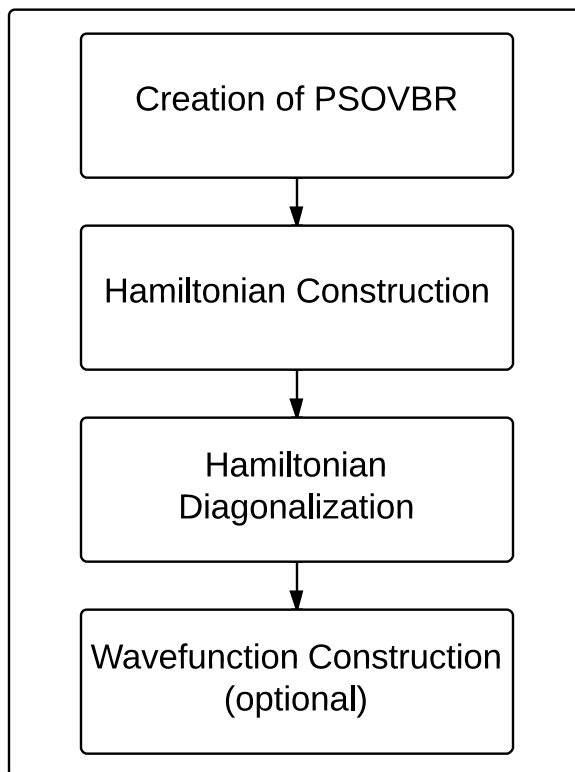


**Figure 3.1:** Simple workflow of the *ScalIT* software suite to elucidate its methodology.

Subsequently, the eigenstates of the effective radial Hamiltonians,

$$\hat{H}_R = -\frac{1}{2\mu_R} \frac{\partial^2}{\partial^2 R} + V_R(R), \quad \hat{H}_r = -\frac{1}{2\mu_r} \frac{\partial^2}{\partial^2 r} + V_r(r), \quad (3.2)$$

are used to construct the optimal PSODVRs. The full (triatomic) rovibrational Hamiltonian of Equation 2.1 is conveniently rewritten as

$$\hat{H} = \hat{H}_R + \hat{H}_r + \frac{1}{2\mu_R R^2} \left( \vec{J} - \vec{j} \right)^2 + \frac{1}{2\mu_r r^2} \vec{j}^2 + V(R, r, \theta) - V_R(R) - V_r(r). \quad (3.3)$$

By default, *ScalIT* computes PSODVR functions from the user-provided effective potentials,  $V_R(R)$  and  $V_r(r)$ , of Equation 3.1. If no effective potentials are provided, sinc-DVR functions are used. Although it is more computationally efficient to use PSODVR functions for the angular space as well, *ScalIT* employs associated Legendre polynomials instead to simplify general usability. These angular functions are then dimensionally combined with the Wigner rotation bases to form into a single “effective angular” coordinate.

### 3.2 The **A**-matrix Form

Such a representation of the rovibrational Hamiltonian, which is the standard for *ScalIT*, represents what is known as a “weakly separable” basis representation. The “weak” indicates the angular kinetic energy’s parametric dependence on the radial values, thus making them not completely independent. The *ScalIT* literature describes this in terms of “inner” and “outer” block (coordinate) levels, where inner blocks do not depend on each other, and outer blocks parametrically depend on the former.<sup>1;30</sup> This creates a matrix that exhibits a certain block-type structure of having diagonal blocks, plus off-diagonal blocks that are themselves diagonal. The diagonal blocks are either dense, or subdivided into smaller blocks in the same fashion as the original matrix. In other words, the diagonal blocks can be self-similar to the whole, much like a fractal. For the purposes of this dissertation, we will call these “**A**-type matrices.” A pictorial representation of this is given in Figure 3.2.

With an increasing number of block levels (closely related to system dimensionality), the sparsity of the matrix increases dramatically, which encourages the employment of sparse matrix techniques to solve such Hamiltonians. On the other hand, fewer block levels allows for more efficient truncation of the representational basis, and therefore smaller matrix sizes. *ScalIT* has the optional capability to dimensionally combine two or more radial coordinates into a single block, creating a single effective coordinate. This gives users additional configurability when attempting to optimize parallel efficiency and matrix size. In practice, 2–4 block levels is found to provide a good balance, regardless of system dimensionality. For the calculations discussed in this dissertation, we do not employ any dimensional combination

other than the default angular dimensional combination, yielding 3 and 4 block levels for HO<sub>2</sub> and Ne<sub>4</sub>, respectively.

### 3.3 Sparse Iterative Solvers

Two linear algebra operations that are routinely manifested in the physics, engineering and applied mathematics fields to simulate partial differential equations are the linear solve and the symmetric eigenvector/eigenvalue problem—represented, respectively, by the following two equations.

$$(\mathbf{H} - \lambda\mathbf{I})^{-1}\vec{x} = \vec{b} \quad (3.4)$$

$$(\mathbf{H} - \lambda\mathbf{I})\vec{x} = 0 \quad (3.5)$$

Here, bold face items are matrices, arrowed items are vectors, and all others are scalars. In the rovibrational context,  $\mathbf{H}$  is the Hamiltonian matrix, which in our chosen representation takes on the form of an  $\mathbf{A}$  matrix,  $\lambda$  is the corresponding eigenenergy, and  $\vec{x}$  is a stationary state or wavefunction of the time independent Schrödinger equation.

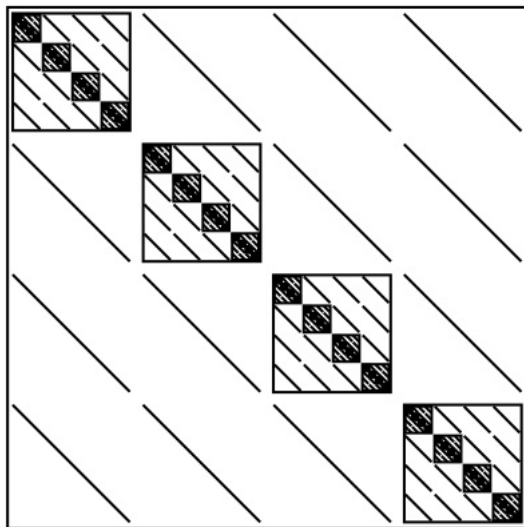


**Figure 3.2:** Pictorial representation of a A-type matrix

There are many numerical methods for solving Equations 3.4 and 3.5. For dense matrices, *direct diagonalization* methods are typically employed, such as Householder's algorithm.<sup>31</sup> The CPU cost scales as  $N^3$  for an  $N \times N$  matrix, which can be unfeasibly expensive for many rovibrational Hamiltonian calculations, for which the matrices can be very large ( $N \geq 10^6$ ). The memory burden can also be unfeasible, as direct methods require full  $N^2$  storage, even for sparse matrices. A matrix is sparse when  $n_{nz} \ll N^2$ , where  $n_{nz}$  is the number of nonzero elements. Fortunately, matrices produced in the manner discussed earlier are sparse. This has led to the motivation to use methods that exploit sparsity. In particular the methods used by *ScalIT* preserve the **A**-matrix form, falling into the category of sparse *iterative* techniques. Sparse iterative techniques require multiple matrix-vector products; the CPU cost scales as  $M \times n_{nz}$ , where  $M$  is the number of iterations (essentially the number of matrix-vector products), in contrast to direct diagonalization methods which scale as  $N^3$ . An efficient sparse iterative method is one that requires a small number of iterations to reach convergence. For rovibrational molecular applications, the number of iterations can be very large;<sup>8;9</sup> To this end, in order to ensure efficiency, we precondition the Hamiltonian in efforts to minimize the number of matrix-vector products.

### 3.4 PIST

In order to compute rovibrational energies, one must diagonalize the Hamiltonian in its basis representation. As previously discussed, because of the sheer size of rovibrational Hamiltonian representations, direct methods such as Householder's algorithm for this eigensolve problem are intractable. The most popular iterative methods for the eigensolve problem of Equation 3.5 are Krylov subspace methods, in particular the Lanczos method.<sup>32</sup> Unfortunately, if one were to naively apply the Lanczos method directly to the rovibrational Hamiltonian, especially at high energies, the number of iterations needed to converge would be comparable to if not exceeding the computational effort required of direct methods.

#### 3.4.1 Spectral Transform

To this end, it has been shown that performing a spectral transform

$$\mathbf{H} \rightarrow F(\mathbf{H}) = (E\mathbf{I} - \mathbf{H})^{-1} \quad (3.6)$$

where  $E$  is a chosen energy shift greatly reduces the number of iterations required for convergence, specifically for highly excited states in the vicinity of the energy  $E$ . The number of iterations for the former is around  $3\times$  excitation number, whereas the latter scales around  $1.7\times$  the number of states in a chosen energy window. For example, the number of Lanczos iterations for the 10,000th excited state would be around 30,000, whereas for the transformed matrix with a window of 10 states, it might be only 17 iterations. The benefit of shifting and inverting is therefore obvious, but in reality, one does not know the new matrix  $(E\mathbf{I} - \mathbf{H})^{-1}$  a priori, and computing it is unfeasible. However, the matrix itself is not needed; all we need to know is how to multiply a vector by it. But this is just the sparse linear solve problem of Equation 3.4 which we implement using yet another iterative algorithm, QMR.<sup>31</sup> QMR has shown to be the superior method (requires fewer iterations) than its competitors, yet in some cases, such as at higher energies where the density of states (DOS) is very high, the number of QMR iterations per Lanczos iteration is exceedingly large. In this case, preconditioning the Hamiltonian is done to drastically reduce the number of QMR iterations.

### 3.4.2 OSB+Wyatt Preconditioning

To precondition a linear system, one finds a matrix  $\mathbf{P}^{-1}$  that when left multiplied onto  $\mathbf{A}$  is close to the identity, i.e.:

$$\mathbf{P}^{-1}\mathbf{A}\vec{x} = \mathbf{P}^{-1}\vec{b} \quad (3.7)$$

$$\vec{x} \approx \mathbf{P}^{-1}\vec{b} \quad (3.8)$$

where  $\mathbf{A} = (\mathbf{H} - \lambda\mathbf{I})^{-1}$  in Equation 3.4. By choosing a  $\mathbf{P}^{-1}$  that makes the product of  $\mathbf{P}^{-1}\mathbf{A}$  close to unity, the number of iterations to reach convergence is greatly reduced that would be necessary to converge  $\mathbf{A}\vec{x} = \vec{b}$ . There are many standard preconditioners that have been developed that work well for sparse matrices, but unfortunately, for the  $\mathbf{A}$ -matrix structure of chemical physics, these have proven to be inefficient. However, it has been shown that for the  $\mathbf{A}$ -matrix Hamiltonians, Optimal Separable

Basis (OSB) preconditioning greatly reduces the number of iterations needed to converge, and more efficiently than any other preconditioner developed thus far to the author’s knowledge.<sup>33</sup>

The OSB method has proven to be an efficient preconditioner for the type of matrices discussed previously—that is to say, a matrix that: (1) can be separated into square blocks of identical size; (2) has diagonal off-diagonal blocks; (3) has identical diagonal blocks, apart from the diagonal elements.<sup>1</sup> A good preconditioner satisfies two requirements: (a) It must be close to the matrix which it is preconditioning, and (b) it must be easily invertible. To this end, we choose a preconditioner of the form  $\mathbf{P} = (E\mathbf{I} - \mathbf{H}_0)$ , where  $\mathbf{H}_0$  represents some approximation to the true Hamiltonian  $\hat{H}$ . Taking advantage of its **A**-type structure, we decompose the full Hamiltonian into  $\mathbf{H} = \mathbf{H}_0 + \mathbf{\Delta}$ , where  $\mathbf{H}_0$  is block diagonal, and the perturbation  $\mathbf{\Delta}$  off-block diagonal.

The OSB method is characterized by minimizing  $\mathbf{\Delta}$ , and subsequently ignoring it as an approximation. The minimization process is performed via the Block Jacobi diagonalization scheme, a block adaptation of the popular Jacobi diagonalization technique,<sup>31</sup> and serves as a core to OSB preconditioning.<sup>33</sup> It is described as a series of orthogonal transformations to the Hamiltonian that minimize the contribution from the off-diagonal-blocks of the matrix. The same process is repeated iteratively to the resultant Hamiltonian’s blocks (for the matrix is now block-diagonal) to the lowest level, producing a block-diagonal matrix of dense blocks. These are then diagonalized, and their eigenstates are used to create the OSB preconditioner,  $\mathbf{H}_0^{\text{OSB}}$ . This resultant matrix satisfies the aforementioned preconditioner requirements, for a diagonal matrix is trivially inverted, and  $\mathbf{H}_0^{\text{OSB}}$  can be considered as a truly optimal choice, in that it is the minimum of  $|\hat{H} - \hat{H}_0|$  with respect to variations in  $\hat{H}_0$ .<sup>33</sup> A pictorial representation of how the OSB preconditioner looks for a single iteration can be seen in Figure 3.3.

In energetic ranges exhibiting a high DOS, even preconditioning using OSB can result in a high number of QMR iterations, due to energy eigenstates being in close proximity to  $E$  of Equation 3.6. To combat this, we combine OSB with an energetically tuned window about the energy  $E$  of off-diagonal matrix elements, referred to as a “Wyatt window” in homage to Wyatt’s suggestion in Ref. [34]. The Wyatt window is composed of the previously ignored off-diagonal elements, denoted  $\mathbf{\Delta}^{\text{OSB}}$ ,

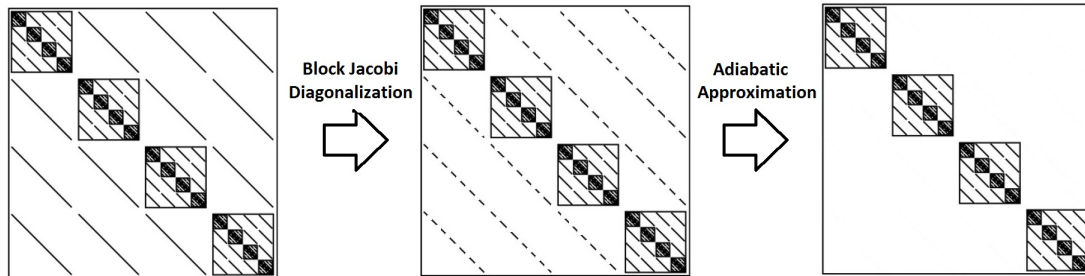


**Figure 3.3:** Pictorial representation of the process of single iteration of OSB preconditioning. Block Jacobi Diagonalization of an  $\mathbf{A}$ -matrix shifts a portion of the off diagonal block elements into the diagonal blocks. Then the off diagonal blocks are then removed. This process is iteratively repeated separately for all remaining diagonal blocks until the lowest layer is reached, resulting in a diagonal matrix.

associated with eigenvalues of  $\mathbf{H}_0^{\text{OSB}}$  close to  $E$ .<sup>5</sup> This combinatory scheme, denoted OSB+Wyatt (OSBW), results in a new preconditioner that is mostly diagonal, except in the vicinity of  $E$  where a small “Wyatt block” exists with dimensions  $W \times W$ , where  $W$  is the number of states that exist inside the Wyatt window. This preconditioner can be seen as an optimal adiabatic approximation of the rovibrational Hamiltonian, and has been shown to drastically reduce the number of required iterations for convergence over an OSB only preconditioning scheme, especially in regimes with high DOS. Note that though the resultant preconditioners discussed are approximations to the true Hamiltonian matrix, the preconditioned QMR calculation is exact.

### 3.5 Parallelization

In order to perform exact QD rovibrational calculations on larger molecules, even with efficient algorithms of the sort described above, it becomes necessary to use massively parallel computers. Furthermore, it is necessary to use efficient algorithms that scale well across these platforms. Where QD calculations are concerned, this turns out to be extremely difficult. However, *ScalIT* is the first QD code to employ parallel algorithms that scale effectively across hundreds and thousands of cores.

These parallel algorithms are rather involved;<sup>1-4</sup> a discussion here would take us too far afield. We do, however, present the results of an earlier isoeficiency study, evaluating the parallel scalability of *ScalIT*. These tests indicated that *ScalIT* has

the potential to scale well up to 10,000 cores. The test was performed on Argonne's Jazz cluster, communicating through myrinet connectivity. The current available resources to the author include Hrothgar (7000 cores), and Robinson (1200 cores), both of which use the faster and more efficient infiniband connectivity. Figure 3.4

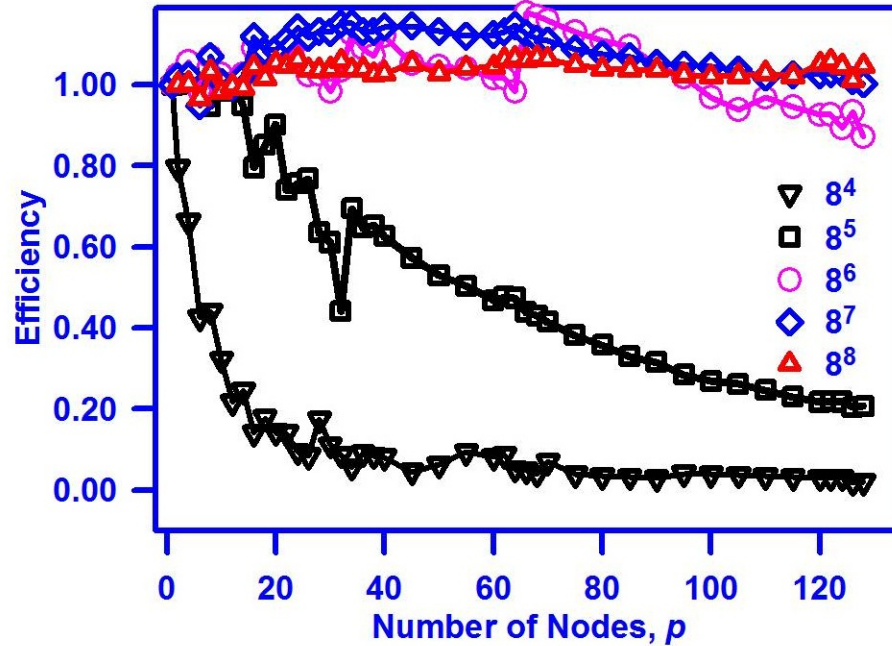


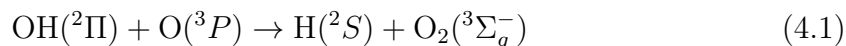
**Figure 3.4:** Plot of Block Jacobi diagonalization parallel efficiency across 128 nodes on Argonne's Jazz cluster. Reprinted with permission from Ref. [1]

shows a plot of the scalability of Block Jacobi diagonalization across 128 cores. Note that as the system size increases, the efficiency tends to flatten and maintain a steady rate. This flatness, along with other trends, is what lead to the conclusions of such large possible scalability.

CHAPTER 4  
HIGH LYING ROVIBRATIONAL STATES OF HO<sub>2</sub><sup>1</sup>

4.1 Introduction

The hydroperoxyl radical, HO<sub>2</sub>, has received very substantial experimental<sup>36–42</sup> and theoretical<sup>6–9;15–18;24;25;43–76</sup> interest over the last two decades. Far from abating over time, this interest seems only to have increased in recent years. Despite the large body of previous work, HO<sub>2</sub> is still regarded as dynamically “elusive,”<sup>69;70</sup> presenting as yet unresolved challenges for rigorous quantum theoretical treatment. Serving as a reaction intermediate, this radical is an extremely key player in combustion chemistry, with the specific reaction



being widely recognized as singularly important.<sup>68;77</sup> Accordingly, rate constants and/or cross sections for reactions such as Equation 4.1 have been extensively assessed, using a variety of means. In this context, the resonance states of HO<sub>2</sub> are obviously very relevant. However, the bound states may also play an important (albeit indirect) role in chemical reactivity, via Lindemann-type (dissociation)/recombination mechanisms, relying on energy transfer through non-reactive third-body collisions. At any rate, the bound vibrational states of HO<sub>2</sub> have been extensively investigated previously, using accurate quantum dynamical techniques<sup>6;15;24;46;47;49;51;55–61;63;67</sup>

On the other hand, it is the *rovibrational* states that are relevant for reactivity—i.e., not just the vibrational states corresponding to total angular momentum  $J = 0$ . Accurate quantum dynamical characterization of rovibrational states is in general much more difficult. In practice, approximations are often used to characterize the rovibrational energy levels, in terms of the rotational quantum numbers  $J$  and  $K$ , and generally based on the assumption of separability of rotation and vibrational motions (and thus additivity of the corresponding energies). In particular, J. M. Bowman is the progenitor of the famous and very useful  $J$ -shifting (JS) [and related adiabatic rotation (AR)] approach,<sup>9;48;53;54;66;71;72;78–83</sup> whereby  $J = 0$  results are com-

<sup>1</sup>This chapter has been reprinted and adapted for this dissertation from Ref. [35]

puted exactly, and used to approximate corresponding  $J > 0$  results via an energy shift associated with the (usually symmetric) rigid rotor kinetic energy. This idea can be applied to the computation of reactive scattering cross sections, as well as rovibrational spectra.

In its simplest incarnation, the rigid rotor constants correspond to a single equilibrium geometry, and are thus taken to be the same for all quantum states. More sophisticated versions of JS allow for *state-dependent* rotational constants. In particular, J. M. Bowman’s AR method leads to a vibrational state dependent (VSD) JS scheme, for which the rotational constant values for a given rovibrational state depend on the corresponding vibrational state<sup>9;48;80;81</sup>—assuming that the latter can be meaningfully assigned. Likewise, in 1998, B. Poirier developed a different, rotational state dependent (RSD) JS scheme, for which the rotational constants themselves depend on  $J$  and  $K$ —thus naturally incorporating centrifugal distortion and other effects.<sup>82;83</sup> RSD JS was shown to provide substantially improved accuracy for the OHCl system, as compared to simple JS—even when  $J$  and  $K$  values are large. Of course, all JS schemes require that a given rovibrational state can be associated with a unique  $K$  value, but in the RSD case (unlike VSD) no additional assignments are required.

As all JS strategies are approximations, it is important to establish under what conditions they are legitimate and/or accurate. In general, they may be expected to break down in the limit of high rotational and/or vibrational excitation, as well as for molecular systems that are inherently floppy. To what extent JS is accurate for HO<sub>2</sub> has been the focus of some investigation over the years.<sup>9;45;48;53;54;58;66;68–72</sup> A related issue, also considered in this same literature, is the importance of Coriolis ( $K$ ) coupling—i.e., how “good” a quantum number  $K$  is. Ignoring Coriolis coupling leads to the helicity conserving (HC) approximation,<sup>17;84;85</sup> which in general can be regarded as less extreme than JS—though to some extent this depends on the choice of embedding (rotational gauge) used to define  $K$ .<sup>48;80;81</sup> Even less extreme—but still an approximation—is the practice of “ $K$  truncation,”<sup>69</sup> whereby some Coriolis coupling is included in the QD calculation, but only out to  $|K| \leq K_{\max} < J$  (whereas an exact rovibrational calculation for a given  $J$  requires all values  $|K| \leq J$ ).

Of course, a completely rigorous characterization of the validity of the above approximations requires comparison with accurate rovibrational QD calculations, as well as a determination of the relevant  $J$  range. Although such calculations have been performed for the HO<sub>2</sub>  $J = 0$  states using a variety of different PESs,<sup>24;43;44;46;47;49;51;55–57</sup> comparatively few exact rovibrational bound state calculations have thus far been performed.<sup>6–9;15;25;64;75</sup> This is despite much evidence<sup>7–9;17;18;48;66;68–72</sup> suggesting that HO<sub>2</sub> exhibits substantial Coriolis coupling and otherwise floppy behavior. An important contributing factor here is the extremely large  $J$  values that are in practice relevant for this system. In the present dissertation, we show that bound rovibrational states exist at least as far as  $J = 120$  (but disappear by  $J = 130$ ). Reactive scattering applications may be expected to require even larger  $J$  values, in order to achieve fully converged results.

When Coriolis coupling is significant,  $K$  truncation may in principle still be used to reduce computational cost. However, previous work suggests that even mild  $K$  truncation may not be so effective for HO<sub>2</sub> at the larger  $J$  values<sup>17;18;69;70;72</sup>—leading, e.g., to an alternate O-OH embedding strategy<sup>69</sup> (as opposed to the usual embedding that adopts the O-O vector as the body-fixed  $z$  axis). Even for very low  $J$  values ( $J \leq 3$ ), the need to include all  $K$  values in previous HO<sub>2</sub> bound rovibrational state calculations necessitated use of a parallel (albeit not *massively* parallel) computing strategy.<sup>6–9;15</sup> Consequently, the largest  $J$  value that has thus far been considered in this context prior to the present work is only  $J = 50$ <sup>9</sup>—which, though “heroic,” is far from the maximum  $J$  value required. In the scattering context, the importance of large- $J$  contributions has been recognized for some time, with gradual but steady progress having been achieved over the years, also with the help of (non-massive) parallel computing.<sup>17;18;63;65–74</sup> In 2008, H. Guo and coworkers performed a  $J = 150$  calculation,<sup>69</sup> but with the rather severe truncation of  $K_{\max} = 20$  (justified via the alternate embedding described above). These authors and others<sup>69;72–74</sup> have since performed fully Coriolis coupled (no  $K$  truncation) QD calculations up to  $J = 84$ , which is particularly impressive inasmuch as state-to-state cross sections are computed, as opposed to more integrated/summed scattering quantities. In any event, this previous work clearly addresses the need to include all  $K$  values in the calculation.

The accuracy achieved in the scattering context is far less than that required in a spectroscopic calculation of rovibrational levels. In this chapter, we present energy levels and wavefunctions for the rovibrational bound states of HO<sub>2</sub>, computed across the entire range of  $J$  values for which these states exist, and a little beyond. These calculations have been performed using “exact” QD—i.e., no approximations beyond Born-Oppenheimer have been applied—including no  $K$  truncation, so that all Coriolis coupling is included explicitly. The results have also been converged to a much higher level of accuracy than observed in previous calculations—i.e., to 10<sup>-6</sup> eV or better. In particular, calculations have been performed for every multiple-of-ten  $J$  value from  $J = 10$  to  $J = 130$ —thus filling an existing gap in the knowledge base, in that no exact  $J > 50$  bound state spectroscopic calculations have ever previously been performed, to the author’s knowledge.

Together with the use of the double many-body expansion (DMBE) IV PES,<sup>44</sup> the focus on multiple-of-ten  $J$  values enables direct comparison with previous bound rovibrational calculations performed by S. Smith and coworkers up to  $J = 50$ , as well as with a recent article from our own group addressing the  $J = 0$ –10 states<sup>25</sup> (hereinafter referred to as “Paper I”). Note that more recent and accurate PESs exist, as described in Section 4.4, but have not been used as extensively as DMBE IV in the context of bound rovibrational states. Of particular interest in the most recent HO<sub>2</sub> literature have been studies addressing the DOS.<sup>64;75</sup> The latter work shows marked DOS differences across the different PESs, particularly at high energies. DMBE IV is found to have the highest DOS of the PESs considered—implying that the exact calculations as presented here would be substantially less computationally expensive, if performed using a more recent PES.

We are not the first to have applied parallel QD techniques to the rovibrational HO<sub>2</sub> system—in fact, the history of the former has “paralleled” calculations of the latter since the earliest days that such techniques were developed.<sup>15–19</sup> The main strategy used—in effect, to assign one  $K$  block to each core or node—is by and large that still adopted in more recent studies, such as those from the S. Smith and H. Guo groups.<sup>6–9;63–72</sup> *ScalIT*, on the other hand, adopts an entirely different approach—a much more powerful, flexible, and scalable strategy, focused on parallelization at the matrix-vector product level, and thus allowing for true, distributed-memory, massive

parallelization. (See Paper I for additional discussion, both of the history of parallel QD calculations, as well as ***ScalIT*** itself.) Note that HO<sub>2</sub> rovibrational state calculations even as low as  $J=10$  are *extremely* challenging; S. Smith once estimated that roughly *one-half year* would be required on a single 1.9 GHz Pentium 4 CPU. Here, using ***ScalIT***, we are able to perform even one of the largest ( $J = 120$ ) calculations on a single Intel Xeon node (two 2.66 GHz hex-core CPUs) in less than six hours. HO<sub>2</sub> may thus be regarded as a “small” application for ***ScalIT***—although in order to test parallel scalability, we have also performed some calculations across an artificially large number of cores (up to 1200 or so). In any event, ***ScalIT*** is currently also being applied to much more challenging tetraatomic and pentaatomic molecular applications.

The HO<sub>2</sub> bound rovibrational energy levels as computed in this chapter have also been used to rigorously evaluate the efficacy of VSD and RSD JS across the now fully extended  $J$  range. Part and parcel with this analysis is the extent to which reasonable  $K$  labels can be legitimately assigned, which is also considered. Previous work by S. Smith and coworkers<sup>9</sup> found the performance of VSD JS to be rather modest, even for the single vibrational excitation bands. Moreover, higher vibrational excitation was found to rapidly lead to deterioration of this approach, due to floppiness associated with the low-lying DMBE IV barrier to linear geometry<sup>64</sup> (although later authors claim that the tee-shaped transition state<sup>76</sup> is lower energy; the equilibrium ground state of HO<sub>2</sub> is in any case bent). As expected, performance was also found to diminish with increasing  $J$ , up to the highest,  $J = 50$  value considered by those authors. By that point, however, even the HC approximation (i.e. the validity of the quantum label  $K$ ) was found to be breaking down. More importantly, these authors conclude that the JS and HC approximations are incapable of providing an indication of their own limitations, and thereby avoiding the need for expensive exact quantum calculations.

Our own work as presented here and elsewhere corroborates and enhances the findings of S. Smith (and less directly, H. Guo) and coworkers. Although a comprehensive comparison of different JS schemes as applied to the HO<sub>2</sub> bound rovibrational energy levels will form the subject of Chapter 5, we do provide here a comparison of VSD vs. RSD JS for  $J = 50$ . Based on the above discussion, this is perhaps beyond

the point where any JS scheme might be expected to operate effectively. Nevertheless, our RSD scheme is found to be at least one order of magnitude more accurate than VSD, with many predictions within a few meV of the correct values. We also present a detailed characterization of a  $J = 120$  rovibrational wavefunction, in terms of an underlying RSD JS description. Even in this extreme context, the latter picture is found to provide valuable dynamical insight—although not necessarily a very accurate prediction of the energy levels, per se. Indeed, as discussed in Section 4.5, this analysis also sheds some dynamical light on the scattering case as well.

The remainder of this chapter is organized as follows. Section 4.2 briefly describes the theoretical framework for the rovibrational calculations of triatomic molecules in Jacobi coordinates (Section 4.2). It also explains the basic operation of the VSD and RSD JS strategies used here (Section 4.3). Section 4.4 presents numerical details for the specific *ScalIT* HO<sub>2</sub> bound rovibrational state calculations of this chapter. Results and discussion are then presented in Section 4.5, including tables of rovibrational energy levels (Section 4.5.1), analysis of JS for  $J = 50$  (Section 4.5.2), and analysis of a  $J = 120$  wavefunction (Section 4.5.3). Finally, a summary and concluding remarks are provided in Section 4.6.

## 4.2 Rovibrational Calculations for Triatomic AB<sub>2</sub> Molecules

The framework for rovibrational calculations of ABC triatomics was laid out in Chapter 2. Here, we connect that framework to the AB<sub>2</sub> molecule, and discuss associated changes. The full dimensional rovibrational Hamiltonian described by Equation 2.1 stays the same, with  $r$  becoming the distance between the two O atoms, and  $R$  the distance between H and the O–O center of mass. There reduced masses of Equation 2.2,  $\mu_R$  and  $\mu_r$ , become

$$\begin{aligned}\mu_r &= \frac{m_{\text{O}}m_{\text{O}}}{m_{\text{O}} + m_{\text{O}}} = \frac{m_{\text{O}}}{2} \\ \mu_R &= \frac{m_{\text{O}_2}m_{\text{H}}}{m_{\text{O}_2} + m_{\text{H}}} = \frac{2m_{\text{O}}m_{\text{H}}}{2m_{\text{O}} + m_{\text{H}}},\end{aligned}\tag{4.2}$$

with  $m_{\text{O}}$  and  $m_{\text{H}}$ , respectively, the masses of the O and H atoms.

The ground state geometry for the HO<sub>2</sub> system is bent, and corresponds to a prolate (but slightly asymmetric) rigid rotor. Due to the large  $m_{\text{O}}/m_{\text{H}}$  mass ratio,

the smallest moment of inertia aligns roughly with  $\vec{r}$ , which is thus taken as the body-fixed  $z$  axis. This leads to the rotational quantum numbers  $J$  and  $K$  in the usual fashion—although the latter (as discussed previously) is not perfectly “good,” due to Coriolis coupling. The rigorously good quantum numbers are:  $J$ , the total angular momentum;  $M$ , the projection onto the space-fixed  $Z$  axis;  $\epsilon = \pm 1$ , the total inversion parity.

The rovibrational eigenstate wavefunctions can thus be labeled  $\Psi^{JM\epsilon}$ , and expanded as previously explained in Chapter 2.

For  $AB_2$  molecules such as  $HO_2$ , permutation of the two identical atoms is another symmetry operation to be considered. The effect on the parity-adapted combined bend-rotation angular functions is

$$Y_{jK}^{JM\epsilon}(\alpha, \beta, \gamma, \theta) \rightarrow \epsilon(-1)^{J-j} Y_{jK}^{JM\epsilon}(\alpha, \beta, \gamma, \theta). \quad (4.3)$$

One half of these functions are thus symmetric (even) under O atom exchange; the other half are antisymmetric (odd). Since  $^{16}O$  is a spin-zero boson, and the  $HO_2$  ground electronic state exhibits ( $^2A''$ ) symmetry, only those rovibrational states with odd permutation symmetry exist.

Using the basis set above, the  $(J, M, \epsilon)$  block of the rovibrational Hamiltonian of Equation 2.1 becomes:

$$\begin{aligned} \mathbf{H}^{JM\epsilon} = & H_{v_1 v_1'}^R \delta_{v_2 v_2'} \delta_{jj'} \delta_{KK'} + H_{v_2 v_2'}^r \delta_{v_1 v_1'} \delta_{jj'} \delta_{KK'} \\ & + \left[ \frac{J(J+1) - 2K^2}{2\mu_R R_{v_1}^2} + \left( \frac{1}{2\mu_R R_{v_1}^2} + \frac{1}{2\mu_r r_{v_2}^2} \right) j(j+1) \right] \delta_{v_1 v_1'} \delta_{v_2 v_2'} \delta_{jj'} \delta_{KK'} \\ & - \left[ \frac{\lambda_{JK}^+ \lambda_{jK}^+}{2\mu_R R_{v_1}^2} \sqrt{1 + \delta_{K0}} \delta_{K+1, K'} + \frac{\lambda_{JK}^- \lambda_{jK}^-}{2\mu_R R_{v_1}^2} \sqrt{1 + \delta_{K1}} \delta_{K-1, K'} \right] \delta_{v_1 v_1'} \delta_{v_2 v_2'} \delta_{jj'} \\ & + [V_{jj'}^K(R_{v_1}, r_{v_2}) - V_R(R_{v_1}) \delta_{jj'} - V_r(r_{v_2}) \delta_{jj'}] \delta_{v_1 v_1'} \delta_{v_2 v_2'} \delta_{KK'} \end{aligned} \quad (4.4)$$

where

$$\begin{aligned} \lambda_{JK}^\pm &= \sqrt{J(J+1) - K(K \pm 1)}, \lambda_{jK}^\pm = \sqrt{j(j+1) - K(K \pm 1)}, \\ V_{jj'}^K(R_{v_1}, r_{v_2}) &= \left( \frac{1 + \epsilon \delta_{K0}}{1 + \delta_{K0}} \right) \langle \Theta_{jK}(\theta) | V(R_{v_1}, r_{v_2}, \theta) | \Theta_{j'K}(\theta) \rangle, \end{aligned} \quad (4.5)$$

and  $V_R(R)$  and  $V_r(r)$  are the PSO “effective potentials” in  $R$  and  $r$ , respectively (used to generate the corresponding PSODVRs<sup>86–89</sup>).

### 4.3 $J$ -shifting Strategies

In Paper I, the low-lying ( $J \leq 10$ ) rovibrational eigenenergies as computed using *ScalIT* were assigned  $K$  values, and used to compute (VSD) rotational constants for HO<sub>2</sub>.<sup>25</sup> The results are in surprisingly good agreement with a previous calculation<sup>15</sup> that used only  $J = 0$  and  $J = 1$  rovibrational data. In this section, we use various JS schemes to do the reverse; a rotational energy shift associated with the rigid rotor kinetic energy is added to an exact  $J = 0$  vibrational state energy, in order to estimate the energy of a corresponding rovibrational state.<sup>9;48;53;54;66;71;72;78–83</sup> The accuracy of the JS predictions are then established via direct comparison with the corresponding exact rovibrational levels obtained using *ScalIT*, once the latter have been assigned  $K$  labels. The  $K$  assignment is clear for the low-lying  $J$  values, but starts to become a bit ambiguous for the larger  $J$  values.

Throughout this chapter, the symmetric rigid rotor form of the rotational kinetic energy shift is presumed. This can be rationalized via the slightly-asymmetric-prolate-top arguments of Section 4.2, but also by the fact that the earlier work as described in the previous paragraph<sup>15;25</sup> found the two small rotational constants to be nearly identical. In any event, the symmetric rigid rotor form leads to

$$\begin{aligned} E_{vJK}^{J\text{-shift}} &= E_v + E_{JK}^{\text{rot}}, & \text{where} \\ E_{JK}^{\text{rot}} &= (A - B)K^2 + BJ(J + 1) \end{aligned} \quad (4.6)$$

as the JS prediction for the true rovibrational energy  $E_{vJK}$ , in terms of the vibrational energy  $E_v$ , the rotational state  $(J, K)$ , and the rotational constants,  $A$  and  $B$ . For the presumed prolate HO<sub>2</sub> rigid rotor,  $A > B$ .

Different JS schemes may be distinguished with regard to how the values of  $A$  and  $B$  are determined (or more generally  $E_{JK}^{\text{rot}}$ ; The next chapter will explore quite a number of options). The simplest choice is to use the moments of inertia associated with the HO<sub>2</sub> equilibrium ground state geometry, to obtain one set of rotational constants for use with all rovibrational states. Though necessarily asymmetric, the

two small rotational constants (being nearly identical as discussed above) can be simply averaged together to obtain the symmetric rotor form of Equation 4.6.<sup>9;48;79–81</sup>

Of course, the rotational constants can also be determined experimentally. In this context, a more refined and commonly employed spectroscopic technique is to allow the rotational constants to depend on the vibrational state,  $v$ , giving rise to a VSD JS scheme. Using  $A(v)$  and  $B(v)$  values for the ground and lowest two singly-excited vibrational states of HO<sub>2</sub> as obtained from earlier experimental work of J. B. Burkholder and coworkers,<sup>90</sup> the S. Smith group applied VSD JS to the lowest-lying dozen or so rovibrational states (of each parity) for  $J = 50$ .<sup>9</sup>

In this section, we explore an RSD JS scheme, for which the rotational constants depend on the *rotational*, rather than vibrational, state. Again, a similar strategy may be found in standard spectroscopic analysis, where centrifugal distortion and related effects are incorporated via higher-order  $J$  and  $K$  terms in the rotational kinetic energy expansion. Rather than obtaining the expansion parameters via fitting to experimental data, however, we rely on a more natural and purely theoretical determination of the  $E_{JK}^{\text{rot}}$  values. This leads to a cleaner and more self-consistent assessment of the efficacy of the JS approach (since the PES may itself exhibit discrepancies vs. experimental data), and—for the HO<sub>2</sub> example at least—far better performance than for VSD JS.

The RSD JS scheme is based on an alternate—and in many respects more natural—form of the exact rovibrational quantum Hamiltonian that was first derived by B. Poirier in 1998.<sup>82;83;91</sup> One feature of this approach is that it automatically generalizes the two-body notion of the “centrifugal potential” for three-body systems. Among other benefits, this allows for a true direct-product basis representation of the rovibrational Hamiltonian, using a single  $K$ -independent bend-angle basis set—as was once advocated by J. M. Bowman himself,<sup>48</sup> and successfully applied to real molecular systems by B. Poirier<sup>91</sup> [though the traditional  $K$ -dependent basis of Equation 2.3 is used in the present work].

As might be expected via analogy with the two-body case, the three-body centrifugal potential depends on the triatomic internal coordinates,  $(R, r, \theta)$ , as well as the rotational state indices,  $(J, K)$ . Also, it is added directly to the true potential, to obtain the “effective potential” governing the dynamics for a given rotational state.

The explicit formula for the latter is found to be<sup>82;83</sup>

$$V_{JK}^{\text{eff}}(R, r, \theta) = V(R, r, \theta) + \frac{J(J+1)}{2\mu_r r^2} + \left( \frac{1}{2\mu_R R^2 \sin^2 \theta} + \frac{\cot^2 \theta - 1}{2\mu_r r^2} \right) K^2, \quad (4.7)$$

in units where  $\hbar = 1$ , as are presumed throughout this chapter.

Curiously, the centrifugal potential energy in Equation 4.7 has the form of a symmetric rigid rotor for all geometries—even though the actual three-body rotor is generally asymmetric. In any event, to extract a meaningful RSD JS approximation from Equation 4.7, one simply minimizes  $V_{JK}^{\text{eff}}(R, r, \theta)$  rather than  $V(R, r, \theta)$  itself, with respect to the internal coordinates, for each rotational state  $(J, K)$ . The resultant RSD energy shift—i.e.,  $E_{JK}^{\text{rot}}$  in Equation 4.6—is then taken to be

$$\min[V_{JK}^{\text{eff}}(R, r, \theta)] - \min[V(R, r, \theta)], \quad (4.8)$$

where the two minima are evaluated independently. Note that this differs slightly from the scheme proposed in Ref. [82], for which *both*  $V$  and  $V_{JK}^{\text{eff}}$  are evaluated at the minimum geometry of the latter.

#### 4.4 Computational Details

A number of PESs may be found in the HO<sub>2</sub> literature<sup>43;44;50;65–68</sup> (for an overview, consult Paper I.<sup>25</sup>). As per Section 4.1, however, we use the DMBE IV PES in the present work. This PES was used in all previous HO<sub>2</sub> rovibrational state calculations,<sup>6–9;15;25</sup> with which we wish to compare our results. Since the system and PES are the same as in Paper I, the radial PSO effective potentials,  $V_R(R)$  and  $V_r(r)$ , are also the same as were used in Paper I (Section 4.2). The radial sinc-DVR grid<sup>92</sup> used is also the same, i.e. 6000 uniformly spaced points in both  $R$  and  $r$ , across the coordinate ranges indicated in Table 4.1.

In Paper I, the number of radial PSODVR points used was  $N_R=60$  for coordinate  $R$ , and  $N_r=40$  for coordinate  $r$ . Comprehensive convergence testing indicated that these values correspond to final computed HO<sub>2</sub> rovibrational energies that are all converged to better than  $10^{-6}$  eV—including the highly-vibrationally-excited states close to the dissociation threshold, as well as rotationally excited states corresponding to the highest  $J$  value considered ( $J = 10$ ). As a comparison, S. Smith and coworkers

**Table 4.1:** Parameters used for all HO<sub>2</sub> bound rovibrational eigenstate calculations presented in this chapter. All units are atomic units.

Category	Parameter	Value (a.u.)
Mass	$\mu_r$	14578.471659
	$\mu_R$	1781.041591
Coordinate ranges	$r_{\min}$	1.0
	$r_{\max}$	11.0
	$R_{\min}$	0.0
	$R_{\max}$	11.0

used a standard PO DVR of size  $(N_R=110) \times (N_r=50)$ , contracted from a  $315 \times 150$  primitive sinc-DVR grid,<sup>24</sup> for both their low- $J$ <sup>7;8</sup> and high- $J$ <sup>9</sup> HO<sub>2</sub> rovibrational state calculations. Despite using more than twice as many radial DVR functions as we did, their calculations achieve significantly less accuracy than the present work (their stated accuracy was  $10^{-5}$  eV or so, although comparison with our results suggests  $10^{-4}$  eV or better, for the larger  $J$  values). This is a testament to the efficacy of the PSODVR approach, and in line with what we have observed previously using this method.

In the present chapter, we compute the lowest-lying 30 bound rovibrational eigenstates, for each  $J$  and  $\epsilon$  value considered. For  $J < 90$ , these states lie sufficiently far from the dissociation threshold that substantially fewer radial PSODVR points are required than was the case in Paper I. This is indicated in Columns II and III of Table 4.2, which lists the number of radial PSODVR points in  $r$  and  $R$ , respectively, required to converge all of the computed energy eigenvalues at the specified  $J$  value to  $10^{-6}$  eV or better. On the other hand, the  $90 \leq J \leq 110$  PSODVR grid sizes match those of Paper I, and the  $J = 120$  and  $J = 130$  PSODVR grid sizes slightly *exceed* the older values. This situation will be further commented upon below.

In the highest- $J$  calculations that were performed by S. Smith and coworkers,<sup>9</sup> the lowest-lying 12–15 rovibrational states of each parity for  $J = 30, 40,$  and  $50$  were computed, and assigned  $K$  and  $v$  labels. Separate low- $J$  studies provided similar data for  $J = 10$  (but without the  $v$  labels),<sup>7</sup> and for  $J = 20$  (with neither  $v$  nor  $K$  labels). Note that these results encompass only the lowest two vibrational excitations. It should be mentioned that Ref. [9] also includes some high-lying eigenstates for each

**Table 4.2:** Basis sizes used for various HO<sub>2</sub> bound rovibrational eigenstate calculations presented in this chapter, as a function of total angular momentum,  $J$ :  $N_r$ , the number of radial PSODVR points in  $r$ ;  $N_R$ , the number of radial PSODVR points in  $R$ ;  $j_{\max}$ , the number of bend-angle ( $\theta$ ) basis functions;  $jK_{\text{num}}$ , the number of combined bend-rotation basis functions. These were used to achieve convergence of all computed eigenvalues to  $10^{-6}$  eV or better.

$J$ value	$N_r$	$N_R$	$j_{\max}$ value	$jK_{\text{num}}$ value
10	22	24	90	600
20	22	24	90	600
30	22	24	90	650
40	22	26	90	650
50	22	26	90	650
60	24	26	90	650
70	30	50	120	800
80	30	50	120	800
90	40	60	130	1000
100	40	60	130	1000
110	40	60	130	1000
120	50	60	200	1000
130	50	60	225	1000
50 (highest-lying)	30	40	120	900

of the three  $J$  values—although these defy all attempts at labeling. In any event, their low-lying results may be directly compared with those of the present chapter—as the same DMBE IV PES was used, and no  $K$  truncation was applied. The  $v$  label assignments enable use of VSD JS, as was applied and assessed in Ref. [9]. A similar calculation is performed in this chapter for the  $J = 50$ ,  $\epsilon = 0$  (even parity) rovibrational states—but using RSD JS, and our own  $K$  assignments.

The final convergence parameter impacting the accuracy of the HO<sub>2</sub> energy level calculation is  $j_{\max}$ —the maximum value for  $j$  in Equation 4.4, and (essentially) the number of bend-angle basis functions. To achieve a final level of convergence comparable to that of the radial PSODVR, the  $j_{\max}$  values indicated in Table 4.2 were employed. As  $j_{\max}$  must be larger than  $J$  itself—provided no  $K$  truncation is applied, as is the case here—one expects a marked  $J$  dependence, as is indeed observed in the Table. Together with the expanded  $K$  range, this is the reason that larger  $J$  values lead to much more expensive calculations. A more direct measure of this increase,

however, is to be found in  $jK_{\text{num}}$ —the total number of combined bend-rotation basis functions used in the calculation—whose values are provided in Column V of Table 4.2. In comparison with the high- $J$  calculations of S. Smith and coworkers, our angular basis sizes are significantly larger—reflecting the fact that the underlying basis functions are (essentially) the same in both calculations, but our calculation is performed to substantially higher accuracy. Note that their calculation introduces quadrature error in the potential energy matrix elements through the use of an associated Legendre DVR grid, which may also affect the accuracy of their results.

All in all, the total basis size used by S. Smith and coworkers for their largest,  $J = 50$  calculation was around  $5.7 \times 10^6$ , whereas our corresponding largest  $J = 50$  basis is  $1.08 \times 10^6$ . They used the same basis for both their low- and high-lying energy window calculations. In our case, we singled out the high-lying HO<sub>2</sub> bound rovibrational states of  $J = 50$  for special consideration, as potentially the most computationally challenging of all. In general, increasing  $J$  increases the required number of combined bend-rotation states (Table 4.2), making the calculation more difficult; but at the same time, it also leads to a shallower effective potential well [Equation 4.7], making the calculation easier. The “worst of both worlds” is therefore likely to be found in the middle of the  $J$  range—e.g., around  $J = 50$ . In any event, we have performed  $J = 50$  calculations for a number of spectral windows at successively higher energies—with the largest basis size as reported above that used for the highest-lying window. As it happens, the  $J = 120$  calculation required an even larger basis size, owing to the presence of states just below the dissociation threshold—although the highest-lying  $J = 50$  calculation was still the more computationally expensive, owing to the increased number of QMR iterations (Section 4.5.1).

We note that we have conducted many hundreds of convergence tests, considering each value of  $J$  separately, to ensure the validity of all of our computed results. S. Smith and coworkers performed accurate convergence testing for  $J = 0$ , and then used the same converged radial basis sizes for all of their larger  $J$  calculations. Equation (4.7) suggests that this should in fact be a legitimate strategy—since the effective potential is (virtually always) positive, and the same number of states is being computed for each  $J$ . Of course, such an analysis is only valid so long as the computed eigenstates are far from the dissociation threshold—when the latter is approached,

one expects larger PSODVR grids to be required, perhaps on the order of the largest  $J = 0$  grids from Paper I. Our own work leads to a slightly different conclusion, however. From Table 4.2, we find that: (1) radial PSODVR grid sizes must be increased throughout the  $J$  range, not just at the highest values where dissociation is approached; (2) the highest  $J$  values require slightly larger radial PSODVR grids than in Paper I. The underlying reasons are not entirely clear, but may have to do with the fact that increasing  $J$  results in an effective potential well that is *broader*, as well as shallower.

Parallel scalability of the HO<sub>2</sub> *ScalIT* calculations was also investigated. By the standards of many iterative sparse matrix calculations, the total basis size required for even one of the largest ( $J = 120$ ) calculations performed here—i.e.,  $2.5 \times 10^6$ —is quite modest. Consequently, the bottleneck, stage 3 component of even this  $J = 120$  calculation can be performed on a single Intel Xeon node (two 2.66 GHz hex-core CPUs) in less than six hours. For convenience however, most of the larger of the calculations were parallelized across five nodes, or 60 cores. The corresponding parallel speedup observed for the above  $J = 120$  calculation was about  $45\times$ , corresponding to an excellent parallel efficiency of 75.4%—despite the small problem size, and the significant amount of distributed memory parallelization. As an explicit test of scalability, we further parallelized this same calculation (up to ten nodes, or 120 cores), leading to a maximum parallel speedup of around  $66\times$ . In contrast, the best speedup achieved by S. Smith and coworkers was around  $6\times$ —even though they used only shared, not distributed, memory parallelization.

The calculations described above were performed on the Robinson cluster (Texas Tech University Department of Chemistry and Biochemistry). Although HO<sub>2</sub> presents a “small” application vis-à-vis massive parallelization, some scalability tests across a much larger number of nodes were also performed—using the Lonestar cluster (Texas Advanced Computation Center), which has a similar architecture as Robinson (twelve cores per node and low-latency, high-bandwidth Infiniband connectivity). Even though the HO<sub>2</sub> application size was not increased, effective parallel scalability was achieved across 100 or so Lonestar *nodes*. However, this study also revealed some inefficiency in the combining of shared and distributed parallelization in the second phase of stage 3 (Appendix A) that bears further investigation.

## 4.5 Results and Discussion

### 4.5.1 Rovibrational Eigenstates

Using *ScalIT*, bound rovibrational energy levels of HO<sub>2</sub> were computed for all multiple-of-ten  $J$  values, up to the largest  $J$  for which bound states exist ( $J = 120$ ) and a bit beyond ( $J = 130$ ). Only states with odd permutation symmetry were considered, as nuclear spin-statistics rule out the physical existence of the even permutation symmetry states. However, both even and odd parity states were computed for each  $J$  value considered. For each  $J$  and parity value, the lowest-lying 30 rovibrational energies were obtained from a single PIST spectral window calculation.<sup>93–95</sup> For  $J = 50$  with even parity, a number of higher-lying spectral window calculations were also performed, in order to compute the lowest-lying 125 states. All rovibrational energies are reported in eV, relative to the vibrational ground state energy from Paper I.

Each calculation typically required around 100 Lanczos iterations, and 15 QMR iterations per Lanczos iteration—or 1500 iterations total—to converge the 30 states. This is with a typical Wyatt window size of around 50 states (a larger window would have led to fewer QMR iterations, but greater computational cost for the preconditioner construction). In contrast, S. Smith and coworkers required from  $10^5$  to  $10^6$  iterations to converge each of their filter diagonalization calculations<sup>9;64</sup>—although their computational cost per iteration is somewhat less than ours. For so many iterations—arguably the largest ever published at the time—reorthogonalization of the Lanczos vectors is certainly not possible,<sup>22</sup> and so those authors must contend with spurious eigenvalues and other headaches.

Regardless of the iterative method used, the number of iterations increases with increasing spectral energy. For our even-parity  $J = 50$  calculations, for instance, around 400 QMR iterations per Lanczos iteration were required for the highest-lying spectral window considered, using a Wyatt window of 750 states. Consequently, these were the most time-consuming of our calculations (13.9 hours across 36 cores), even though the basis size was smaller than for  $J = 120$  and  $J = 130$ , as indicated in Table 4.2.

For  $J = 120$ , the attractive PES well is nearly obliterated by the centrifugal potential, and so the effective potential of Equation 4.7 is very shallow. Only around

20 bound rovibrational eigenstates of each parity were obtained for this  $J$  value. For  $J = 130$ , a large-basis calculation found no rovibrational eigenstates for either parity; the converged even-parity ground state, for example, was found to lie at  $7.69 \times 10^{-2}$  eV above the H+O<sub>2</sub> dissociation threshold of 2.0158147 eV (relative to the vibrational ground state<sup>25</sup>). This would appear to rule out any  $J = 130$  bound states—although it is conceivable that a new calculation with an expanded radial coordinate range might reveal the above state to be extremely weakly bound. In any event, the  $J = 130$  calculation was performed here to confirm that we have indeed reached the end of the  $J$  range for the bound states. In the  $J = 120$  case, in addition to computing rovibrational energy eigenvalues, *ScalIT* was also used to compute a representative wavefunction (see Section 4.5.3 for further discussion).

The HO<sub>2</sub> bound rovibrational energy levels for  $J = 10$ , for both even and odd parities, are presented in Table 4.3. These states have been previously investigated, by S. Smith and coworkers,<sup>7</sup> and by the present author (Paper I). The previous results are also presented here, and serve as a useful check on the present results. All of the new eigenvalues agree with those of Paper I to within the accuracy that those two sets of calculations were converged—i.e.,  $10^{-6}$  eV or better. The agreement with S. Smith and coworkers is to within  $10^{-4}$  eV or better. The  $K$  values listed in the Table are our assignments, as obtained using the procedure described in Section 4.5.2. These agree with the assignments used in Paper I, apart from a switching of the  $n = 25$  and  $n = 26$  even-parity labels, where  $n$  labels the rovibrational state excitation.

The HO<sub>2</sub> bound rovibrational energy levels for  $J = 20$ , for both even and odd parities, are presented in Table 4.4. These states have also been previously investigated by S. Smith and coworkers,<sup>8</sup> using similar methodology and basis sets as for their  $J = 10$  study. Perhaps not surprisingly, therefore, the agreement of their results with ours is again to within  $10^{-4}$  eV or better.

The HO<sub>2</sub> bound rovibrational energy levels for  $J = 30$  and 40, for both even and odd parities, are presented, respectively, in Tables 4.5 and 4.6. Together with  $J = 50$ , these states have also been previously investigated by S. Smith and coworkers, in their high- $J$  study of 2006.<sup>9</sup> Note that they have only computed the lowest 12–15 states of each  $J$  and parity, whereas we continue to obtain states up to  $n = 30$ . For those states for which S. Smith and coworkers have provided data, the computed energy

**Table 4.3:** Lowest-lying rovibrational energy levels of HO<sub>2</sub> for total angular momentum  $J = 10$ , with odd permutation symmetry and both even and odd parity. All energies are in eV, and relative to the vibrational ground state. Previous results from Paper I<sup>25</sup> and from S. Smith *et al.*<sup>7</sup> are also presented. New energies are converged to  $10^{-6}$  eV or better; they agree with Paper I to this level of accuracy, and with Ref. [5] to within  $10^{-4}$  eV or better. Columns II and VI: our  $K$  assignments. These agree with Paper I, except for the even parity  $n = 25$  and 26 assignments, which are switched.

Index $n$	Even Parity				Odd Parity			
	$K$	Smith/LHFD	Poirier/2010	This Work	$K$	Smith/LHFD	Poirier/2010	This Work
1	0	0.014855	0.014863	0.0148635	1	0.017474	0.017480	0.0174802
2	1	0.017049	0.017058	0.0170575	2	0.024455	0.024461	0.0244614
3	2	0.024463	0.024473	0.0244729	3	0.036425	0.036433	0.0364339
4	3	0.036426	0.036436	0.0364361	4	0.053143	0.053153	0.0531532
5	4	0.053143	0.053156	0.0531555	5	0.074573	0.074586	0.0745858
6	5	0.074573	0.074588	0.0745881	6	0.100669	0.100685	0.1006848
7	6	0.100669	0.100687	0.1006871	7	0.131375	0.131394	0.1313944
8	7	0.131375	0.131396	0.1313967	1	0.149204	0.149224	0.1492244
9	0	0.146616	0.146635	0.1466357	2	0.156098	0.156119	0.1561186
10	1	0.148782	0.148801	0.1488015	3	0.166628	0.166651	0.1666509
11	2	0.156107	0.156127	0.1561274	8	0.167922	0.167944	0.1679447
12	8	0.166628	0.166653	0.1666532	1	0.178402	0.178415	0.1784157
13	3	0.167922	0.167944	0.1679443	4	0.184436	0.184461	0.1844606
14	0	0.175663	0.175679	0.1756787	2	0.185646	0.185660	0.1856603
15	1	0.177932	0.177947	0.1779468	3	0.198090	0.198106	0.1981061
16	4	0.184436	0.184460	0.1844602	5	0.205607	0.205633	0.2056337
17	2	0.185656	0.185673	0.1856730	9	0.206335	0.206383	0.2063827
18	3	0.198090	0.198108	0.1981079	4	0.215462	0.215479	0.2154794
19	5	0.205607	0.205633	0.2056333	6	0.231388	0.231417	0.2314174
20	9	0.206355	0.206385	0.2063850	5	0.237720	0.237741	0.2377409
21	4	0.215461	0.215481	0.2154813	10	0.250479	0.250512	0.2505115
22	6	0.231388	0.231417	0.2314170	7	0.261717	0.261750	0.2617504
23	5	0.237720	0.237743	0.2377428	6	0.264817	0.264842	0.2648418
24	10	0.250479	0.250514	0.2505137	1	0.276003	0.276039	0.2760385
25	6	0.261717	0.261750	0.2617501	2	0.282813	0.282850	0.2828497
26	7	0.264818	0.264844	0.2648437	3	0.294493	0.294534	0.2945335
27	0	0.273446	0.273480	0.2734798	7	0.296302	0.296334	0.2963343
28	1	0.275586	0.275620	0.2756196	8	0.296923	0.296953	0.2969525
29	2	0.282822	0.282857	0.2828565	1	0.309843	0.309870	0.3098703
30	3	0.294496	0.294530	0.2945330	4	0.310810	0.310852	0.3108521

**Table 4.4:** Lowest-lying rovibrational energy levels of HO<sub>2</sub> for total angular momentum  $J = 20$ , with odd permutation symmetry and both even and odd parity. All energies are in eV, and relative to the vibrational ground state. Previous results from S. Smith *et al.*<sup>8</sup> are also presented. New energies are converged to  $10^{-6}$  eV or better; they agree with Ref. [6] to within  $10^{-4}$  eV or better. Columns II and V: our  $K$  assignments.

Index $n$	Even Parity			Odd Parity		
	$K$	Smith/LSFD	This Work	$K$	Smith/LSFD	This Work
1	0	0.056551	0.0565703	1	0.059852	0.0598696
2	1	0.058240	0.0582594	2	0.066237	0.0662548
3	2	0.066369	0.0663898	3	0.078223	0.0782420
4	3	0.078220	0.0782416	4	0.094902	0.0949208
5	4	0.094900	0.0949232	5	0.116287	0.1163096
6	5	0.116287	0.1163119	6	0.142334	0.1423575
7	6	0.142333	0.1423598	7	0.172981	0.1730081
8	7	0.172981	0.1730104	1	0.190651	0.1906837
9	0	0.187386	0.1874178	2	0.196693	0.1969833
10	1	0.189058	0.1890818	3	0.208167	0.2081975
11	2	0.197082	0.1971150	8	0.208784	0.2088182
12	8	0.208167	0.2081998	1	0.221083	0.2211057
13	3	0.208930	0.2088153	4	0.225250	0.2252848
14	0	0.217634	0.2176066	2	0.227667	0.2276917
15	1	0.219282	0.2193221	3	0.240132	0.2401573
16	4	0.225250	0.2252846	5	0.246363	0.2464000
17	2	0.227822	0.2278492	9	0.247821	0.2478543
18	3	0.240130	0.2401558	4	0.257468	0.2574890
19	5	0.246363	0.2463998	6	0.272070	0.2721084
20	9	0.247821	0.2478566	5	0.279748	0.2797138
21	4	0.257462	0.2574909	10	0.291863	0.2919002
22	6	0.272069	0.2721083	7	0.302291	0.3023322
23	5	0.279680	0.2797157	6	0.306807	0.3067943
24	10	0.291863	0.2919024	1	0.316543	0.3165921
25	6	0.302293	0.3023321	2	0.322767	0.3228162
26	7	0.306762	0.3067961	3	0.334457	0.3345072
27	0	0.313319	0.3133660	7	0.336807	0.3368487
28	1	0.314994	0.3150107	8	0.338825	0.3388240
29	2	0.322896	0.3229438	1	0.340210	0.3402506
30	3	0.334454	0.3345025	4	0.350723	0.3507751

levels agree to within  $10^{-4}$  eV or better with our results, and the  $K$  assignments agree perfectly with ours.

As discussed previously, the  $J = 50$  case is singled out for special consideration. The  $\text{HO}_2$  bound rovibrational energy levels for  $J = 50$  and even parity are presented in Table 4.7. Like the other calculations, these are converged to  $10^{-6}$  eV or better. In this Table, we provide both  $K$  and  $v$  labels—where  $v$  refers to the vibrational excitation—according to the procedure described in Section 4.5.2. The latter label is required for VSD JS, as performed in Ref. [9] and in this chapter (along with RSD JS) in Section 4.5.2. In any event, our  $K$  and  $v$  labels agree perfectly with those of Ref. [9], for the 15 states for which they have provided data. The computed rovibrational energies for these states also again agree to within  $10^{-4}$  eV or better. Similar comments also apply for the odd-parity  $J = 50$  levels, as presented in Table 4.8. In Table 4.9, reaching about halfway up the bound spectrum, the lowest-lying 125 bound rovibrational energy levels for  $J = 50$  and even parity are presented, obtained using multiple spectral energy windows. As discussed in Section 4.4 and above, these constitute some of the most difficult possible spectral calculations for  $\text{HO}_2$ .

Continuing along these lines, the  $\text{HO}_2$  bound rovibrational energy levels for  $J = 60, 70,$  and  $80$ , for both even and odd parities, are presented, in Table 4.10. No previous calculations exist for comparison. Also, for such large  $J$  values, we do not bother to make  $K$  value assignments. Similar results for  $J = 90, 100, 110,$  and  $120$  are presented in Table 4.11. These rovibrational energies become increasingly close to the dissociation threshold of 2.0158147 eV, with the  $J = 120$  states reaching dissociation by  $n \approx 20$  for both parities. As discussed, the proximity to dissociation leads to a substantially more difficult calculation. Nevertheless, we were able to converge all computed energies to our target accuracy of  $10^{-6}$  eV or better. That said, it may be that the highest-lying rovibrational energies for  $J = 120$ , i.e. those lying just below the dissociation threshold, might change a bit under a new calculation performed using an expanded radial coordinate range.

#### 4.5.2 $J$ -shifting Results for $J = 50$

As discussed in Section 4.1, the validity of the HC and JS approximations as applied to  $\text{HO}_2$  is a topic of perennial interest.<sup>9;45;48;53;54;58;66;68-72</sup> The general feel-

**Table 4.5:** Lowest-lying rovibrational energy levels of HO<sub>2</sub> for total angular momentum  $J = 30$ , with odd permutation symmetry and both even and odd parity. All energies are in eV, and relative to the vibrational ground state. Previous results from S. Smith *et al.*<sup>9</sup> are also presented. New energies are converged to  $10^{-6}$  eV or better; they agree with Ref. [9] to within  $10^{-4}$  eV or better. Columns II and V: our  $K$  assignments (agree with Ref. [9]).

Index $n$	Even Parity			Odd Parity		
	$K$	Smith/LSFD	This Work	$K$	Smith/LSFD	This Work
1	0	0.124642	0.1246776	1	0.129246	0.1292814
2	1	0.125728	0.1257642	2	0.134702	0.1347378
3	2	0.135318	0.1353560	3	0.146814	0.1468507
4	3	0.146785	0.1468240	4	0.163395	0.1634332
5	4	0.163396	0.1634361	5	0.184703	0.1847425
6	5	0.184702	0.1847448	6	0.210660	0.2107025
7	6	0.210661	0.2107047	7	0.241209	0.2412539
8	7	0.241209	0.2412561	1	0.258503	0.2585524
9	0	0.253944	0.2539930	2	0.263879	0.2639284
10	1	0.255012	0.2550603	3	0.275937	0.2758806
11	2	0.26449	0.2645401	8	0.276284	0.2763316
12	8	0.275801	0.2758517	1	0.290950	0.2909922
13	3	0.276284	0.2763338	4		0.2922441
14	0	0.285991	0.2860331	2		0.2965573
15	1	0.287061	0.2871032	3		0.3091714
16	4		0.2922421	5		0.3132623
17	2		0.2972783	9		0.3158640
18	3		0.3091373	4		0.3263911
19	5		0.3132624	6		0.3388622
20	9		0.3158662	5		0.3485280
21	4		0.3263936	10		0.3597727
22	6		0.3388623	7		0.3689623
23	5		0.3485297	6		0.3755121
24	10		0.3597749	1		0.3829698
25	6		0.3689624	2		0.3882828
26	7		0.3755139	3		0.4000865
27	0		0.3784699	7		0.4034215
28	1		0.3795255	8		0.4073516
29	2		0.3888819	1		0.4079737
30	3		0.4000564	4		0.4162462

**Table 4.6:** Lowest-lying rovibrational energy levels of HO<sub>2</sub> for total angular momentum  $J = 40$ , with odd permutation symmetry and both even and odd parity. All energies are in eV, and relative to the vibrational ground state. Previous results from S. Smith *et al.*<sup>9</sup> are also presented. New energies are converged to a  $10^{-6}$  eV or better; they agree with Ref. [9] to within  $10^{-4}$  eV or better. Columns II and V: our  $K$  assignments (agree with Ref. [9]).

Index $n$	Even Parity			Odd Parity		
	$K$	Smith/LSFD	This Work	$K$	Smith/LSFD	This Work
1	0	0.218531	0.2185910	1	0.225158	0.2252188
2	1	0.219106	0.2191853	2	0.229505	0.2295107
3	2	0.231164	0.2312276	3	0.241961	0.2420222
4	3	0.241808	0.2418725	4	0.258325	0.2583874
5	4	0.25833	0.2583948	5	0.279508	0.2795725
6	5	0.279508	0.2795746	6	0.305336	0.3054022
7	6	0.305336	0.3054043	7	0.335742	0.3358109
8	7	0.335742	0.3358130	1	0.352246	0.3523197
9	0	0.345684	0.3457563	2	0.356469	0.3565420
10	1	0.346284	0.3463382	3	0.368807	0.3688821
11	2	0.358167	0.3582421	8	0.370658	0.3707302
12	8	0.368656	0.3687311	1	0.384935	0.3850113
13	3	0.370658	0.3707323	4		0.3875629
14	0	0.380266	0.3803327	2		0.3918437
15	1	0.380826	0.3808922	3		0.4049241
16	4		0.3850259	5		0.4059063
17	2		0.3938301	9		0.4100872
18	3		0.4047384	4		0.4218789
19	5		0.4059066	6		0.4313630
20	9		0.4100893	5		0.4438614
21	4		0.4218875	10		0.4538032
22	6		0.4313633	7		0.4613151
23	5		0.4438631	6		0.4706743
24	10		0.4538053	1		0.4746615
25	6		0.4613156	2		0.4788368
26	7		0.4681882	3		0.4910178
27	0		0.4687643	7		0.4956605
28	1		0.4706761	8		0.5017937
29	2		0.4805050	1		0.5022761
30	3		0.4908685	4		0.5069517

**Table 4.7:** Lowest-lying rovibrational energy levels of HO<sub>2</sub> for total angular momentum  $J = 50$ , with odd permutation symmetry and even parity. All energies are in eV, and relative to the vibrational ground state. Previous results from S. Smith *et al.*<sup>9</sup> are also presented—as are approximate VSD (Column V) and RSD (Column VIII) JS results, together with corresponding errors (Columns VI and IX, respectively). Column III: our  $K$  assignments (agree with Ref. [9]). Column II: vibrational state assignments (agree with Ref. [9]). Boldfaced entries indicate vibrationally excited rovibrational states.

State labels			Smith/LSFD			This Work		
$n$	$v$	$K$	Energy	VSD $J$ -Shift	Error	Energy	RSD $J$ -Shift	Error
1	0	0	0.337633	0.343722	-0.006089	0.3377239	0.3377239	0
2	0	1	0.337923	0.346111	-0.008188	0.3380129	0.3401239	-0.002110
3	0	2	0.353452	0.353278	0.000174	0.3535472	0.3473199	0.006227
4	0	3	0.362818	0.365223	-0.002405	0.3629127	0.3592969	0.003616
5	0	4	0.379279	0.381947	-0.002668	0.3793755	0.3760269	0.003349
6	0	5	0.400257	0.403449	-0.003192	0.4003546	0.3974759	0.002879
7	0	6	0.425905	0.429729	-0.003824	0.4260047	0.4235979	0.002407
8	0	7	0.456121	0.460787	-0.004666	0.4562228	0.4543399	0.001883
9	<b>1</b>	0	0.462009	0.550546	<b>-0.088537</b>	0.4621111	0.4698269	<b>-0.007716</b>
10	<b>1</b>	1	0.462292	0.552900	<b>-0.090608</b>	0.4623934	0.4722269	<b>-0.009834</b>
11	<b>1</b>	2	0.477640	0.559962	<b>-0.082322</b>	0.4777465	0.4794239	<b>-0.001678</b>
12	0	8	0.486861	0.496624	-0.009763	0.4869664	0.4896409	-0.002675
13	<b>1</b>	3	0.490829	0.571732	<b>-0.080903</b>	0.4909338	0.4913999	<b>-0.000466</b>
14	<b>2</b>	0	0.499818	0.592906	<b>-0.093088</b>	0.4999147	0.4984539	<b>0.001461</b>
15	<b>2</b>	1	0.500070	0.595335	<b>-0.095264</b>	0.5001664	0.5008549	<b>-0.000689</b>
16	<b>1</b>	4		0.588209	<b>-0.085007</b>	0.5032023	0.5081299	<b>-0.004928</b>
17	<b>2</b>	2		0.602622	<b>-0.085605</b>	0.5170171	0.5080509	<b>0.008966</b>
18	<b>2</b>	3		0.614767	<b>-0.090893</b>	0.5238741	0.5200269	<b>0.003847</b>
19	<b>1</b>	5		0.609394	<b>-0.082916</b>	0.5264781	0.5295789	<b>-0.003101</b>
20	0	9		0.537238	-0.007176	0.5300623	0.5294299	0.000632
21	<b>2</b>	4		0.631769	<b>-0.088218</b>	0.5435514	0.5367579	<b>0.006793</b>
22	<b>1</b>	6		0.635287	<b>-0.086140</b>	0.5491468	0.5557009	<b>-0.006554</b>
23	<b>2</b>	5		0.653630	<b>-0.088361</b>	0.5652690	0.5582069	<b>0.007062</b>
24	0	10		0.582631	-0.009104	0.5735271	0.5736319	-0.000105
25	<b>2</b>	6		0.680348	<b>-0.101435</b>	0.5789125	0.5843289	<b>-0.005416</b>
26	<b>1</b>	7		0.665888	<b>-0.083962</b>	0.5819257	0.5864439	<b>-0.004518</b>
27	3	0				0.5822055	0.5969889	-0.014783
28	3	1				0.5918391	0.5993899	-0.007551
29	3	2				0.5973373	0.6065859	-0.009249
30	3	3				0.6064520	0.6185619	-0.012110

**Table 4.8:** Lowest-lying rovibrational energy levels of HO<sub>2</sub> for total angular momentum  $J = 50$ , with odd permutation symmetry and odd parity. All energies are in eV, and relative to the vibrational ground state. Previous results from S. Smith *et al.*<sup>9</sup> are also presented. New energies are converged to  $10^{-6}$  eV or better; they agree with Ref. [9] to within  $10^{-4}$  eV or better. Column II: our  $K$  assignments (agree with Ref. [9]).

$n$	$K$	Smith/LSFD	This Work
1	0	0.346874	0.3469657
2	1	0.349929	0.3500197
3	2	0.363344	0.3634372
4	3	0.379251	0.3793441
5	4	0.400258	0.4003535
6	5	0.425905	0.4260027
7	6	0.456121	0.4562208
8	7	0.471153	0.4712573
9	0	0.474154	0.4742577
10	1	0.487383	0.4874881
11	2	0.490829	0.4909319
12	8	0.503052	0.5031584
13	3		0.5100281
14	0		0.5129769
15	1		0.5238724
16	4		0.5271237
17	2		0.5300602
18	3		0.5435117
19	5		0.5491461
20	9		0.5652686
21	4		0.5735251
22	6		0.5789117
23	5		0.5909422
24	10		0.5918373
25	6		0.5939130
26	7		0.6069630
27	0		0.6130795
28	1		0.6212435
29	2		0.6224414
30	3		0.6231530

ing appears to be that these are not very reliable, particularly for large  $J$  or large vibrational excitation. In this regime, the flexibility of HO<sub>2</sub>—particularly the low transition state barriers to isomerization<sup>9;64;76</sup>—contributes to substantial HC breakdown. Some might argue that since the DMBE IV PES is not accurate at high energies, evaluating HC breakdown there is not relevant; however, for purely *theoretical* investigations—e.g., the comparison vs. exact quantum results that will be conducted here—this PES should serve perfectly well.

With regard to bound rovibrational state calculations, S. Smith and coworkers conclude that by  $J = 50$ , the validity of the label  $K$  is becoming suspect, and even vibrational assignment is only possible for the very lowest-lying excitations.<sup>9</sup> As a result, JS—even VSD JS—is unreliable, particularly for states that lie close to one another, for which  $K$ -mixing is especially pronounced. Another important observation, made by J. M. Bowman some years ago,<sup>48</sup> is that “as  $J$  and  $K$  increase, the states that were bound states become resonances”—a particularly nettlesome phenomenon, vis-à-vis JS, that will be taken up again in Section 4.5.3.

Recent HO<sub>2</sub> work pertaining to application of JS in the reactive scattering context also bears comment. The most recent and accurate calculations by H. Guo and coworkers<sup>66;69–72</sup> again suggest that JS is ineffective. Though less accuracy is required in the reactive scattering context, the inherent high energies and molecular rearrangements pose their own problems. In addition, since the reaction involves a stable intermediate, there is also the fundamental problem—raised years earlier by J. M. Bowman<sup>48</sup>—of which geometry should be used for JS: the transition state, or the HO<sub>2</sub> intermediate minimum? There is one research group<sup>53;54</sup> that claims that the O–OH transition state leads to a viable JS strategy—one which, moreover, is alleged to work *better* at higher excitation energies. By their own admission, however, these conclusions are “controversial;” in any event, they performed no  $J > 0$  calculations (and used a different PES), drawing their conclusions directly from comparison with experiment.

In contrast, H. Guo and coworkers argue that JS must *inherently* fail for HO<sub>2</sub> reactive scattering applications, because the form of the energy dependence of the scattering quantities is very different from one  $J$  value to the next.<sup>71;72</sup> (As a side note, they also find, interestingly, that quasiclassical trajectories yield poor predictions for

overall cross sections but good predictions of relative product state distributions). As a basic, inherent requirement for the success of JS, the energy-dependent curves for different  $J$  values must closely resemble each other, apart from an energetic shift (although in practice, whether the shift energies may be accurately estimated *a priori* is another matter...). As this is not the case for HO<sub>2</sub>, that would seem to definitively rule out using any JS scheme reliably in this context.

On the other hand, Figure 4.1 suggests that there is indeed hope for the HO<sub>2</sub> bound rovibrational states—and moreover, one that may achieve some success throughout the *entire*  $10 \leq J \leq 120$  range! In the figure, each curve represents the lowest-lying 30 exact rovibrational energies (of even parity) for a given  $J$  value, presented in energetic order—as in Section 4.5.1, but without regard to any other considerations such as state labeling. As is very evident from the figure, *these curves do indeed resemble one another*, apart from an energetic shift. Moreover, the shift energy appears to be roughly quadratic in  $J$ —i.e., exactly what one would expect, based on Equation 4.6. It is perhaps surprising that this basic pattern persists across the entire  $J$  range—even where HC breakdown is undoubtedly very severe, and for rotational energies that are nearly sufficient to dissociate the molecule. That said, we note that the states in Figure 4.1 are all low-lying with respect to their vibrational excitation; one cannot expect the pattern to extend to the highly-vibrationally excited rovibrational states. Also, although the resemblance is especially close for  $J \leq 50$ , the curves increasingly deviate from one another as  $J$  increases beyond this value.

Indeed, one *very* curious trend is the convergence of the  $n = 1$  and 2 energy levels with increasing  $J$ , leading to the increasingly kinked behavior evident on the left side of Figure 4.1 (and elsewhere). From the tables, the even-parity,  $J = 10$ ,  $n = 1 \rightarrow 2$  level spacing is .0022 eV—on the order of the rotational  $K$ -level spacing, which is appropriate given the respective  $K$  assignments of 0 and 1. As  $J$  increases however, the two lowest-lying energies converge exponentially quickly, so that by  $J = 120$ , they are only about  $10^{-6}$  eV apart! Obviously, the  $K$  labels are no longer so suitable for purposes of JS; but the more relevant point here is to try to establish the underlying dynamical cause of this behavior. This is still not settled—although the bound state analog of a bend-rotation Feshbach resonance is suspected (in the same manner that

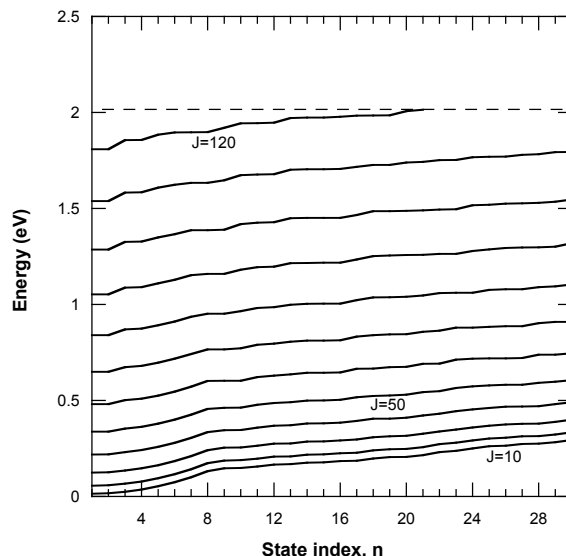


**Figure 4.1:** Lowest-lying 30 even-parity rovibrational energy levels of  $\text{HO}_2$ , as a function of state index  $n$ , for each multiple-of-ten value of total angular momentum  $J$ , from  $J = 10$ – $120$ . All energies are in eV, and relative to the vibrational ground state. The different  $J$  curves resemble each other, apart from an energy shift. Dashed line represents dissociation threshold.

double-well tunneling splitting might be regarded as the bound state analog of a shape resonance). Section 4.5.3 has additional discussion.

We will present a detailed, comprehensive analysis in the next chapter. Here, we restrict ourselves to some preliminary JS results, obtained for just the even-parity rovibrational states for  $J = 50$ . As a practical measure, application of JS requires some means of assigning  $K$  values to those rovibrational states that are being considered, despite possible HC breakdown. In Paper I, the individual  $K$  components of the computed bound rovibrational eigenstate wavefunctions with  $J \leq 10$  were consulted, in order to determine the most probable  $K$  value (and also vibrational state assignments). Such an approach is not likely feasible for the larger  $J$  values, however. Instead, we adopt the following procedure. First, all of the RSD JS rovibrational energies are computed, as per Section 4.3, and energetically ordered. These are compared to the exact  $J = 50$  eigenenergies (energy-ordered, labelled by  $n$ ), as in Figure 4.1, and found to match quite closely—apart from being systematically too large by about

$1.2 \times 10^{-3}$  eV. Methods exist for computing accurate rovibrational ground state energies for any  $J$  value, that use much less computation than would be required for excited states—e.g. Monte Carlo methods. This justifies introducing a systematic energy shift into the RSD JS predictions, so as to make the ground state prediction exact. In any event, RSD energetic ordering as described above leads to unambiguous rotational and vibrational assignments for each of the exact rovibrational states. This procedure is followed throughout this chapter and the next, leading to the  $K$  and  $v$  values as presented in Tables 4.3–4.8. These assignments are in perfect agreement with those of Paper I and of S. Smith, for the low-lying states for which S. Smith and coworkers have performed calculations. The higher-lying  $J = 10$  state labels also agree with those of Paper I—except for the even-parity  $n = 25$  and  $n = 26$   $K$  labels, which are switched.

In Table 4.7, both VSD JS and RSD JS results are presented for the  $J = 50$  even-parity states. RSD values are obtained as described above, and compared to the exact rovibrational energy levels as computed in this work. For the lowest-lying  $n \leq 15$  states, for which exact results are provided in Ref. [9], those results are used to compare with VSD predictions, also obtained from Ref. [9]. For  $n > 15$ , we have extrapolated the VSD predictions using the recipe and VSD rotor data from Ref. [9] (no  $v = 3$  data was provided, which is why states  $n = 27$ – $30$  are still missing); however, the errors are compared against the exact results from this work. Being customized for individual vibrational states, the VSD scheme is intended to provide more accurate predictions for vibrationally excited rovibrational states than a non-VSD scheme. At such a high  $J$  value, however, we find that in fact, *VSD does a fairly poor job for the vibrationally excited states*, even with just a single vibrational excitation, as indicated by the bold-faced entries in the Table. In contrast, RSD JS is remarkably consistent and accurate throughout, with most errors just a few meV. A comparison of VSD vs. RSD errors for this calculation is presented in graphical form in Figure 4.2. To enable a fair comparison, the ground-state-energy shift procedure described above for RSD, is here also applied to VSD. Whereas the predictions of the two JS procedures are quite close when there are no vibrational excitations, in general, the VSD errors are an order of magnitude or so worse than those of RSD.

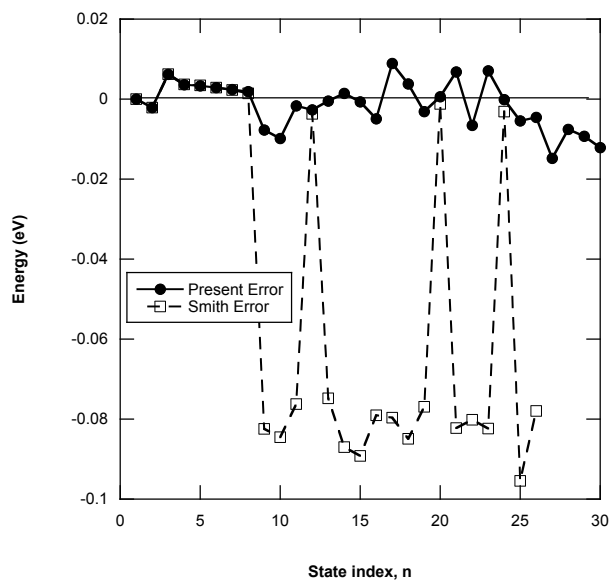


**Figure 4.2:** Error comparison for VSD (Smith) vs. RSD (our) JS, for the lowest-lying 30 rovibrational energy levels of  $\text{HO}_2$ , for total angular momentum  $J = 50$ , with odd permutation symmetry and even parity, as a function of state index  $n$ . For accurate comparison, ground-state-energy shifting has been applied to both predictions (i.e., the error for the  $n = 1$  state is zero). This convention differs from the VSD results as presented in Table 4.7 and in Ref. [9].

It thus appears that RSD JS can indeed predict the bound rovibrational states of  $\text{HO}_2$  quite successfully, even at considerably large  $J$ —provided that  $v$  and  $K$  values are fairly small. Moreover, RSD outperforms VSD, *especially* when there are vibrational excitations.

#### 4.5.3 Wavefunction Analysis of a $J = 120$ Rovibrational Bound State

The reason for RSD’s success may be understood in terms of Equation 4.7, and the role of centrifugal distortion. As total angular momentum is increased, the minimum geometry of  $V_{JK}^{\text{eff}}$  is distorted, away from that of  $V$  itself. For small  $K$ , most of this distortion is along the O–O bond—but the heaviness of the atoms limits the extent of this distortion, even for large  $J$  values. On the other hand, the  $K$  dependence of Equation 4.7 is much more pronounced, owing to the lightness of the H

atom—i.e., to the fact that  $\mu_R \ll \mu_r$  (Table 4.1). Consequently,  $V_{JK}^{\text{eff}}$  changes much more dramatically as  $K$  is increased, with the H atom pushed substantially outward from O<sub>2</sub>. Of course, this has a marked impact on the rotational constants, and on the associated RSD JS levels.

The ramifications become quite interesting in the large- $J$  and  $-K$  limit. Because the  $J$  contribution in Equation 4.7 is large for large  $J$ , the  $V_{JK}^{\text{eff}}$  potential well is greatly diminished by the  $J$  contribution alone—i.e., even for  $K = 0$ . At some point—i.e., beyond some  $K$  value—the  $K$  contribution to  $V_{JK}^{\text{eff}}$  first pushes the potential well above the dissociation threshold, and then obliterates it completely, leading in both cases to a scattering potential. This situation—well presaged by J. M. Bowman’s comment at the start of Section 4.5.2—implies that exact quantum dynamical treatment of the *bound* rovibrational states for the largest  $J$  values may actually provide some insight into the *scattering* process. In any event, use of the global minimum in RSD JS would, for the larger  $K$  values, lead to completely dissociated H+O<sub>2</sub> as the appropriate geometry—with the  $H$  atom infinitely far away from the O<sub>2</sub> diatomic, and  $\theta = \pi/2$  [from Equation 4.7]. Note that this is the “oblate top” realm, with smaller  $K$  values corresponding to more O<sub>2</sub> rotation, and therefore *larger* rotational kinetic energy values. The intriguing prospect of observing mixed prolate and oblate behavior within the  $K$  expansion for a *single* quantum dynamical state is not something that has been previously considered, to the author’s best knowledge.

To explore the above scenario, we have performed an accurate quantum dynamical calculation of the even-parity,  $J = 120$ ,  $n = 1$  rovibrational eigenstate *wavefunction*, using the **ScalIT** codes. The most telling information to extract from this wavefunction is the distribution of probability across  $K$  values—i.e.,  $\sum_{v_1, v_2, j} |C_{v_1, v_2, j, K}^{J0\epsilon}|^2$  as a function of  $K$  [with  $C_{v_1, v_2, j, K}^{JM\epsilon}$  from Equation 2.3]. The results, presented in Figure 4.3(a), exhibit a curious, alternating- $K$  structure, up to about  $K = 38$ . Beyond this point, there is no oscillation; the probability values simply peter out—steadily but gradually—with increasing  $K$ . It is thus abundantly clear that even for just this lowest-lying  $n = 1$  eigenstate, even modest  $K$  truncation will be ineffective, insofar as accurate rovibrational level calculations are concerned.

More dynamically intriguing, however, is understanding the “ $K = 38$  divide.” It turns out that this is the crossover point above which the binding-plus-rotation

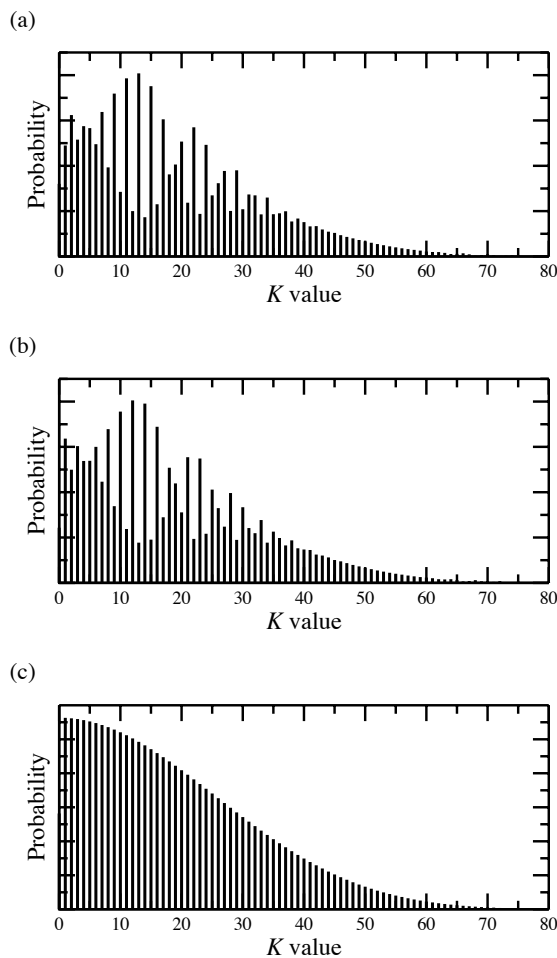


**Figure 4.3:** Distribution of probability across  $K$ , for lowest-lying rovibrational eigenstate wavefunctions of  $\text{HO}_2$ , for total angular momentum  $J = 120$ , with odd permutation symmetry and even parity: (a)  $n = 1$  eigenstate; (b)  $n = 2$  eigenstate; (c) sum of  $n = 1$  and  $n = 2$ .

energy for the bound molecule geometry exceeds the  $\text{O}_2$  diatomic rotation energy for the  $\text{H}+\text{O}_2$  dissociated molecule—as demonstrated in Figure 4.4, a plot of the rotational energy shifts,  $E_{JK}^{\text{rot}}$  as a function of  $K$ , for  $J = 120$ . Two different curves are presented: one corresponding to the bound molecule local minimum of  $V_{JK}^{\text{eff}}$ , the other to the dissociated  $\text{H}+\text{O}_2$  fragments. Due to their respective prolate/oblate natures, as discussed above, the first curve necessarily increases with  $K$ , whereas the

second necessarily decreases. There is thus an energetic crossover that occurs at some intermediate  $K$  value—which from the figure is found to be *exactly* at  $K = 38$ . Thus, the steady decay evident in Figure 4.3(a) for  $K > 38$  can be regarded as a tunneling contribution from dissociated configurations that are classically forbidden.

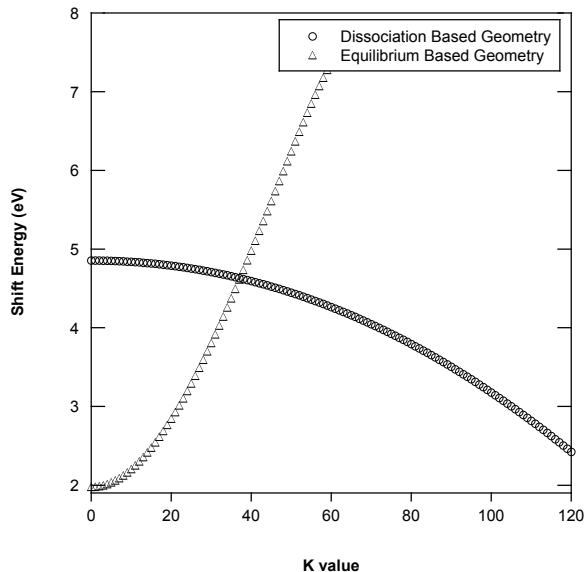


**Figure 4.4:** RSD rotational energy shifts,  $E_{JK}^{\text{rot}}$ , as a function of  $K$ , for  $J = 120$ , as computed using the method of Section 4.3 applied to the DMBE IV PES. Triangles correspond to local  $V_{JK}^{\text{eff}}$  minimum geometry associated with the bound  $\text{HO}_2$  molecule. Circles correspond to the dissociated  $\text{H} + \text{O}_2$  fragments. There is an energetic crossover between the two curves at  $K = 38$ .

Conversely, the oscillatory behavior observed in the “classical”  $K \leq 38$  region must reflect some sort of quantum interference effect. Intuition suggests that this is somehow related to the fact that the  $n = 1$  and  $n = 2$  eigenenergies are nearly identical (Section 4.5.2). Indeed, Figure 4.3(b), depicting the  $K$  distribution of probability for the  $n = 2$  state, exhibits remarkable similarity to Figure 4.3(a)—except that the oscillations are *exactly complementary*. This is demonstrated in Figure 4.3(c), in which the  $n = 1$  and  $n = 2$  distributions are summed, and the  $K$  oscillations are seen to disappear completely. In any event, whether our Feshbach-like-resonance

hypothesis is correct or not, from the figure, there can be no doubt that Coriolis coupling is directly involved.

As alluded to above, the crossover point should also provide some useful information about HO<sub>2</sub> reactivity. In particular, for highly rotationally excited HO<sub>2</sub> with  $J \geq 38$ , we expect to see a decrease in reactivity, owing to the rotational barrier that the fragments must overcome in order to get close enough to react. In Figure 1 of Ref [72]—even accounting properly for the rotational shift—one does indeed observe a substantial decrease in the cumulative reaction probability for  $J > 30$ .

As a final validation of the “effective potential” idea, we have created various wavefunction plots as a function  $(r, R, \theta)$ , for the even-parity,  $J = 120$ ,  $n = 1$  rovibrational eigenstate, evaluated at two different values of  $K$ . Being the lowest-lying eigenstate, the plots all exhibit a single narrow peak, and are otherwise “boring,” and not presented. Instead, we focus here on the geometry of maximum probability density for each  $K$  value. For  $K = 0$ , this geometry occurs at  $r_{\max} = 2.76$  a.u. and  $R_{\max} = 2.43$  a.u. As per earlier arguments, one expects the majority of the centrifugal distortion for  $K = 0$  to manifest as a modest elongation of the O–O bond. Given that  $r_{\max} = 2.51$  a.u. for the vibrational ground state, this is indeed observed to be the case. We have also analyzed the  $K = 47$  component—lying well within the “oblate” region, and for which  $V_{JK}^{\text{eff}}$  is in fact completely repulsive. An HC calculation would predict only scattering contributions at this  $K$  value, and significant probability density across an extended  $R$  range. In reality, the  $K = 47$  component of the  $n = 1$  eigenstate—like that for  $K = 0$ —is found to be narrowly peaked about its  $R_{\max}$  value. However,  $R_{\max} = 2.51$  a.u. is now elongated in comparison to the  $K = 0$  value, and  $r_{\max} = 2.51$  is now reduced to its undistorted value—both of which are consistent with a transfer of angular momentum from the body-fixed  $x$  and  $y$  components to the  $z$  component, as might be predicted from Equation 4.7.

#### 4.6 Summary and Concluding Remarks

The HO<sub>2</sub> radical continues to garner much attention in the literature. From previous work, it is clear that the rovibrationally excited states—particularly at very large  $J$ —are dynamically very important. Yet, a comprehensive calculation of the bound rovibrational eigenstates of HO<sub>2</sub>, up to the highest allowable  $J$  values, has never

been achieved before now. Specifically, QD calculations were performed here for all multiple-of-ten  $J$  values in the range  $10 \leq J \leq 130$ . These calculations are “exact,” in the sense that no  $K$  truncation or other approximations to the rovibrational quantum Hamiltonian of Equation 2.1 were applied. For each  $J$  value considered, both the even and odd parity states were computed (although the even-permutation-symmetry states are not physically allowed, and are therefore ignored).

All calculations were performed using the DMBE IV PES, and the *ScalIT* suite of parallel codes. DMBE IV is an older PES, not likely very accurate at higher energies. However, it has served as a standard benchmark for other HO<sub>2</sub> bound rovibrational state calculations—which, to the author’s best knowledge, have only previously been performed up to  $J = 50$ .<sup>9</sup> For the high convergence accuracies achieved in this study—i.e.,  $10^{-6}$  eV or better for all computed energy levels—there can be no doubt that the “accuracy bottleneck” of the overall calculation is the DMBE IV PES. Future work may see similar calculations applied to more accurate HO<sub>2</sub> PESs, such as “XXZLG”<sup>67</sup> or one of its variants. From a computational standpoint, all indications are that such calculations would be *less* challenging than those performed here, owing to the reduced DOS.<sup>64;75</sup> Note also that previous DOS work has focused on the vibrational rather than the rovibrational DOS, yet it is the latter that is of greater practical importance. Accordingly, we may also perform our own rovibrational DOS study in future.

For purposes of addressing the efficacy of the *ScalIT* parallel quantum dynamics codes as applied to triatomic molecules at very large  $J$ , use of the DMBE IV PES is entirely justified. The fact that we were able to effectively parallelize even a comparatively “small” (from a massively parallel standpoint) problem such as  $J = 120$  HO<sub>2</sub> across one hundred *nodes* (twelve cores each) is highly encouraging—although this did involve a bit of “tweaking,” and exposed some unexpected issues. On the other hand, running across a more modest five nodes (60 cores) presented no special consideration or difficulties whatsoever, and resulted in typical MPI wall times well under one hour per job. Moreover, it must be emphasized that all *ScalIT* jobs were executed here in the manner of a “non-expert” user—i.e., by using only default algorithms and high-level modules, and paying little explicit attention to optimization. Almost anyone—following the “recipe” described in Appendix A and provided with access

to a modest-sized cluster—could have duplicated the results obtained here. Together with Paper I, this work is thus intended to demonstrate the viability and robustness of *ScalIT* as an effective computational tool for non-expert users from the general chemical dynamics field—as opposed, e.g., to various previous numerically-oriented investigations.<sup>1-4</sup>

At the same time, HO<sub>2</sub> also serves as an ideal testbed for parallel QD methodologies, because: (a) many previous studies are available in the literature; (b) such calculations, especially for the rovibrational states, are still considered extremely challenging; (c) certain dynamical features such as HC breakdown are still poorly understood; (d) other parallel methods have been applied to this system. Whereas Paper I focused more on (d), in this chapter, it is (c) that has been primarily emphasized. Given that the JS and HC approximations are *theoretical* models, it is our view that any honest assessment of these techniques requires comparison with exact rovibrational spectroscopy calculations performed using the same PES—rather than, say, via comparison with experiment. We have endeavored to provide just such an assessment here, at least for our RSD JS method (in which context, also, the use of the DMBE IV PES is entirely justified). In contrast, the VSD JS predictions rely on experimental VSD rotational constants, which may indeed help to explain why this approach behaves so poorly when applied at very large  $J$  values—i.e., well outside the range of the experimental fitting parameters.

On the other hand, it is *precisely* the large- $J$  regime that presents the greatest topical interest—and computational challenges—for the HO<sub>2</sub> system. In this chapter, we confirm the conclusion reached by many previous researchers, that HO<sub>2</sub> at large  $J$  experiences *severe* Coriolis coupling and HC breakdown. For this reason (and also because the HC approximation is embedding-dependent), we did not deem it fruitful to perform any HC calculations here. Yet remarkably, Figure 4.1 indicates that the vibrationally low-lying rovibrational energy levels are indeed characterized by some sort of JS, across the entire  $J$  range. Moreover our particular RSD JS scheme is found to yield surprisingly accurate predictions for the rotational energy shifts, even for considerably large  $J$ . We deem this to be a sufficiently important finding as to justify a whole other article addressing this theme alone.

The underlying dynamical picture upon which RSD JS is based—i.e., that of the three-body “effective potential,” consisting of the true potential plus a centrifugal correction, in exact analogy with the familiar two-body case—is further found to provide additional benefits. In particular, this description yields important dynamical insight into the  $K$ -structure of the exact quantum dynamical rovibrational eigenstate wavefunctions, even at the very highest  $J = 120$  value for which such states are (now) known to exist. Almost unused since its invention in 1998,<sup>82;83;91</sup> despite exhibiting substantial promise, the three-body effective potential idea—conceptually simple, yet practically useful—will, it is to be hoped, be adopted by other researchers, going forward.

It is also to be hoped that the utility, efficiency, and ease-of-use of *ScalIT*—as have by now been amply demonstrated<sup>1-4;11;25-27</sup>—will also attract converts, going forward. These might include non-experts such as experimentalists, who have a practical need to compute accurate rovibrational state data reliably and quickly, as well as the more “expert” QD practitioner, with the desire to introduce massively parallel functionality into his or her existing code base. For either type of user, both the *ScalIT* package itself, and the associated documentation, will be made available from the Poirier group on request.

**Table 4.9:** Lowest-lying 125 rovibrational energy levels of HO<sub>2</sub> for total angular momentum  $J = 50$ , with odd permutation symmetry and even parity. All energies are in eV, and relative to the vibrational ground state. Energies are converged to  $10^{-6}$  eV or better.

$n$	Energy								
1	0.3377239	26	0.5819257	51	0.6972612	76	0.7771876	101	0.8255161
2	0.3380129	27	0.5822055	52	0.6978582	77	0.7773717	102	0.8321959
3	0.3535472	28	0.5918391	53	0.6981385	78	0.7777674	103	0.8323362
4	0.3629127	29	0.5973373	54	0.6982265	79	0.7786029	104	0.8345098
5	0.3793755	30	0.6064520	55	0.6998362	80	0.7827856	105	0.8391353
6	0.4003546	31	0.6130744	56	0.7130283	81	0.7833484	106	0.8439770
7	0.4260047	32	0.6212383	57	0.7138427	82	0.7857187	107	0.8448200
8	0.4562228	33	0.6224480	58	0.7210979	83	0.7888526	108	0.8452965
9	0.4621111	34	0.6231479	59	0.7220653	84	0.7910431	109	0.8500331
10	0.4623934	35	0.6238717	60	0.7290518	85	0.7944307	110	0.8500982
11	0.4777465	36	0.6241375	61	0.7310211	86	0.7953825	111	0.8514417
12	0.4869664	37	0.6408178	62	0.7378960	87	0.7954248	112	0.8528856
13	0.4909338	38	0.6429098	63	0.7407083	88	0.8022355	113	0.8564731
14	0.4999147	39	0.6499652	64	0.7433171	89	0.8027719	114	0.8587294
15	0.5001664	40	0.6515416	65	0.7435628	90	0.8050560	115	0.8591698
16	0.5032023	41	0.6522968	66	0.7438783	91	0.8066598	116	0.8594119
17	0.5170171	42	0.6524324	67	0.7452464	92	0.8105873	117	0.8621204
18	0.5238741	43	0.6591535	68	0.7494155	93	0.8108701	118	0.8667870
19	0.5264781	44	0.6668068	69	0.7537549	94	0.8111544	119	0.8681210
20	0.5300623	45	0.6678602	70	0.7539767	95	0.8119071	120	0.8700097
21	0.5435514	46	0.6705960	71	0.7580703	96	0.8145130	121	0.8704280
22	0.5491468	47	0.6731157	72	0.7601341	97	0.8156824	122	0.8757258
23	0.5652690	48	0.6803139	73	0.7690520	98	0.8220822	123	0.8760311
24	0.5735271	49	0.6880384	74	0.7691344	99	0.8222201	124	0.8786040
25	0.5789125	50	0.6941553	75	0.7700454	100	0.8226380	125	0.8788423

**Table 4.10:** Lowest-lying rovibrational energy levels of HO<sub>2</sub> for total angular momentum  $J = 60, 70$  and  $80$ , with odd permutation symmetry and both even and odd parity. All energies are in eV, and relative to the vibrational ground state. Energies are converged to  $10^{-6}$  eV or better.

Index $n$	$J = 60$		$J = 70$		$J = 80$	
	Even	Odd	Even	Odd	Even	Odd
1	0.4814901	0.4936133	0.6491905	0.6641582	0.8399739	0.8575764
2	0.4816210	0.4955593	0.6492474	0.6652779	0.8399982	0.8581734
3	0.5015303	0.5106492	0.6741319	0.6829679	0.8701106	0.8793496
4	0.5092875	0.5257061	0.6801388	0.6966951	0.8744290	0.8913221
5	0.5258254	0.5464917	0.6970475	0.7172339	0.8921998	0.9116478
6	0.5464906	0.5718998	0.7172134	0.7423246	0.9115790	0.9363206
7	0.5719037	0.6018736	0.7423253	0.7719934	0.9363237	0.9656150
8	0.6018772	0.6144506	0.7661060	0.7808957	0.9521959	0.9695828
9	0.6024624	0.6163612	0.7661615	0.7819958	0.9522198	0.9701711
10	0.6025900	0.6312379	0.7719935	0.7994293	0.9656160	0.9910254
11	0.6222570	0.6363225	0.7907274	0.8061200	0.9819284	0.9993508
12	0.6298900	0.6460665	0.7966403	0.8129509	0.9861872	1.0028352
13	0.6363262	0.6574325	0.8061204	0.8287395	0.9993517	1.0226638
14	0.6441957	0.6592238	0.8124394	0.8296911	1.0035137	1.0229220
15	0.6442852	0.6665640	0.8124645	0.8332291	1.0038461	1.0236190
16	0.6462110	0.6751653	0.8133694	0.8446148	1.0040481	1.0374275
17	0.6659037	0.6753307	0.8331609	0.8488220	1.0227965	1.0463220
18	0.6666606	0.6906816	0.8397022	0.8579384	1.0367250	1.0473855
19	0.6736728	0.6916002	0.8446149	0.8626050	1.0374280	1.0582383
20	0.6751689	0.7121553	0.8454300	0.8837607	1.0406569	1.0760558
21	0.6908349	0.7183141	0.8579370	0.8870374	1.0472392	1.0779360
22	0.6916033	0.7211293	0.8630625	0.8875252	1.0593684	1.0785207
23	0.7121529	0.7309068	0.8789902	0.8935658	1.0607997	1.0791489
24	0.7183178	0.7328030	0.8790462	0.8946616	1.0608236	1.0797983
25	0.7190904	0.7384012	0.8837347	0.9095891	1.0760602	1.0990233
26	0.7192172	0.7474613	0.8870382	0.9118186	1.0790452	1.1044271
27	0.7211319	0.7550529	0.8875256	0.9207957	1.0797976	1.1093425
28	0.7384048	0.7621142	0.9032323	0.9251951	1.0900649	1.1107478
29	0.7385900	0.7656972	0.9090944	0.9343571	1.0943068	1.1262282
30	0.7461439	0.7693726	0.9095954	0.9401463	1.1044314	1.1304655

**Table 4.11:** Lowest-lying rovibrational energy levels of HO<sub>2</sub> for total angular momentum  $J = 90, 100, 110,$  and  $120$ , with odd permutation symmetry and both even and odd parity. All energies are in eV, and relative to the vibrational ground state. Energies are converged to  $10^{-6}$  eV or better.

Index $n$	$J = 90$		$J = 100$		$J = 110$		$J = 120$	
	Even	Odd	Even	Odd	Even	Odd	Even	Odd
1	1.0527646	1.0727613	1.2862321	1.3083913	1.5387803	1.5628593	1.8084129	1.8341889
2	1.0527750	1.0730654	1.2862365	1.3085427	1.5387826	1.5629348	1.8084138	1.8342270
3	1.0880158	1.0983892	1.3262269	1.3383553	1.5829690	1.5972234	1.8562077	1.8726571
4	1.0908934	1.1083506	1.3280212	1.3462515	1.5840391	1.6031913	1.8568321	1.8769781
5	1.1101888	1.1285859	1.3495601	1.3666311	1.6084220	1.6240569	1.8844073	1.8987298
6	1.1283943	1.1527028	1.3661755	1.3900006	1.6231154	1.6464247	1.8964023	1.9196835
7	1.1527130	1.1794281	1.3872855	1.4091834	1.6335515	1.6573621	1.8966446	1.9221974
8	1.1596826	1.1797273	1.3872942	1.4093334	1.6335582	1.6574344	1.8972683	1.9223523
9	1.1596930	1.1815609	1.3900444	1.4183248	1.6465263	1.6741444	1.9200244	1.9468522
10	1.1815473	1.2046520	1.4183070	1.4386491	1.6740571	1.6911311	1.9437080	1.9599986
11	1.1944483	1.2144154	1.4267433	1.4464852	1.6772137	1.6971176	1.9444647	1.9644190
12	1.1972987	1.2149107	1.4285334	1.4510575	1.6782649	1.7062219	1.9470934	1.9781496
13	1.2148005	1.2344250	1.4496297	1.4665997	1.7021305	1.7177424	1.9715151	1.9859772
14	1.2162542	1.2388514	1.4510834	1.4751764	1.7043515	1.7302425	1.9739670	2.0016423
15	1.2172381	1.2391300	1.4512666	1.4753157	1.7043870	1.7303236	1.9740194	2.0017539
16	1.2173111	1.2523802	1.4513134	1.4877921	1.7062253	1.7395368	1.9780858	2.0065244
17	1.2342732	1.2582805	1.4661834	1.4899774	1.7168718	1.7429449	1.9840017	2.0096983
18	1.2523765	1.2668447	1.4859224	1.5074832	1.7267415	1.7502299	1.9844189	2.0098412
19	1.2555899	1.2762927	1.4859354	1.5075924	1.7267532	1.7503042	1.9848819	2.0141350
20	1.2576888	1.2829851	1.4877945	1.5081100	1.7396041	1.7671933	2.0067433	
21	1.2587155	1.2832858	1.4899775	1.5151020	1.7429516	1.7678282	2.0141272	
22	1.2635146	1.2867260	1.4946360	1.5177889	1.7520550	1.7731301		
23	1.2635259	1.2942385	1.4961654	1.5292689	1.7529209	1.7830725		
24	1.2786318	1.2971337	1.5174676	1.5361674	1.7670906	1.7833539		
25	1.2867171	1.3077577	1.5195195	1.5365266	1.7697871	1.7893109		
26	1.2942356	1.3175297	1.5247792	1.5443134	1.7708253	1.7948157		
27	1.2968395	1.3196106	1.5266016	1.5500856	1.7795370	1.7992365		
28	1.2977552	1.3217059	1.5292687	1.5598208	1.7830772	1.8096838		
29	1.3005963	1.3372550	1.5356406	1.5642454	1.7930621	1.8172147		
30	1.3191352	1.3400808	1.5473471	1.5743792	1.7945925	1.8239492		

## CHAPTER 5

*J*-SHIFTING STRATEGIES AS APPLIED TO THE HO<sub>2</sub> MOLECULE<sup>1</sup>

## 5.1 Introduction

The proliferation of computational resources and sophisticated codes has made the calculation of “exact” quantum dynamical quantities such as vibrational spectra more accessible, despite the inherent numerical challenges. Nevertheless, in the context of bound *rovibrational* spectroscopy, such calculations can still be extremely difficult<sup>96;97</sup>—especially if the total angular momentum quantum number,  $J$ , is large. To simplify such calculations, approximations that separate rotational and vibrational motions are often used. HC method, for example, adopts a relatively mild adiabatic approximation, for which the vibrational motion quantum states depend parametrically on the rotational quantum numbers.<sup>98–100</sup> The simpler and more popular JS strategy as discussed in the previous chapter uses a much more severe “completely” separable approximation, for which vibrational and rotational energy components are purely additive.<sup>96</sup> Variations of these two basic approaches can also be found.<sup>9;48;81</sup>

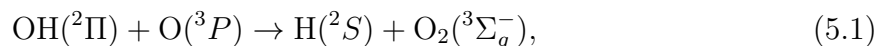
Although the JS approximation is expected to be less accurate than HC, neither is expected to fare well when Coriolis coupling is substantial. This is the case for floppy molecules such as HO<sub>2</sub>—though it should be noted that *all* molecules become floppy for sufficiently large  $J$ . At any rate, HO<sub>2</sub>, particularly at large  $J$ , serves as a severe test case for analyzing HC and JS type methods—even though it is only a triatomic system—owing to its extensive Coriolis coupling.<sup>7–9;17;18;48;66;68–72</sup>

In this chapter, we compare various JS schemes. The goal is to systematically evaluate and improve upon existing JS methods, as well as to determine whether (and to what extent) *any* JS method may be expected to “work” in such an extremely challenging context. Paper I<sup>25</sup> addressed the lower  $J$  values of HO<sub>2</sub>, up to  $J = 10$ . Chapter 4 presented exact results for states rotationally excited all the way to the dissociation threshold ( $J < 130$ ) and also introduced a new JS scheme. Surprisingly, the latter was found to be remarkably accurate, even up to very large  $J$  values where Coriolis coupling becomes very substantial. It was this success that inspired the present, comprehensive comparison.

---

<sup>1</sup>This chapter has been reprinted and adapted for this dissertation from Ref. [10]

There is much existing HO<sub>2</sub> literature, both theoretical and experimental.<sup>6-9;25;35;90</sup> This system holds intrinsic interest for its role as an important radical intermediate in combustion reactions such as



but it has also been specifically targeted because of its Coriolis coupling, allowing it to serve as a rigorous benchmark for HC and JS methods.<sup>6-9</sup> All such previous work has been limited, however, with respect to the  $J$  range for which accurate computed rovibrational data was (previously) available. With the new results from Paper II, this former limitation is now removed—making it possible to use the largest- $J$  HO<sub>2</sub> states as an even more extreme benchmark for HC and JS methods.

To this end, it is important to distinguish empirical, semi-empirical, and theory-based JS methods and analysis techniques. Our philosophy is always to compare apples to apples; for a given PES and corresponding known exact theoretical vibrational spectrum, we evaluate how well a given JS scheme predicts the corresponding exact theoretical *rovibrational* spectrum. We are thus interested in JS as a *predictive* tool—not merely something to be fit *a posteriori* to accurate rovibrational spectra, obtained using other means. We thus never resort to experimental data, except when comparing our results with those of previous authors. For the same reason, we are not too concerned that the PES used here (DMBE IV;<sup>44</sup> see Papers I and II) is not an especially accurate one, particularly for the very highly rovibrationally excited states considered.

## 5.2 Theory and Background

For a rotating molecule, there are three rotational quantum numbers,  $J$ ,  $K$ , and  $M$ .<sup>13;25</sup>  $J$  and  $M$  are good quantum numbers, which can be used as rigorous labels for the rovibrational states. Note that  $M$  merely labels different degenerate states of the same energy level; thus, this label is unnecessary. In contrast to  $J$  and  $M$ , the body-fixed  $z$ -axis angular momentum projection,  $K$ , is *not* a good quantum number. Moreover, the definition of  $K$  itself depends on the choice of rovibrational coordinates and associated body-fixed frame. For any such choice, however, there is always non-zero Coriolis coupling that induces transitions across different  $K$  values.

If Coriolis coupling is sufficiently small, it is legitimate to use  $K$ , also, as a quantum state label. This implies an association of a specific “symmetric rotor” state,  $|JKM\rangle$ , with every rovibrational state. Interestingly, it is always a symmetric rotor that is obtained in this fashion, even if the equilibrium geometry is asymmetric. In any event, this symmetric rotor state assignment breaks down as Coriolis coupling increases, which correlates to increasing  $J$ .

To compute exact rovibrational states, a separate calculation is performed for each  $J$  value. The computational effort scales at least as  $(J + 1)^2$ . Thus, computing the rovibrational states for  $J = 100$ , say, requires a tremendous numerical effort, compared to that required for the  $J = 0$  (vibrational) states. However, for many realistic molecules (even the relatively small  $\text{HO}_2$ ), such high  $J$  values are dynamically relevant, and must therefore be considered. Traditionally, approximations have been used.

The HC approximation is defined by simply ignoring the Coriolis coupling; the resultant uncoupled  $(J, K)$  blocks of the Hamiltonian are then each solved independently, with a numerical effort that is in each case comparable to that of the vibrational problem. The cruder JS approximation requires only that the vibrational spectrum [(0, 0) HC block] be computed explicitly. To each vibrational energy, a pure rotational energy shift is added, based on the presumed  $(J, K)$  values of the corresponding rovibrational state. In a sense, then, JS tries to approximate the quantum mechanical difference between the  $(J, K)$  and (0, 0) HC blocks.

Almost invariably, JS methods presume a symmetric rigid rotor form for the rotational energy shift, which leads to the following JS energy level predictions:

$$E_{vJK}^{J\text{-shift}} = E_v + E_{JK}^{\text{rot}}, \quad \text{where} \quad (5.2)$$

$$E_{JK}^{\text{rot}} = (A - B)K^2 + BJ(J + 1), \quad (5.3)$$

$E_{vJK}^{J\text{-shift}}$  is the JS approximation energy,  $E_v$  is the vibrational energy, and  $E_{JK}^{\text{rot}}$  is the rotational shift energy. The latter depends on the two rotational constants,  $A$  and  $B$ , and on the rotational state labels,  $(J, K)$ . For a highly prolate symmetric rotor, as is presumed here for  $\text{HO}_2$ ,  $A \gg B$ .<sup>6–9;25;35</sup>

We investigate different strategies for choosing the constants  $A$  and  $B$ , thereby defining different JS strategies. Keeping the above HC discussion in mind, we will also

consider broader forms for the rotational shift energy than the symmetric rotor form of Eq. (5.3). Having specified a set of candidate JS methods, we then compare the results to the exact rovibrational energies from Papers I and II. Note that any such comparison requires a scheme for assigning  $(v, K)$  labels to the exact rovibrational states. In this study, we use labels as defined in Paper II. Alternatively, if no labels are known *a priori*, then JS can also be used to assign them—using an approach that is introduced and discussed herein.

If only *ab initio* rotational constants are to be used (i.e., no empirical data), then the simplest approach is to obtain  $A$  and  $B$  from the equilibrium ground state geometry for the particular PES used. For a highly prolate but non-linear molecule such as HO<sub>2</sub>, one obtains, in this fashion, one large rotational constant, plus two small rotational constants whose values are very close to each other. The “top” is thus not perfectly symmetric; however, reasonable symmetric values can be obtained by averaging the two small constants. The resultant  $A$  and  $B$  values are then used in Eq. (5.3). We denote this approach the “Simple” JS method.

Though the HO<sub>2</sub> rotor itself is nearly symmetric, a general triatomic molecule will not be; thus it is not clear how one should obtain symmetric rotor constants for use in Eq. (5.3). In retrospect, it is somewhat surprising that more fuss has not been made about this general incompatibility. We now introduce a new approach that addresses this, at least for light-heavy-heavy triatomics. The idea is to treat the light atom not as a point particle, but as a one-dimensional “ring,” centered on the axis defined by the two heavy atoms. This is justified by the observation that azimuthal rotational motion of the light atom is much more readily accessible, quantum mechanically, than is, say, vibrational motion of the two heavy atoms. Of course, it also leads to a geometrical object that is a *de facto* symmetric rotor. In this fashion, any asymmetric rotor geometry can be converted into a symmetric ring structure. In this chapter, for each JS method that uses asymmetric molecular geometries, a symmetric “ring” variant will also be considered. For the equilibrium geometry, the ring variant is called “Simple (R).”

To gain improved performance beyond the fixed rotational constants of the Simple methods, it is common in spectroscopic analysis to define a separate set of rotational constant values for each vibrational state. The resultant VSD rotational con-

stants,  $A(v)$  and  $B(v)$ , are expected to perform better for more highly vibrationally excited rovibrational states. Of course, one still needs to specify values for  $A(v)$  and  $B(v)$ . The Smith group has applied one such VSD JS scheme to  $\text{HO}_2$ ,<sup>6–9</sup> using rotational constants derived from earlier experimental work done by J. B. Burkholder and coworkers<sup>101</sup>.

The remaining JS methods to be evaluated in this chapter all derive their rotational constant values from the rotational states themselves; we therefore refer to these as rotational state dependent (RSD) methods.<sup>35</sup> B. Poirier introduced the first RSD JS method in 1998,<sup>102</sup> adopting the aforementioned philosophy that JS methods serve as approximations to HC methods. The basic procedure is outlined below.

After overall translational DOFs are removed, one is left with many possibilities for defining the remaining rovibrational coordinates. An important part of this procedure is determining a rotational “gauge”—*i.e.*, the body-fixed frame. Typically, the gauge is chosen so as to minimize, or at least reduce, Coriolis coupling. For light-heavy-heavy triatomics such as  $\text{HO}_2$ , the body-fixed  $z$ -axis is usually chosen to lie along the bond of the two heavy atoms. As discussed above, in the HC approximation, this leads to a  $(J, K)$  block that is identical to the  $(0, 0)$  block, except that the potential  $V$  is replaced with the following effective potential:<sup>102</sup>

$$V_{\text{eff}}(R, r, \theta, J, K) = V(R, r, \theta) + \frac{\hbar^2 J(J+1)}{2\mu_r r^2} + \left( \frac{1}{2\mu_R R^2 \sin^2 \theta} + \frac{\cot^2 \theta - 1}{2\mu_r r^2} \right) \hbar^2 K^2, \quad (5.4)$$

where  $V(R, r, \theta)$  is the PES, and the coordinates  $(R, r, \theta)$  are defined as follows:<sup>35</sup>  $r$  is the O–O interatomic distance;  $R$  is the distance between H and the  $\text{O}_2$  center of mass;  $\theta$  is the angle between the two vectors  $\vec{r}$  and  $\vec{R}$ .

Note that the “centrifugal potential” contribution to  $V_{\text{eff}}$  (last two terms) has the symmetric rotor form of Eq. (5.3)—with coordinate-dependent values for  $A$  and  $B$ . To completely decouple rotation from vibration (*i.e.*, to specify appropriate  $A$  and  $B$  constants) using Eq. (5.4), one must select appropriate reference geometry values for  $(R, r, \theta)$ . One natural approach is to define this geometry to be the minimum of  $V_{\text{eff}}$ , for a given  $J$  and  $K$ .<sup>35;102</sup>  $E_{JK}^{\text{rot}}$  is then determined as the value of  $(V_{\text{eff}} - V)$  at the reference geometry. Since the reference geometry depends on  $J$  and  $K$ , this

approach naturally incorporates centrifugal distortion and other RSD effects. We hereafter refer to it as the “Effective Potential” (EP) method.

In Chapter 4, a modification on the original EP method was introduced, in which  $E_{JK}^{\text{rot}}$  is defined as the difference between the minima for the two potentials, *i.e.*  $E_{JK}^{\text{rot}} = [\min(V_{\text{eff}}) - \min(V)]$ . Note that the two potential minima correspond to different geometries, as a consequence of which  $E_{JK}^{\text{rot}}$  no longer has the simple form of Eq. (5.3). This will be referred to as the “modified Effective Potential” (modEP) method.

For the purpose of computing RSD  $A$  and  $B$  values, rather than placing the  $\min(V_{\text{eff}})$  reference geometry values into Equation 5.4, one could simply use this geometry itself to obtain the rotational constants directly, à la the Simple JS scheme. This approach has the conceptual advantage that it incorporates centrifugally distorted moments of inertia directly into the  $E_{JK}^{\text{rot}}$ . We refer to this scheme as “geoEP”; the ring variant is “geoEP (R).” The various attributes of the six JS methods described above are summarized in Table 5.1.

### 5.3 Results and Discussion

The various JS methods defined in Section 5.2 were used to predict the 30 lowest-lying rovibrational energies of  $\text{HO}_2$ , for each of three representative total angular momentum values,  $J = 10, 50, 100$ . The three  $J$  values span the range over which  $\text{HO}_2$  exhibits bound rovibrational states ( $J < 130$ ; see Chapter 4). Roughly speaking, they correspond to regimes where the prospect of  $K$  labeling is, respectively, well suited, mildly suited, and ill suited. A plot of all errors, relative to the exact rovibrational energies of Papers I and Chapter 4, can be seen in Figure 5.1; the corresponding RMS values can be found in Table 5.2. The same information as Figure 5.1 broken out into vibrational bands can be viewed in Figures 5.2, 5.3, and 5.4. The level spacing and energy range are such that the same  $(v, K)$  labels apply for all three  $J$  values—although any labeling scheme becomes highly suspect by  $J = 100$ .

Table 5.3, Table 5.4, and Table 5.5 report individual errors for each of the 30 energy levels considered for  $J = 10, 50, 100$ , respectively, for all JS methods tested. Exact results from Chapter 4 are also reported (column IV), as are empirical VSD JS results from the Smith group<sup>9</sup> (column XI). As  $\text{HO}_2$  is a prolate rotor, the lowest-

**Table 5.1:** Table summarizing the various attributes of each JS method

Attribute	Simple	Simple(R)	modEP	EP	geoEP	geoEP(R)
symmetric rotor based	×	✓	×	×	×	✓
geometry based	✓	✓	×	×	✓	✓
Eq. (3) form	✓	✓	×	✓	✓	✓
RSD method	×	×	✓	✓	✓	✓
effective potential based	×	×	✓	✓	✓	✓

lying state for each  $J$  block should correspond to ( $v = 0, K = 0$ ). For improved accuracy, and in order to establish a baseline for comparison, an additional shift of ( $E_{0J0} - E_{0J0}^{J\text{-shift}}$ ) was added to Eq. (5.2) for each computed JS level. This is justified by the assumption that  $E_{0J0}$  can be readily obtained—*e.g.*, via Monte Carlo methods. All rovibrational energies (and errors) are reported in eV, relative to the vibrational ground state energy of Paper I.

Overall, we find modEP to be the most accurate and reliable of the JS methods tested. By “accurate”, we mean that the errors are smallest on average; by “reliable”, we mean that this is generally true across all  $J$ ,  $K$ , and  $v$  values. In any case, modEP stands out as substantially different from the other *ab initio* JS methods, which all exhibit very similar trends (Fig. 5.1). Even EP behaves more like these other methods than like modEP—although it usually is closest to modEP, and the “second-best” performer. The third-best is invariably Simple—which means that none of the other geometry-based methods (*i.e.* geoEP, and the ring variants) actually improves performance. This somewhat disheartening conclusion will be discussed further a bit later on.

For  $J = 10$ , modEP achieves a remarkable RMS error of only 0.0008 eV (several wavenumbers), which is about one order of magnitude better than all other *ab initio* methods except EP. EP lies “halfway” between modEP and the others, with an RMS error of 0.0033 eV—comparable to Smith. The maximum  $J = 10$  error for most JS methods is around 0.03 eV; for modEP, it is only 0.002 eV [for ( $v = 2, K = 5$ )]. The relative degradation of accuracy with increasing  $v$  (Table 5.2) is comparable between modEP and Smith; both experience a roughly  $3\times$  error increase for  $v > 0$  vs.  $v = 0$ . This is surprising, considering that Smith uses a VSD scheme, but may relate to the

fact that his rotational constants are obtained from experiment. In any case, modEP is always much more accurate than Smith, even for the largest  $v$  values considered.

For  $J = 50$ , modEP is still the best performer—although only by about a factor of two, vs. the other *ab initio* methods. The modEP RMS error is substantially larger than for  $J = 10$  (by about  $7\times$ ). The behavior across methods is best illuminated by separating out the data by vibrational band (Table 5.2), so that  $v$  and  $K$  trends may be observed independently. Figure 5.3 conveys the same information as the  $J = 50$  plot of Fig. 5.1, but separated in this fashion. We first note that all JS methods exhibit a marked lack of degradation in performance with respect to increasing  $v$ . In contrast, the Smith VSD performance shows a very substantial degradation for  $v > 0$ , resulting in an overall RMS error around  $25\times$  larger than for  $J = 10$ , and more than  $10\times$  larger than for  $J = 50$  modEP.

Regarding the  $K$  trends, first note that in the Fig. 5.3 plots, the horizontal axis represents  $K$  value, rather than overall rovibrational excitation. As  $K$  increases for a given vibrational band, we see an overall increase in the JS errors. This is to be expected, given that Coriolis coupling also becomes more pronounced with increasing  $K$ . Remarkably however, modEP alone exhibits little to no such  $K$  degradation, and in some cases (*e.g.*,  $v = 0$ ), even *improves* with increasing  $K$ . Note that the errors exhibit monotonic spreading or fanning out across method as  $K$  increases—especially modEP, which approaches the other JS methods quite closely when  $K$  is small, but deviates significantly from them for large  $K$ . This accounts for the large “spikes” in Fig. 5.1 (where  $K$  is large and modEP disagrees with the other methods), as well as the smaller spikes (where  $K$  is small and all methods agree).

For  $J = 100$ , the *ab initio* JS methods exhibit a significant increase in RMS errors from  $J = 50$ , by about  $2\times$ . The modEP results are still the best, but are only marginally better than the others, with all methods behaving similarly. This can be attributed to  $K$  labeling becoming no longer valid. The most striking manifestation is a “kinking” behavior observed in the exact rovibrational spectrum, which becomes much more pronounced with increasing  $J$ . Simply put, rather than increasing smoothly and roughly quadratically with  $K$ , the exact energy levels clump together into nearly degenerate pairs (Chapter 4). This unexpected effect can only be

attributed to Coriolis coupling—although a simple physical explanation still eludes us.<sup>25;35</sup>

At any rate, no JS scheme [certainly none based on Eq. (5.3)] can be very effective when such spectral kinking is highly pronounced, and so this likely explains why all of the *ab initio* JS methods behave similarly. As for the Smith results, these degrade much more quickly with  $J$  (and  $v!$ ) than do the others, so that by  $J = 100$ , the Smith RMS error is 0.25 eV—about two orders of magnitude larger than for  $J = 10$ . Such degradation is perhaps not too surprising—although it does underscore the dangers of mixing experimental and theoretical data when attempting to analyze JS effectiveness.<sup>53;54</sup>

Although all of the *ab initio* methods besides modEP behave very similarly, there are some trends across methods that merit further discussion. First, geoEP predicts slightly lower energies than does Simple. Likewise, both ring variants yield appreciably lower energies than their non-ring counterparts, with error magnitudes that increase by 20–30 percent or so. This can be attributed to the effect that the geometry modifications have on the moments of inertia. Specifically, the ring structure necessitates a larger body-fixed  $z$ -axis moment of inertia than the corresponding asymmetric rotor. Likewise, the geoEP geometry is less prolate than the equilibrium geometry (due to centrifugal distortion), leading also to a larger  $z$ -axis moment of inertia. This results in smaller  $A$  values, and hence lower rotational energies. Because all JS methods tend to underestimate the correct energies, at least for HO<sub>2</sub>, this is the reason that the modified-geometry methods do less well than Simple.

A final consideration is that of the particular  $(v, K)$  labeling scheme used. In order to confirm the robustness of the general conclusions drawn here, an alternate labeling scheme was also explored. In the new scheme, a set of (presumed) accurate JS energy levels is compared with the exact rovibrational energies. By systematically analyzing all differences between JS and exact energy level pairs, one can assign suitable  $(v, K)$  labels to the exact energies by minimizing pair differences—i.e., errors. This procedure is further constrained by the assumptions that: (1) state labels have to be assigned in ascending order; (2) a  $K$  assignment associated with a given  $v$  cannot be made until the respective  $K$  of the previous vibrational band has been assigned. Thus,  $(v = 1, K = 3)$  is filled before  $(v = 2, K = 3)$ , for example. Of

course, the labeling so obtained can depend on the particular JS method used—in this case, modEP.

We found that for  $J = 10$ , the new state labels exactly matched those of the author’s previous HO<sub>2</sub> study, establishing a base of credibility for this approach. For  $J = 50$ , where  $(v, K)$  labels are thought to become questionable, the assignments differed only slightly from those assumed in the previous work; five of the 30 state labels were changed, and all of those in the top half of the spectrum. For  $J = 100$ , where the  $K$  distribution for individual rovibrational state wavefunctions becomes highly delocalized (Chapter 4), very different state labels were obtained using the new approach. Nevertheless, for all three  $J$  values, a separate analysis of the various JS methods using the new labels resulted in very similar accuracies, trends, and general conclusions.

For both labeling schemes, a fitting of vibrational bands to quadratic curves in  $K$  was also performed, in a further attempt to assess the validity of any JS and/or state-labeling scheme. As expected,  $J = 10$  fit beautifully to quadratic curves, with an average RMS error of .000558 eV for both (identical) labeling schemes. Surprisingly,  $J = 50$  also followed a quadratic pattern quite well for both schemes, with the Chapter 4 labels exhibiting a slightly smaller RMS error (0.00319 eV) than did the new scheme (0.00426 eV). For  $J = 100$ , neither state labeling scheme exhibited very meaningful quadratic behavior in  $K$ , and all had RMS errors at least 2–3× larger than for  $J = 50$  ( $\sim 0.01$  eV), which is greater than the rotational level spacing.

#### 5.4 Summary and Concluding Remarks

We have applied a variety of “*ab initio*” (pure theory-based) JS approximation methods to HO<sub>2</sub>, to predict exact rovibrational energy levels across a representative range of total angular momentum values,  $J = 10, 50, 100$ . Some of these theory-based methods [Simple, Simple (R)] use fixed rotational constants; the others use RSD values, obtained from the centrifugally distorted effective potential of Equation 5.4. Results are also compared with those of the empirical VSD JS scheme used by the Smith group.<sup>9</sup> In comparison with the present results, the accuracy of the Smith predictions degrades precipitously with increasing  $J$ , as might be expected. More

surprising is the degradation of the Smith results with increasing  $v$ , as compared with that of the present methods.

Of all JS methods considered, modEP stands out as the most accurate and reliable, across all  $J$ ,  $K$ , and  $v$  values considered. In comparison with the other *ab initio* JS methods, all of which are geometry-based, modEP performs extremely well for small  $J$ , but also for large  $K$ . Thus, modEP is surprisingly unsusceptible to degradation due to Coriolis coupling originating from  $K$ . All in all, modEP performs remarkably well—*i.e.*, to much higher accuracies at low  $J$ , and to reasonable accuracies at much higher  $J$  values—than might have been expected of any JS scheme. It is also surprisingly impervious to  $v$  excitation, even though it is not a VSD method.

The geometry-based JS methods all behave similarly across the board. Among these, EP generally performs best, followed by Simple. The modified-geometry methods all perform worse than Simple, because the modifications serve to lower the value of the rotational constant,  $A$ , and the corresponding rotational shift energies,  $E_{JK}^{\text{rot}}$ . These methods might present an improvement over Simple, for specific molecules where the rovibrational energies are over- rather than under-estimated via JS. Even in such cases, however, modEP is still expected to be the best approach.

**Table 5.2:** RMS errors in HO<sub>2</sub> rovibrational energy levels for various JS methods, for three different  $J$  values. For each  $J$ , RMS errors for the 30 lowest-lying states are presented—cumulative, as well as broken out by vibrational band. For  $v = \{0, 1, 2, 3\}$ , the number of states considered is  $\{11, 8, 7, 4\}$  respectively. The Smith results are set apart in a separate column; these are based on experimentally derived rotational constants (up to  $v = 2$ ), rather than the theory-based values used here. Errors are reported in eV.

$J$	$v$	Simple	Simple (R)	modEP	EP	geoEP	geoEP (R)	Smith
10	all	0.0058747	0.0077243	0.0008192	0.0032769	0.0072254	0.0093505	0.0027188
	0	0.0082052	0.0109287	0.0003339	0.0045838	0.0105368	0.0136291	0.0012139
	1	0.0044401	0.0057978	0.0009298	0.0022642	0.0049454	0.0065352	0.0032727
	2	0.0044035	0.0054118	0.0010996	0.0026330	0.0045973	0.0058018	0.0035915
	3	0.0005789	0.0007442	0.0009387	0.0006090	0.0005726	0.0007722	N/A
50	all	0.0080612	0.0094146	0.0060006	0.0075724	0.0092396	0.0108633	0.0625812
	0	0.0092641	0.0118694	0.0029028	0.0083199	0.0117502	0.0146334	0.0031493
	1	0.0047656	0.0053036	0.0056632	0.0046383	0.0050330	0.0058017	0.0790580
	2	0.0073108	0.0080141	0.0056460	0.0067861	0.0074724	0.0083138	0.0859537
	3	0.0106018	0.0104249	0.0112672	0.0107742	0.0105934	0.0103891	N/A
100	all	0.0155294	0.0162391	0.0146557	0.0197078	0.0178636	0.0188349	0.2464060
	0	0.0193557	0.0208478	0.0169698	0.0272732	0.0240378	0.0257897	0.0167903
	1	0.0117989	0.0120159	0.0119334	0.0135853	0.0125195	0.0130126	0.3005630
	2	0.0095283	0.0095563	0.0099244	0.0102668	0.0096685	0.0099145	0.3490401
	3	0.0184698	0.0182754	0.0190214	0.0177162	0.0180904	0.0179146	N/A

**Table 5.3:** JS method comparison for  $J = 10$  with exact HO<sub>2</sub> rovibrational energies. All states are relative to ground state energy, and are in units of eV.

$n$	$v$	$K$	Exact	Simple	Simple (R)	mPM	PM	Geo	Geo (R)	Smith
1	0	0	0.0148635	0	0	0	0	0	0	0
2	0	1	0.0170575	0.0000012	-0.0000557	0.0002116	0.0001187	0.0000120	-0.0000574	0.0001951
3	0	2	0.0244729	-0.0008289	-0.0010562	0.0000076	-0.0003724	-0.0007953	-0.0010723	-0.0000530
4	0	3	0.0364361	-0.0018165	-0.0023280	0.0000455	-0.0008134	-0.0017776	-0.0023977	-0.0000708
5	0	4	0.0531555	-0.0031700	-0.0040792	0.0000911	-0.0014509	-0.0031910	-0.0042854	-0.0000665
6	0	5	0.0745881	-0.0048465	-0.0062672	0.0001509	-0.0022851	-0.0050591	-0.0067534	0.0000028
7	0	6	0.1006871	-0.0067992	-0.0088449	0.0002263	-0.0033124	-0.0074157	-0.0098291	0.0001839
8	0	7	0.1313967	-0.0089722	-0.0117567	0.0003184	-0.0045664	-0.0103029	-0.0135468	0.0005325
9	1	0	0.1466357	0.0003310	0.0003310	0.0003310	0.0003310	0.0003310	0.0003310	0.0035394
10	1	1	0.1488015	0.0003603	0.0003035	0.0005708	0.0004779	0.0003712	0.0003017	0.0037276
11	1	2	0.1561274	-0.0003802	-0.0006075	0.0004563	0.0000763	-0.0003466	-0.0006236	0.0034635
12	0	8	0.1666532	-0.0113019	-0.0149387	0.0004286	-0.0060500	-0.0137658	-0.0179437	0.0011124
13	1	3	0.1679443	-0.0012215	-0.0017329	0.0006406	-0.0002183	-0.0011826	-0.0018026	0.0034161
14	2	0	0.1756787	-0.0000843	-0.0000843	-0.0000843	-0.0000843	-0.0000843	-0.0000843	0.0037263
15	2	1	0.1779468	-0.0001573	-0.0002141	0.0000531	-0.0000398	-0.0001464	-0.0002159	0.0038871
16	1	4	0.1844602	-0.0023716	-0.0032808	0.0008896	-0.0006525	-0.0023925	-0.0034869	0.0033777
17	2	2	0.1856730	-0.0012981	-0.0015254	-0.0004616	-0.0008416	-0.0012645	-0.0015415	0.0034478
18	2	3	0.1981079	-0.0027574	-0.0032688	-0.0008953	-0.0017542	-0.0027185	-0.0033385	0.0031576
19	1	5	0.2056333	-0.0037885	-0.0052092	0.0012089	-0.0012271	-0.0040011	-0.0056954	0.0033899
20	0	9	0.2063850	-0.0137166	-0.0183194	0.0005579	-0.0077630	-0.0178574	-0.0230644	0.0019952
21	2	4	0.2154813	-0.0047649	-0.0056741	-0.0015038	-0.0030458	-0.0047859	-0.0058803	0.0027868
22	1	6	0.2314170	-0.0054259	-0.0074716	0.0015995	-0.0019392	-0.0060425	-0.0084559	0.0034993
23	2	5	0.2377428	-0.0072703	-0.0086910	-0.0022729	-0.0047089	-0.0074829	-0.0091772	0.0023859
24	0	10	0.2505137	-0.0161380	-0.0218205	0.0007076	-0.0097103	-0.0226313	-0.0289541	0.0032593
25	2	6	0.2617501	-0.0071313	-0.0091770	-0.0001058	-0.0036445	-0.0077478	-0.0101612	0.0050970
26	1	7	0.2648437	-0.0103160	-0.0131004	-0.0010254	-0.0059101	-0.0116466	-0.0148906	0.0006736
27	3	0	0.2734799	0.0006493	0.0006493	0.0006493	0.0006493	0.0006493	0.0006493	
28	3	1	0.2756196	0.0007046	0.0006478	0.0009150	0.0008221	0.0007155	0.0006460	
29	3	2	0.2828577	0.0000531	-0.0001742	0.0008895	0.0005095	0.0000867	-0.0001903	
30	3	3	0.2945329	-0.0006478	-0.0011592	0.0012143	0.0003554	-0.0006088	-0.0012289	

**Table 5.4:** Errors in HO<sub>2</sub> rovibrational energy levels for various JS methods, for  $J = 50$ . Errors are obtained via comparison with the exact results of Chapter 4 (column IV), using  $(v, K)$  labels from Chapter 4 (columns I–III), and are presented in eV. The Smith results are set apart in a separate column (XI).

$n$	$v$	$K$	Exact	Simple	Simple (R)	modEP	EP	geoEP	geoEP (R)	Smith
1	0	0	0.3377239	0	0	0	0	0	0	0
2	0	1	0.3380129	0.001906	0.001849	0.002112	0.001965	0.001906	0.001840	0.002100
3	0	2	0.3535472	-0.007043	-0.007270	-0.006226	-0.006817	-0.007043	-0.007308	-0.006267
4	0	3	0.3629127	-0.005433	-0.005944	-0.003616	-0.004957	-0.005467	-0.006059	-0.003687
5	0	4	0.3793755	-0.006530	-0.007439	-0.003348	-0.005743	-0.006679	-0.007723	-0.003426
6	0	5	0.4003546	-0.007753	-0.009173	-0.002878	-0.006646	-0.008162	-0.009777	-0.002903
7	0	6	0.4260047	-0.009256	-0.011302	-0.002406	-0.007851	-0.010154	-0.012453	-0.002273
8	0	7	0.4562228	-0.010938	-0.013722	-0.001882	-0.009345	-0.012645	-0.015734	-0.001433
9	1	0	0.4621111	0.007716	0.007716	0.007716	0.007716	0.007716	0.007716	0.082437
10	1	1	0.4623934	0.009629	0.009572	0.009834	0.009688	0.009629	0.009563	0.084508
11	1	2	0.4777465	0.000861	0.000634	0.001677	0.001087	0.000861	0.000596	0.076217
12	0	8	0.4869664	-0.008755	-0.012391	0.002675	-0.007133	-0.011704	-0.015679	0.003660
13	1	3	0.4909338	-0.001351	-0.001862	0.000466	-0.000875	-0.001385	-0.001977	0.074799
14	2	0	0.4999147	-0.001460	-0.001460	-0.001460	-0.001460	-0.001460	-0.001460	0.086994
15	2	1	0.5001664	0.000484	0.000427	0.000689	0.000542	0.000484	0.000418	0.089171
16	1	4	0.5032023	0.001747	0.000838	0.004928	0.002534	0.001598	0.000554	0.079008
17	2	2	0.5170171	-0.009782	-0.010009	-0.008965	-0.009556	-0.009782	-0.010047	0.079607
18	2	3	0.5238741	-0.005663	-0.006175	-0.003846	-0.005188	-0.005698	-0.006289	0.084895
19	1	5	0.5264781	-0.001773	-0.003193	0.003101	-0.000667	-0.002182	-0.003797	0.076918
20	0	9	0.5300623	-0.014533	-0.019136	-0.000632	-0.013116	-0.019277	-0.024228	0.001178
21	2	4	0.5435514	-0.009975	-0.010884	-0.006793	-0.009188	-0.010124	-0.011168	0.082220
22	1	6	0.5491468	-0.000295	-0.002341	0.006555	0.001110	-0.001193	-0.003492	0.080142
23	2	5	0.5652690	-0.011936	-0.013357	-0.007062	-0.010830	-0.012345	-0.013960	0.082363
24	0	10	0.5735271	-0.016291	-0.021973	0.000105	-0.015410	-0.023512	-0.029518	0.003106
25	2	6	0.5789125	-0.001433	-0.003479	0.005417	-0.000028	-0.002331	-0.004630	0.095438
26	1	7	0.5819257	-0.004538	-0.007322	0.004518	-0.002945	-0.006244	-0.009333	0.077964
27	3	0	0.5822055	0.014784	0.014784	0.014784	0.014784	0.014784	0.014784	
28	3	1	0.5918391	0.007346	0.007289	0.007551	0.007404	0.007346	0.007284	
29	3	2	0.5973373	0.008433	0.008205	0.009249	0.008659	0.008432	0.008168	
30	3	3	0.6064520	0.010294	0.009782	0.012111	0.010769	0.010259	0.009668	

**Table 5.5:** Errors in HO<sub>2</sub> rovibrational energy levels for various JS methods, for  $J = 100$ . Errors are obtained via comparison with the exact results of Chapter 4 (column IV), using  $(v, K)$  labels from Chapter 4 (columns I–III), and are presented in eV. The Smith results are set apart in a separate column (XI).

$n$	$v$	$K$	Exact	Simple	Simple (R)	modEP	EP	geoEP	geoEP (R)	Smith
1	0	0	1.2862321	0	0	0	0	0	0	0
2	0	1	1.2862365	0.0021907	0.0021339	0.0023511	0.0019629	0.0020857	0.0020327	0.0023847
3	0	2	1.3262269	-0.0312143	-0.0314416	-0.0305776	-0.0321002	-0.0316484	-0.0318598	-0.0304384
4	0	3	1.3280212	-0.0220330	-0.0225444	-0.0206189	-0.0240605	-0.0230571	-0.0235298	-0.0202872
5	0	4	1.3495601	-0.0282060	-0.0291152	-0.0257380	-0.0318270	-0.0301115	-0.0309445	-0.0251025
6	0	5	1.3661755	-0.0250653	-0.0264859	-0.0213005	-0.0308131	-0.0282121	-0.0294990	-0.0202159
7	0	6	1.3872855	-0.0220290	-0.0240747	-0.0167672	-0.0304528	-0.0268560	-0.0286841	-0.0150459
8	0	7	1.3872942	0.0064989	0.0037145	0.0134072	-0.0052026	-0.0005275	-0.0029772	0.0160036
9	1	0	1.3900444	0.0282910	0.0282910	0.0282910	0.0282910	0.0282910	0.0282910	0.3242890
10	1	1	1.4183070	0.0022235	0.0021666	0.0023839	0.0019957	0.0021185	0.0020654	0.2983810
11	1	2	1.4267433	0.0003726	0.0001453	0.0010093	-0.0005133	-0.0000615	-0.0002729	0.2970060
12	0	8	1.4285334	-0.0018134	-0.0054502	0.0068324	-0.0174589	-0.0116614	-0.0148047	0.0106009
13	1	3	1.4496297	-0.0115382	-0.0120497	-0.0101241	-0.0135658	-0.0125623	-0.0130350	0.2858890
14	2	0	1.4510834	-0.0041204	-0.0041204	-0.0041204	-0.0041204	-0.0041204	-0.0041204	0.3462420
15	2	1	1.4512666	-0.0021085	-0.0021653	-0.0019480	-0.0023362	-0.0022134	-0.0022665	0.3484880
16	1	4	1.4513134	0.0021439	0.0012347	0.0046119	-0.0014772	0.0002383	-0.0005946	0.3006830
17	2	2	1.4661834	-0.0104399	-0.0106672	-0.0098032	-0.0113258	-0.0108740	-0.0110854	0.3408580
18	2	3	1.4859224	-0.0192032	-0.0197147	-0.0177891	-0.0212308	-0.0202273	-0.0207000	0.3332630
19	1	5	1.4859354	-0.0127220	-0.0141426	-0.0089572	-0.0184698	-0.0158688	-0.0171557	0.2872460
20	0	9	1.4877945	-0.0237575	-0.0283603	-0.0133485	-0.0440720	-0.0371867	-0.0410880	-0.0080457
21	2	4	1.4899775	-0.0078925	-0.0088017	-0.0054245	-0.0115135	-0.0097980	-0.0106309	0.3462110
22	1	6	1.4946360	0.0027237	0.0006780	0.0079855	-0.0057001	-0.0021033	-0.0039315	0.3044390
23	2	5	1.4961654	0.0056756	0.0042550	0.0094404	-0.0000722	0.0025288	0.0012420	0.3618830
24	0	10	1.5174676	-0.0117233	-0.0174057	0.0004026	-0.0374819	-0.0295869	-0.0343014	0.0076741
25	2	6	1.5195195	0.0064679	0.0044222	0.0117297	-0.0019560	0.0016408	-0.0001873	0.3652480
26	1	7	1.5247792	0.0011171	-0.0016673	0.0080254	-0.0105844	-0.0059093	-0.0083590	0.3048970
27	3	0	1.5266016	0.0188962	0.0188962	0.0188962	0.0188962	0.0188962	0.0188962	-1.5893800
28	3	1	1.5292687	0.0184242	0.0183674	0.0185846	0.0181964	0.0183192	0.0182662	-1.5920500
29	3	2	1.5356406	0.0186376	0.0184103	0.0192744	0.0177518	0.0182036	0.0179921	-1.5984200
30	3	3	1.5473471	0.0179068	0.0173954	0.0193209	0.0158793	0.0168827	0.0164100	-1.6101200

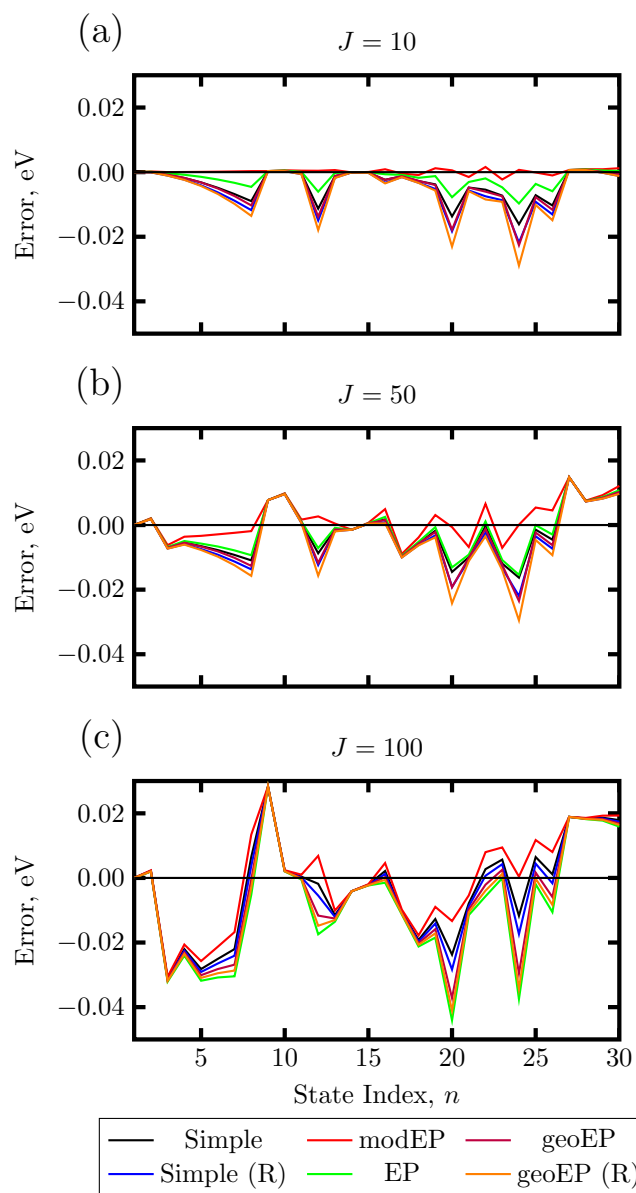


**Figure 5.1:** Errors in HO<sub>2</sub> rovibrational energy levels for various JS methods, as a function of excitation index  $n$ , for three different  $J$  values. Errors are obtained via comparison with the exact results of Papers I and Chapter 4, using  $(v, K)$  labels from Chapter 4, and presented in eV. The Smith results are not plotted, as these lie well outside the range indicated, for  $J = 50$  and  $J = 100$ . A comparison with Smith can be found in Figure 4.2 (with opposite sign convention) for  $J = 50$ .

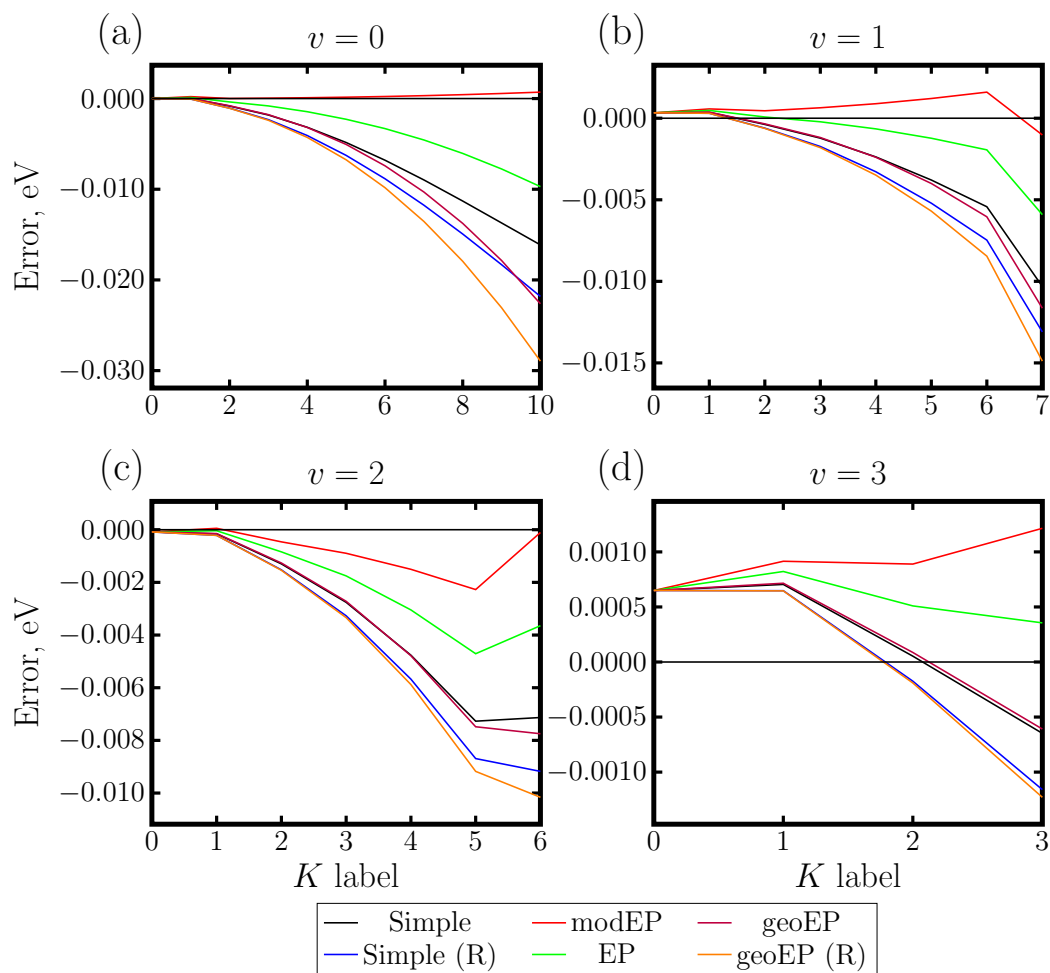


**Figure 5.2:** Errors in  $\text{HO}_2$  rovibrational energy levels for various JS methods, as a function of vibrational ( $v$ ) and rotational ( $K$ ) excitation, for  $J = 10$ . Errors are obtained via comparison with the exact results of Chapter 4, using  $(v, K)$  labels from Chapter 4, and presented in eV.

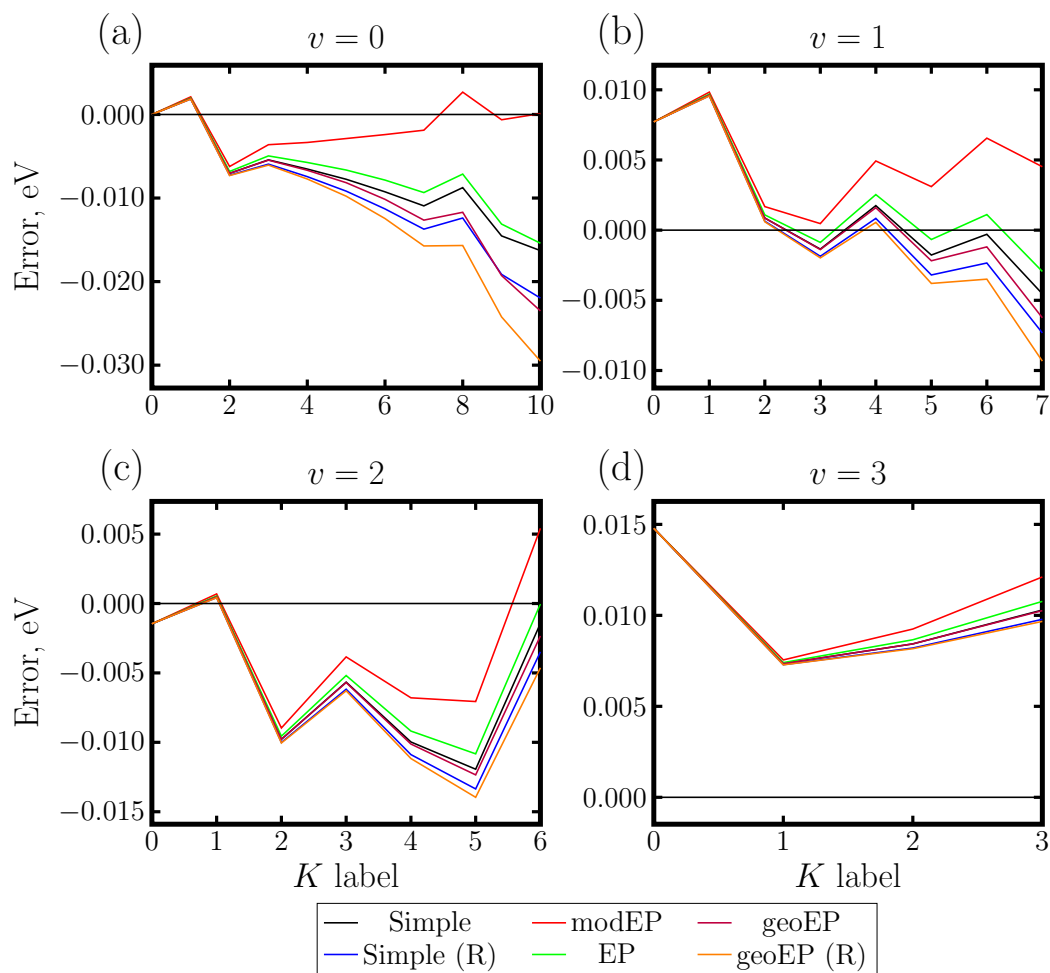


**Figure 5.3:** Errors in HO<sub>2</sub> rovibrational energy levels for various JS methods, as a function of vibrational ( $v$ ) and rotational ( $K$ ) excitation, for  $J = 50$ . Errors are obtained via comparison with the exact results of Chapter 4, using  $(v, K)$  labels from Chapter 4, and presented in eV.

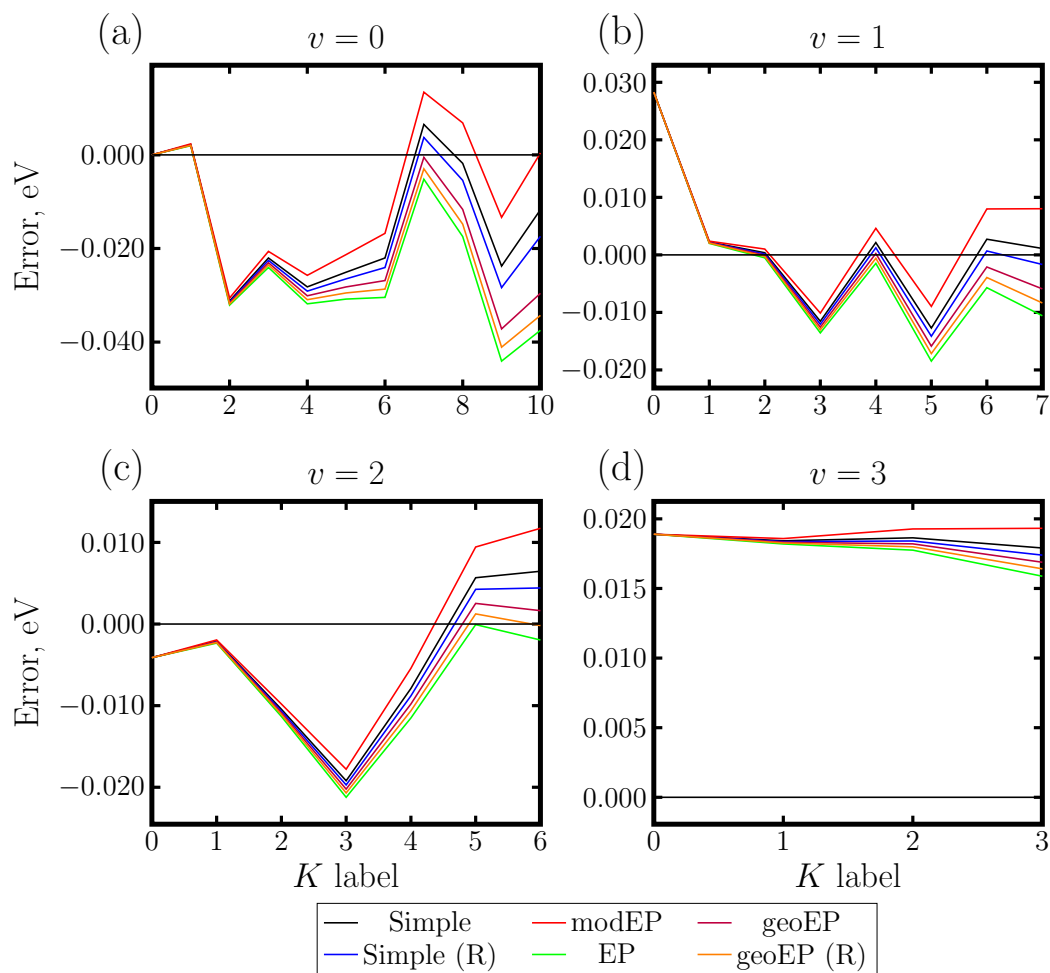


**Figure 5.4:** Errors in HO<sub>2</sub> rovibrational energy levels for various JS methods, as a function of vibrational ( $v$ ) and rotational ( $K$ ) excitation, for  $J = 100$ . Errors are obtained via comparison with the exact results of Chapter 4, using  $(v, K)$  labels from Chapter 4, and presented in eV.

## CHAPTER 6

### VIBRATIONAL STATES OF THE NEON TETRAMER

#### 6.1 Introduction

The field of weakly bound cluster spectroscopy and dynamics touches on diverse areas of chemistry and physics, from fundamental aspects of intermolecular forces to new insights on phase transitions and solvation. Despite its broad applicability and a flurry of research interest throughout the past decades, it is still considered by some an immature field.<sup>103</sup> This is partially due to basic questions about the fundamental nature of clusters going unanswered, such as how to identify the physical phase of clusters and the very nature of their respective transitions. New information on a quantum state level would provide valuable information regarding the dynamics of these phase changes.

Rare gas clusters serve as a poster child for studying weakly bound systems, for their only interaction stems from the Van der Waals interaction, yielding characteristic low binding energies and long range interactions. Furthermore, they can be described fairly accurately via pair-wise Lennard-Jones (L-J) potentials, obviating the difficulties of multidimensional PES development. These reasons allow rare gas clusters to serve as a prototype for more complex phenomena such as solvation with relative ease.

Interestingly, neon clusters have attracted less research than their neighboring counterparts helium and argon, despite their living in a dynamical regime that is “part quantum and part classical.” Investigations involving the equilibrium structure and thermodynamics up to  $\text{Ne}_{38}$  have been performed, but accurate quantum dynamical characterization of bound rovibrational states have gone by the wayside, save for the *ScalIT* study of  $\text{Ne}_3$  mentioned in Section 1.1. Naturally, the  $\text{Ne}_4$  vibrational spectrum is the next logical step in calculations. These states, especially in the isomerization bands, shed light into the dynamics and structure of neon as atoms coalesce into clusters.

Despite the ease in PES development for neon clusters, the quantum dynamical behavior of rare gas clusters provides an extreme computational challenge. In the case of  $\text{Ne}_4$ , the long-range interactions, semi-heavy masses, and low binding energies

creates a very high DOS which exist in a very small energetic window. These types of systems, which are easy to create yet difficult to solve, function perfectly as benchmark applications for *ScalIT*. In fact, we purposely only use the default options of *ScalIT* when performing calculations, not using all of the fine-tuned “bells and whistles” that the QD community uses to optimize calculations, except those that are easy for a non-expert to use. This is all done in effort to show that the high-level modules designed for the *non*-expert user are sufficient for even difficult tetra-atomic applications.

## 6.2 Theory and Background

### 6.2.1 Rovibrational Calculations for Tetra-atomic $A_4$ Molecules

Chapter 2 discussed the general theoretical framework for triatomics. The underlying ideas and concepts of tetra-atomics are identical, but the added DOFs introduce complexity worth noting here. Similar to the high-level triatomic modules in *ScalIT*, the tetra-atomic modules employ Jacobi coordinates. For a tetra-atomic molecule, there are a myriad of Jacobi vector arrangements one can choose, corresponding to two main categories: the 3+1 (triatom-atom) arrangement, or the 2+2 (diatom-diatom) arrangement. For  $Ne_4$ , we have chosen the 2+2 arrangement of Jacobi vectors, which is illustrated in Figure 6.1.

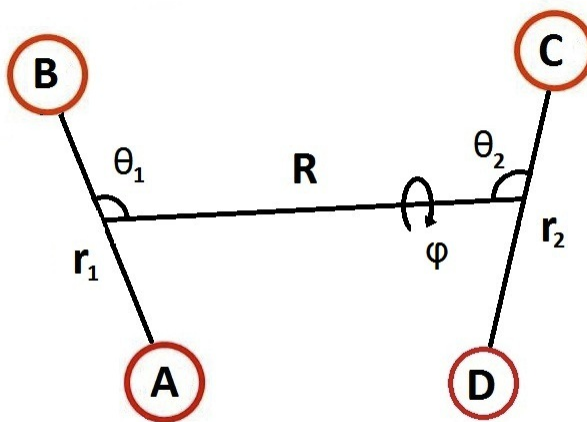


**Figure 6.1:** Diagram of a tetra-atomic molecule described by the diatom-diatom arrangement of Jacobi vectors.

Although we discuss the full rovibrational theory here for the sake of completeness, it should be noted that this dissertation only covers the *vibrational* spectrum, which corresponds to the special case of  $J = 0$ , yielding a slightly simplified vibrational Hamiltonian (rovibrational calculations will be forthcoming, in future work). Within the Born-Oppenheimer approximation, the full dimensional rovibrational Hamiltonian for a tetra-atomic molecule ABCD in body-fixed reference frame and Jacobi coordinates is expressed as:

$$\begin{aligned} \hat{H} = & -\frac{1}{2\mu_R} \frac{\partial^2}{\partial^2 R} - \frac{1}{2\mu_{r_1}} \frac{\partial^2}{\partial^2 r_1} - \frac{1}{2\mu_{r_2}} \frac{\partial^2}{\partial^2 r_2} + \frac{\vec{L}^2}{2\mu_R R^2} + \frac{\vec{j}_1^2}{2\mu_{r_1} r_1^2} + \frac{\vec{j}_2^2}{2\mu_{r_2} r_2^2} \\ & + V(R, r_1, r_2, \theta_1, \theta_2, \phi) \end{aligned} \quad (6.1)$$

with  $\vec{L} = \vec{J} - \vec{j}_{12} = \vec{J} - (\vec{j}_1 + \vec{j}_2)$

where  $\vec{r}_1$  is the vector between atoms A and B,  $\vec{r}_2$  is the vector between atoms C and D,  $\vec{R}$  is the vector between the center of mass of AB and the center of mass of CD,  $\theta_1$  is the angle between vectors  $\vec{r}_1$  and  $\vec{R}$ ,  $\theta_2$  is the angle between  $\vec{r}_2$  and  $\vec{R}$ ,  $\phi$  is the azimuthal angle (torsional or dihedral),  $\vec{J}$  is the total angular momentum operator,  $\vec{j}_1$  is the angular momentum operator associated with vector  $\vec{r}_1$ ,  $\vec{j}_2$  is the angular momentum operator associated with  $\vec{r}_2$ , and  $\mu_R, \mu_{r_1}, \mu_{r_2}$  are the reduced masses:

$$\begin{aligned} \mu_{r_1} = \mu_{AB} &= \frac{m_A m_B}{m_A + m_B} \quad ; \quad \mu_{r_2} = \mu_{CD} = \frac{m_C m_D}{m_C + m_D} \\ \mu_R = \mu_{AB,CD} &= \frac{m_{AB} m_{CD}}{m_{AB} + m_{CD}} = \frac{(m_A + m_B)(m_C + m_D)}{m_A + m_B + m_C + m_D} \end{aligned} \quad (6.2)$$

Following the same lines as Chapter 2, we expand our wavefunctions in a basis with respect to the same three good quantum numbers ( $J, M, \epsilon$ ) as follows:

$$\begin{aligned} \Psi^{JM\epsilon}(R, r_1, r_2, \theta_1, \theta_2, \phi; \alpha, \beta, \gamma) = & \sum_{v_1, v_2, v_3, i, J, M, \epsilon} C_{v_1, v_2, v_3, i}^{J, M, \epsilon} \cdot u_{v_1}(R) \cdot \phi_{v_2}(r_1) \cdot \psi_{v_3}(r_2) \\ & \cdot \Phi_i^{JM\epsilon}(\theta_1, \theta_2, \phi, \alpha, \beta, \gamma) \end{aligned} \quad (6.3)$$

with the parity-adapted angular functions given as:

$$\begin{aligned} \Phi_i^{JM\epsilon}(\theta_1, \theta_2, \phi, \alpha, \beta, \gamma) = & \frac{1}{\sqrt{2(1 + \delta_{K0})}} [D_{KM}^J(\alpha, \beta, \gamma) |j_1 j_2 j_{12} K\rangle \\ & + \epsilon (-1)^{j_1 + j_2 + j_{12} + J} \cdot D_{-KM}^J(\alpha, \beta, \gamma) |j_1 j_2 j_{12} - K\rangle] \end{aligned} \quad (6.4)$$

with

$$\begin{aligned} |j_1 j_2 j_{12} K\rangle = Y_{j_1 j_2}^{j_{12} K}(\theta_1, \theta_2, \phi) = \sum_m C(j_1, j_2, j_{12}, m(K - m)K) \\ \cdot \Theta_{j_1}^m(\theta_1) \cdot \Theta_{j_2}^{K-m}(\theta_2) \cdot \frac{e^{im\phi}}{\sqrt{2\pi}} \end{aligned} \quad (6.5)$$

where all symbols are the higher dimensional counterparts of Equations 2.3 and 2.4. For example,  $C(j_1, j_2, j_{12}, m(K - m)K)$  of Equation 6.5 represent the  $6j$ -symbol coefficients, which are a higher-dimension generalization of Clebsch-Gordon coefficients. The index  $i$  is a composite index used for brevity, and runs over associated ranges of  $(j_1, j_2, j_{12}, K)$ . The  $C$  coefficient of Equation 6.3 is an arbitrary coefficient.

### 6.2.2 Symmetry

As with any scientific numerical application, we attempt to exploit inherent symmetry of the molecule in our basis functions as best we can to reduce the size and difficulty of the problem. With  $\text{Ne}_4$ , a tetrahedron with four identical atoms, there is great potential to do just that. The full molecular symmetry group, including parity, of  $\text{Ne}_4$  is  $G_{48} = \{E, E^*\} \otimes S_4$ , where  $E^*$  is the parity operator, and  $S_4$  is the permutation group of four identical atoms. Often times, one chooses or is relegated to using coordinates that do not respect the full symmetry of the molecule, and such is the case with our application of *ScalIT* to  $\text{Ne}_4$ .

Our choice of Jacobi coordinates results in the following set of permutation operations (plus parity), that can be explicitly treated by the coordinate system:  $\{E, (AB), (CD), (AB)(CD), E^*, (AB)^*, (CD)^*, (AB)(CD)^*\}$ . These constitute the  $G_8 = \{E, E^*\} \otimes G_4$  symmetry group. The  $G_4$  character table can be viewed in Table 6.1. To incorporate inversion parity symmetry, we simply append a “+” or “−” superscript to the  $G_4$  irreducible representation (irrep). Clearly our choice of coordinates do not take advantage of the full symmetry, for we do not respect all of the  $4!$ -fold

	E	(AB)	(CD)	(AB)(CD)	
$A_{gg}$	1	1	1	1	$j_1, j_2$ even
$A_{gu}$	1	1	-1	-1	$j_1$ even, $j_2$ odd
$A_{ug}$	1	-1	1	-1	$j_1$ odd, $j_2$ even
$A_{uu}$	1	-1	-1	-1	$j_1, j_2$ odd

**Table 6.1:**  $G_4$  group character table. Also included is the associated characters of  $j_1$  and  $j_2$ .

permutation of atoms. In fact, *ScalIT* treats both diatoms completely separately, ignoring whether or not they are identical. Put another way: we are working explicitly with the permutation-inversion symmetry group of an  $A_2B_2$  molecule, rather than that of an  $A_4$  molecule. Due to this, computed states from multiple computed  $G_8$  irreps correlate to the same (degenerate)  $G_{48}$  states, as per the correlation table of Table 6.2.

Physically speaking, one can associate the  $A_{gg}$  and  $A_{uu}$  irreps as a simultaneous flipping of both  $\vec{r}_1$  and  $\vec{r}_2$ , while  $A_{gu}$  and  $A_{ug}$  irreps correspond to flipping only  $\vec{r}_1$  or  $\vec{r}_2$ . Due to nuclear spin symmetry restrictions, only states with A character of the  $S_4$

$S_4$	$G_4$
A	$A_{gg}$
B	$A_{uu}$
E	$A_{gg} + A_{uu}$
F	$A_{gg} + A_{gu} + A_{ug}$
G	$A_{uu} + A_{gu} + A_{ug}$

**Table 6.2:**  $S_4$  to  $G_4$  correlation table for identical particle tetra-atomics.

symmetry group will be physically real, which corresponds to the  $A_{gg}$  character of the  $G_4$  calculations we perform. These are the totally symmetric irreps of their respective groups. By computing the eigenenergies for each of the remaining (non- $A_{gg}$ ) irreps of  $G_4$ , and looking for degeneracies with the  $A_{gg}$  states, we can discern which of the  $A_{gg}$  states actually belongs to the totally symmetric A irrep of  $S_4$ —i.e., those states from our  $A_{gg}$  calculation that are physically real. Only the states that survive this procedure in the  $A_{gg}$  character will be labeled physically real. This is done for both

parities so as to capture the entire spectrum of  $G_{48}$ . We present all computed states from all  $G_8$  irreps, even the unphysical ones, as they could serve useful for analysis of rotational constants, or for comparison with other numerical studies. Note that because we have four identical atoms,  $A_{gu}$  and  $A_{ug}$  irreps are identical, corresponding to a flip of either  $\vec{r}_1$  or  $\vec{r}_2$ . Consequently, we do not explicitly report the  $A_{ug}$  states here, although calculations were performed as a sanity check.

### 6.3 Computational Details and Potential Energy Surface

As mentioned per Section 6.2.1, one of the key motivations for performing bound state rovibrational spectra calculations on neon clusters is the speed at which one can obtain a fairly accurate PES. The potential employed in *ScalIT* is simply the sum of pairwise L-J potentials, given as:

$$V = \sum_{i < j} V_{ij}, \quad i, j = \{A, B, C, D\}, \quad V_{ij} = 4\epsilon \left[ \left( \frac{\sigma}{r_{ij}} \right)^{12} - \left( \frac{\sigma}{r_{ij}} \right)^6 \right] \quad (6.6)$$

where  $\epsilon$  is the energy scale indicating the two-atom L-J potential well depth (classical  $\text{Ne}_2$  binding energy), and  $\sigma$  is the length scale parameter, related closely to the equilibrium bond length. Typically, the Hamiltonian of equation 6.1 is rewritten in terms of the scaled length  $r'_{ij} = r_{ij}/\sigma$  and mass  $m' = m\epsilon\sigma^2/\hbar^2$  in order to yield dimensionless energies in units of  $\epsilon$ . We use the Jacobi parameters of Ref [11], which is summarized in Table 6.3 for reference, along with basis sizes and coordinate ranges for each DOF.

As is the case with any choice of pair-wise potential, three-body terms are neglected in the resultant surface, thus limiting our overall potential accuracy and our ability to compare to experimental results. The work presented here is mainly motivated as the next stepping stone from the previous  $\text{Ne}_3$  work performed using *ScalIT*. Nevertheless, we make a rough estimation of the three-body contribution not taken into account. Ref [11] approximates  $1 \text{ cm}^{-1}$  or less for the neon trimer, a slightly smaller contribution than Karlicky *et. al.* calculates for the argon trimer of  $3 \text{ cm}^{-1}$ .<sup>104</sup> This was attributed to the decreased well depths of neon compared to argon. Karlicky also observed an increasingly smaller contribution with vibrational excitation.

L-J	Coordinate range	Basis size
$\epsilon = 24.743267 \text{ cm}^{-1}$	$0.9\sigma \leq r_1 \leq 3.5\sigma$	$n_{r_1} = 9$
$\sigma = 5.195 \text{ a.u.}$	$0.9\sigma \leq r_2 \leq 3.5\sigma$	$n_{r_2} = 9$
$m = 19.99244 \text{ amu}$	$0.0\sigma \leq R \leq 3.5\sigma$	$n_R = 15$
		$n_{j_1} = 30$
		$n_{j_1} = 30$
		$n_{j_{12}} = 60$
		$n_{i,Agg+} = 2736$

**Table 6.3:** Lennard-Jones and basis set parameters for  $\text{Ne}_4$  calculations

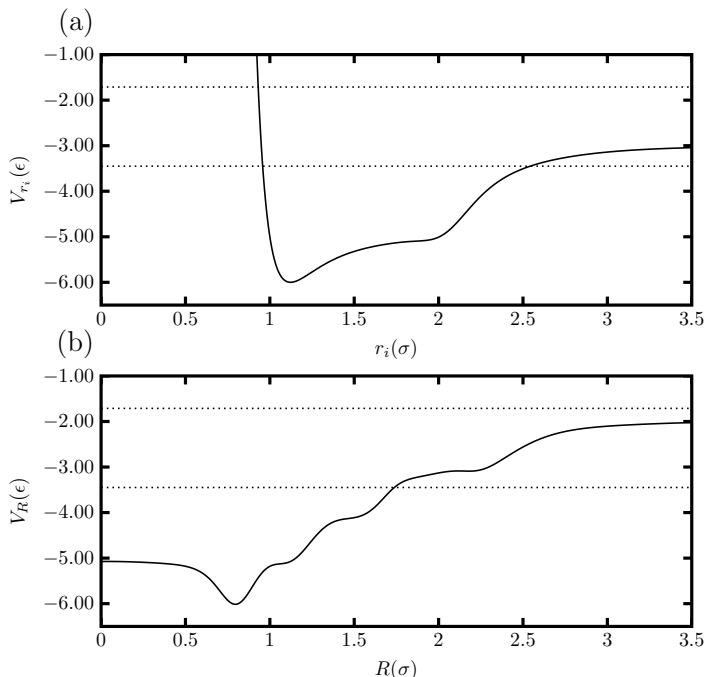
If we use classical well depth comparisons as an indicator of three body term contributions,  $\text{Ne}_4$ 's depth of  $6\epsilon$  doubles that of  $\text{Ne}_3$ , thereby increasing possible three-body interactions. Furthermore, the additional atom of  $\text{Ne}_4$  allows for  $\binom{4}{3} = 4$  possible extra terms to the single term of  $\text{Ne}_3$ , further increasing the interaction contribution. These observations lead us to a rough maximum of 5–10  $\text{cm}^{-1}$  of error attributed to three-body interaction terms.

The effective potentials for  $r_i$  and  $R$  are shown in Figure 6.2. For reference, both the ground state ( $\text{Ne}_4$ ) and first-dissociation ( $\text{Ne}_3+\text{Ne}$ ) energy are projected on top of each effective potential. Outside of their use in creating PSODVR basis functions, 1D effective potential plots shed a significant amount of dynamical information on molecular systems. The equilibrium bond distance for any L-J dimer potential is  $r_m = \sqrt[6]{2}\sigma$ , yielding a minimum potential energy of  $-\epsilon$ . A tetramer of pair-wise potentials leads to a tetrahedral equilibrium structure resulting in 6 bonds and a minimum classical energy of  $-6\epsilon$ .

The limits of stretching either of the  $r$  coordinates tends towards the trimer-atom dissociation pathway, which requires breaking a total of 3 bonds. On the other hand, isomerization only requires a single bond to be broken to become accessible, allowing the molecule to move more freely into its isomer via a hinging about its remaining two bonds into a planar geometry, evident in the scalloping of the potential as it approaches  $r_i = 2$ .

This planar geometry is also associated with the minimum at  $R = 0$ . As  $R$  is decreased from the equilibrium tetrahedron, both  $r_i$  distances stretch causing an in-

**Figure 6.2:** Effective 1D radial potentials for  $\text{Ne}_4$  (or any L-J tetramer) in Jacobi coordinates created in the manner discussed in Section 3.1. (a)  $V_{r_i}(r_i)$ ; (b)  $V_R(R)$ . We use the dimensionless L-J coordinates  $\sigma$  and  $\epsilon$  for length and energy, respectively. The two horizontal lines represent the ground state (bottom) and first-dissociation (top) energies for  $\text{Ne}_4$ .



crease in energy. Therefore, our calculations must include small  $R$  values if we wish to capture isomerization dynamics. Stretching the  $R$  coordinate tends towards the same planar structure through  $\phi$  tending towards zero. Further stretching quickly causes another bond break resulting in a trimer plus atom arrangement at  $\sim 1.5\sigma$ . The slow scalloping from  $1.5\sigma$  to  $\sim 2.25\sigma$  followed by the flattening and minuscule well is characterized by a competition between a complete flattening out into a linear geometry and the 3+1 dissociation pathway of  $V_{r_i}$ . Finally, the two dimers separate. Between the required large amplitude coordinate ranges and nontrivial potential surface dynamics, a standard DVR grid would be hard pressed to accurately describe such a configuration space without implementing a very large number of basis functions to completely describe the space. On the other hand, these are exactly the conditions

for which a PSODVR basis is beneficial, for the basis functions are placed in areas of curvature first, automatically situating themselves in areas of interest.

## 6.4 Results and Discussion

**ScalIT** was used to calculate the lowest  $\sim 22$  bound vibrational states associated with each of the unique  $\text{Ne}_4 G_8$  irreps as described in Section 6.2.2. Multiple separate calculations were performed for each parity and  $G_8$  irrep (excluding the redundant  $A_{ug}$ ), resulting in six separate calculations. For all calculations presented here, the zero of energy corresponds to the  $\text{Ne} + \text{Ne} + \text{Ne} + \text{Ne}$  dissociation limit. The calculated states can be viewed in Table 6.4 along with tentative state labels. The varied factors contributing to a very high DOS and large basis size have limited our ability to perform convergence tests to our desired standards. We systematically increase the basis size of individual coordinates, holding all others the same, to test convergence. This allows us to ascertain an overall level of basis set convergence. Through these tests, we have concluded that the lower 10 states of each irrep are converged to within  $10^{-4}\epsilon$ , with the lowest states to within  $10^{-6}\epsilon$ . As energy increases, our confidence of convergence decreases due to the difficulty in successfully completing jobs in this energy range. Along with basis set error, computational error associated with the iterative nature of **ScalIT** can manifest itself, especially in energetic areas where a high spectral resolution is necessary. The drastic increase in DOS as energy increases has challenged our ability to complete a single run within the allotted job runtime. Nevertheless, these calculations represent the first converged vibrational spectra for  $\text{Ne}_4$  yet computed.

We observe very few states (2–3) that are a significant distance apart from others, *i.e.* more than  $0.05\epsilon$ . Furthermore, the level separation after the third state is on the order of  $0.02\epsilon$  or less. This is indicative of only two states being localized in an individual vibrational well, and all higher-lying states delocalized across multiple wells simultaneously, *i.e.* “fluxional” states. This level of delocalization was to be expected as indicated from the neon trimer results. However for the tetramer, this distinct dividing line can be associated with a clear representation of a liquid–solid phase change from the cluster science point of view. This is further reiterated if we consider our discussion of dynamics discussion related to the effective potentials of

Figure 6.2. The localized states lie in a regime we associated with a competition of geometries, with an energy corresponding to approximately three and half bonds. The subsequent jump to about  $-3\epsilon$  and delocalization for the remaining states indicates a bond breakage, and energetic freedom to “roam” about the competing geometries.

### 6.5 Summary and Concluding Remarks

We have taken the next step in our quest to calculate highly accurate bound rovibrational spectra by successfully calculating the low lying vibrational spectrum of  $\text{Ne}_4$ . We have calculated  $\sim 20$  states for all  $G_8$  symmetry irreps, and attempted to label the physically real states utilizing the full molecular symmetry group  $G_{48}$  correlated to our chosen coordinate symmetry group  $G_8$ . At the low end of the spectrum, a convergence of  $10^{-4}\epsilon$  was achieved, with some states converged to even  $10^{-6}\epsilon$ . The higher energy windows exhibited a drastic increase in difficulty to converge adequately, most likely due to the fast increasing DOS. Future work will be spent on accurately converging the vibrational spectrum to a much higher accuracy, and subsequently fleshing out the low  $J$  rovibrational states.

**Table 6.4:** Lowest lying  $\text{Ne}_4$  vibrational states for each of the computed symmetry irreps.  $S_4$  symmetry labels are assigned via the scheme discussed in Section 6.2.2. The states are in bond energy units,  $\epsilon$ , and relative to the  $\text{Ne} + \text{Ne} + \text{Ne} + \text{Ne}$  atomic dissociation threshold. States without labels are at a high enough energy such that sufficient comparison with other irreps is impossible to make a conclusion. The labels colored red are considered questionable.

	Agg				Auu		Agu	
	Even		Odd		Even	Odd	Even	Odd
1	-3.44907	E	-3.089828	E	-3.08990	-3.449050	-2.98542	-2.98410
2	-3.09063	E	-2.882732	A	-2.92329	-3.090618	-2.91042	-2.85801
3	-2.98429	F	-2.741809	A	-2.81786	-2.982908	-2.78957	-2.71223
4	-2.96505	A	-2.644873	A	-2.67403	-2.959711	-2.62193	-2.59006
5	-2.92339	E	-2.590557	A	-2.61339	-2.885835	-2.59033	-2.55043
6	-2.90849	A	-2.575919	A	-2.59049	-2.858152	-2.54824	-2.50999
7	-2.89470	A	-2.502505	A	-2.58392	-2.825640	-2.53352	-2.48308
8	-2.82366	E/A	-2.478723	E	-2.52641	-2.744464	-2.51782	-2.47936
9	-2.79442	A	-2.463597	A	-2.51943	-2.712803	-2.51216	-2.45683
10	-2.74602	E/A	-2.45436	A/E/F	-2.47130	-2.685961	-2.48106	-2.43236
11	-2.67262	A	-2.43346	A	-2.45594	-2.640159	-2.45709	-2.42212
12	-2.65950	A	-2.41137	F	-2.44956	-2.619400	-2.42219	-2.38409
13	-2.61681	E	-2.38446	F	-2.42945	-2.577499	-2.41024	-2.36517
14	-2.61448	A	-2.38205	A/F	-2.41678	-2.549110	-2.41006	-2.34616
15	-2.58805	A	-2.34514	F	-2.40725	-2.528715	-2.39526	-2.32930
16	-2.57767	E	-2.34085	E	-2.40695	-2.508016	-2.38715	-2.31831
17	-2.54536	A/E/F	-2.32026	—	-2.39729	-2.500541	-2.37949	-2.31279
18	-2.52883	E	-2.31394	—	-2.36369	-2.491602	-2.36925	-2.29374
19	-2.51636	A	-2.29827	—	-2.36215		-2.34509	-2.28362
20	-2.51365	A			-2.35417		-2.33613	-2.27018
21	-2.50893	A/E/F			-2.33770		-2.32639	-2.25695
22	-2.47666	—			-2.32988		-2.32214	-2.25129
23								-2.24376

CHAPTER 7  
CONCLUDING REMARKS

During the course of these studies, *ScalIT* has been used to both broaden the scope of understanding in the systems studied, as well as verify the applicability of *ScalIT* to difficult problems in a straightforward manner. The calculation of HO<sub>2</sub> rovibrational states up to the dissociation threshold proved that even notoriously elusive triatomic molecular systems are well within the purview of even the *non*-expert quantum dynamicist. This work helped to push the avenue of bringing exact QD calculations to the masses, per se. Teaching others to use software suites like *ScalIT* cultivates a culture of collaboration, opening the door to new types of research to be explored, which is, in essence the heart of science.

Riding on the back of the comprehensive HO<sub>2</sub> calculations, the JS methodology introduced as a simple method include Coriolis contributions in widely used approximation techniques, has shown promising potential. It proved robust in the subsequent deep analysis and comparison with other approximation methods, and showed a surprising level of stability throughout all ranges of excitation. Such a simple yet effective tool could prove useful for anyone concerned with molecular dynamics.

On a different front, *ScalIT*'s application to the neon tetramer is an effort to push the limits of exact QD calculations. Clearly, calculation of the low  $J$  rovibrational states of Ne<sub>4</sub> would be the immediate focus of future research. Today's technology pushes towards sharing a computational burden across larger and larger facilities in an intelligent and efficient manner. In order to do this, creatively designed software efficiently applied to said facilities is necessary, especially in the realm of high intercommunication that exact QD lives in. Successful calculation of the Ne<sub>4</sub> rovibrational spectrum will prove a triumph in not only the scientific realm of weakly bound cluster science, but also in the scientific computing community. For the task at hand, this can almost currently be performed using *ScalIT* as a non-expert, given the computational resources at our disposal. However, these calculations would certainly be well within reach, if we were to implement certain "expert user" customizations.

Currently, for a problem size around the neon tetramer application, *ScalIT* runs most efficiently on roughly 240 CPUs on the facilities mentioned in Chapter 3,

with hundreds of gigabytes of shared/distributed memory being used. Some modules parallelize much more efficiently, and scale to well beyond thousands of cores, but are held back by the poor scaling of others. Optimizing the weak links should be a priority in order to further increase the system size to the neon pentamer, a project in which we have started to plan for. Recently, the Poirier group has received access to Mira and Argonne National Lab's computing facility, one of the fastest and most sophisticated machines to date, consisting of over 750,000 cores. In order to take advantage of such a resource, the execution of current projects must maintain a high standard of efficiency and accuracy that past projects have shown.

After all, it *is* harder than rocket science.

BIBLIOGRAPHY

- [1] Chen, W.; Poirier, B. *J. Comput. Phys.* **2006**, *219*, 185–197.
- [2] Chen, W.; Poirier, B. *J. Comput. Phys.* **2006**, *219*, 198–209.
- [3] Chen, W.; Poirier, B. *J. Parallel Distrib. Comput.* **2010**, *70*, 779–782.
- [4] Chen, W.; Poirier, B. *J. Theor. Comput. Chem.* **2010**, *9*, 825–846.
- [5] Poirier, B.; Carrington, T. *J. Chem. Phys.* **2001**, *114*, 9254–9264.
- [6] Zhang, H.; Smith, S. C. *J. Chem. Phys.* **2003**, *118*, 10042–10050.
- [7] Zhang, H.; Smith, S. C. *J. Chem. Phys.* **2004**, *120*, 9583–9593.
- [8] Zhang, H.; Smith, S. C. *J. Chem. Phys.* **2005**, *123*, 014308.
- [9] Zhang, H.; Smith, S. C. *J. Phys. Chem. A* **2006**, *110*, 3246–3253.
- [10] Petty, C.; Poirier, B. *Chem. Phys. Lett* **2014**, *605–606*, 16–21.
- [11] Yang, B.; Chen, W.; Poirier, B. *J. Chem. Phys.* **2011**, *135*, 094306.
- [12] Baccarelli, I.; Gianturco, F. A. *J. of Chem. Phys.* **2006**, *122*, 084313.1–084313.13.
- [13] Zhang, J. Z. H. *Theory and application of quantum molecular dynamics*; World Scientific: Singapore ; River Edge, N.J., 1999.
- [14] Varshalovich, D. A.; Moskalev, A.; Khersonskii, V. *Quantum theory of angular momentum*; World Scientific, 1988.
- [15] Wu, X. T.; Hayes, E. F. *J. Chem. Phys.* **1997**, *107*, 2705–2719.
- [16] Meijer, A. J. H. M.; Goldfield, E. M. *J. Chem. Phys.* **1998**, *108*, 5404–5413.
- [17] Meijer, A. J. H. M.; Goldfield, E. M. *J. Chem. Phys.* **1999**, *110*, 870–880.
- [18] Goldfield, E. M.; Meijer, A. J. H. M. *J. Chem. Phys.* **2000**, *113*, 11055–11062.
- [19] Goldfield, E. M.; Gray, S. K. *Comp. Phys. Commun.* **1996**, *98*, 1–14.
- [20] Mussa, H. Y.; Tennyson, J. *J. Comput. Phys. Commun.* **2000**, *128*, 434–445.
- [21] Wang, X.-G.; Carrington, Jr., T. *Comp. Phys. Commun.* **2009**, *181*, 455–461.

- [22] Lanczos, C. *J. Res. Natl. Bur. Stand.* **1950**, *45*, 255–282.
- [23] Freund, R. W.; Nachtigal, N. M. *Numer. Math.* **1991**, *60*, 315–339.
- [24] Mandelshtam, V. A.; Grozdanov, T. P.; Taylor, H. S. *J. Chem. Phys.* **1995**, *103*, 10074–10084.
- [25] Chen, W.; Poirier, B. *J. Theor. Comput. Chem.* **2010**, *9*, 435–469.
- [26] Yang, B.; Poirier, B. *J. Phys. B* **2012**, *45*, 135102.
- [27] Yang, B.; Poirier, B. *J. Theor. Comput. Chem.* **2012**, *12*, 1250107.
- [28] Light, J.; Carrington, T. *Adv. in Chem. Phys.* **2004**, *114*, 263–310.
- [29] R. Littlejohn, m. *J. Chem. Phys.* **2002**, *116*, 8691–8703.
- [30] Poirier, B. *Numer. Linear Algebra Appl.* **2000**, *7*, 715–726.
- [31] Press, W. H.; *et al*, *Numerical Recipes*, 2nd ed.; Cambridge University Press: Cambridge, England, 1992.
- [32] Golub, G.; Loan, C. V. *Matrix Computations*, 3rd ed.; The John Hopkins University Press, 1996.
- [33] Poirier, B. *Phys. Rev. A* **1997**, *56*, 120–130.
- [34] Wyatt, R. E. *Phys. Rev. E* **1995**, *51*, 3643–3658.
- [35] Petty, C.; Chen, W.; Poirier, B. *J. Phys. Chem. A* **2013**, *32*, 7280–7297.
- [36] Du, H.; Hessler, J. P. *J. Chem. Phys.* **1992**, *96*, 1077–1092.
- [37] Yang, H.; Gardiner, W. C.; Shin, K. S.; Fujii, N. *Chem. Phys. Lett.* **1994**, *231*, 449–453.
- [38] Honma, K. *J. Chem. Phys.* **1995**, *102*, 7856–7863.
- [39] Fink, E. H.; Ramsay, D. A. *J. Mol. Spectrosc.* **1997**, *185*, 304–324.
- [40] Fink, E. H.; Ramsay, D. A. *J. Mol. Spectrosc.* **2002**, *216*, 322–334.
- [41] Anglada, J. M.; Olivella, S.; Sole, S. *J. Phys. Chem. A* **2006**, *110*, 6073–6082.
- [42] Thiebaud, J.; Crunaire, S.; Fittschen, C. *J. Phys. Chem. A* **2007**, *111*, 6859–6966.

- [43] Melius, C. F.; Blint, R. J. *Chem. Phys. Lett.* **1979**, *64*, 183–189.
- [44] Pastrana, M. R.; Quintales, L. A. M.; Brandao, J.; Varandas, A. J. C. *J. Phys. Chem.* **1990**, *94*, 8073–8080.
- [45] Leforestier, C.; Miller, W. H. *J. Chem. Phys.* **1994**, *100*, 733–735.
- [46] Zhang, D. H.; Zhang, J. Z. H. *J. Chem. Phys.* **1994**, *101*, 3671–3678.
- [47] Dai, J.; Zhang, J. Z. H. *J. Chem. Phys.* **1996**, *104*, 3664–3671.
- [48] Qi, J.; Bowman, J. M. *J. Chem. Phys.* **1996**, *105*, 9884–9889.
- [49] Kendrick, B.; Pack, R. T. *Chem. Phys. Lett.* **1995**, *235*, 291–296.
- [50] Kendrick, B.; Pack, R. T. *J. Chem. Phys.* **1995**, *102*, 1994–2012.
- [51] Kendrick, B.; Pack, R. T. *J. Chem. Phys.* **1996**, *104*, 7502–7514.
- [52] Kendrick, B.; Pack, R. T. *J. Chem. Phys.* **1997**, *106*, 3519–3539.
- [53] Quéméner, G.; Balakrishnan, N.; Kendrick, B. K. *J. Chem. Phys.* **2008**, *129*, 224309.
- [54] Quéméner, G.; Kendrick, B. K.; Balakrishnan, N. *J. Chem. Phys.* **2010**, *132*, 014302.
- [55] Pack, R. T.; Butcher, E. A.; Parker, G. A. *J. Chem. Phys.* **1995**, *102*, 5998–6012.
- [56] Barclay, V. J.; Dateo, C. E.; Hamilton, I. P.; Kendrick, B.; Pack, R. T. *J. Chem. Phys.* **1995**, *103*, 3864–3867.
- [57] Barclay, V. J.; Hamilton, I. P. *J. Chem. Phys.* **1995**, *103*, 2834–2838.
- [58] Mandelshtam, V. A.; Taylor, H. S.; Miller, W. H. *J. Chem. Phys.* **1996**, *105*, 496–503.
- [59] Dobbyn, A. J.; Stumpf, M.; Keller, H.-M.; Schinke, R. *J. Chem. Phys.* **1995**, *103*, 9947–9962.
- [60] Dobbyn, A. J.; Stumpf, M.; Keller, H.-M.; Hase, W. L.; Schinke, R. *J. Chem. Phys.* **1995**, *102*, 5867–5870.
- [61] Dobbyn, A. J.; Stumpf, M.; Keller, H.-M.; Schinke, R. *J. Chem. Phys.* **1996**, *104*, 8357–8381.

- [62] Mahapatra, S. *J. Chem. Phys.* **1996**, *105*, 344–345.
- [63] Zhang, H.; Smith, S. C. *J. Chem. Phys.* **2001**, *115*, 5751–5758.
- [64] Zhang, H.; Smith, S. C. *J. Theor. Comput. Chem.* **2010**, *9*, 653–665.
- [65] Xu, C.; Xie, D.; Zhang, D. H.; Lin, S. Y.; Guo, H. *J. Chem. Phys.* **2005**, *122*, 244305.
- [66] Xu, C.; Xie, D.; Honvault, P.; Lin, S. Y.; Guo, H. *J. Chem. Phys.* **2007**, *127*, 024304.
- [67] Xu, C.; Jiang, B.; Xie, D.; Farantos, S. C.; Lin, S. Y.; Guo, H. *J. Phys. Chem A* **2007**, *111*, 10353–10361.
- [68] Xie, D.; Xu, C.; Ho, T.-K.; Rabitz, H. A.; Lendvay, G.; Lin, S. Y.; Guo, H. *J. Chem. Phys.* **2007**, *126*, 074315.
- [69] Lin, S. Y.; Guo, H.; Honvault, P.; Xu, C.; Xie, D. *J. Chem. Phys.* **2008**, *128*, 014303.
- [70] Lin, S. Y.; Sun, Z.; Guo, H.; Zhang, D. H.; Honvault, P.; Xie, D.; Lee, S.-Y. *J. Phys. Chem. A* **2008**, *112*, 602–611.
- [71] Lique, F.; Jorfi, M.; Honvault, P.; Halvick, P.; Lin, S. Y.; Guo, H.; Xie, D. Q.; Dagdigian, P. J.; Klos, J.; Alexander, M. H. *J. Chem. Phys.* **2009**, *131*, 221104.
- [72] Ma, J.; Lin, S. Y.; Guo, H.; Sun, Z.; Zhang, D. H.; Xie, D. *J. Chem. Phys.* **2010**, *133*, 054302.
- [73] Sun, Z.; Zhang, D. H.; Xu, C. X.; Zhou, S. L.; Xie, D. Q.; Lendvay, G.; Lee, S.-Y.; Lin, Y.; Guo, H. *J. Am. Chem. Soc.* **2008**, *130*, 14962–14963.
- [74] Sun, Z.; Lin, X.; Lee, S.-Y.; Zhang, D. H. *J. Phys. Chem A* **2009**, *113*, 4145–4154.
- [75] Troe, J.; Ushakov, V. G. *J. Phys. Chem. A* **2009**, *113*, 3940–3945.
- [76] Barnes, G. L.; Kellman, M. E. *J. Chem. Phys.* **2010**, *133*, 101105.
- [77] Miller, J. A.; Kee, R. J.; Westbrook, C. K. *Annu. Rev. Phys. Chem.* **1990**, *41*, 345–387.
- [78] Sun, Q.; Bowman, J. M.; Schatz, G. C.; Sharp, J. R.; Connor, J. N. L. *J. Chem. Phys.* **1990**, *92*, 1677–1686.

- [79] Bowman, J. M. *J. Phys. Chem.* **1991**, *95*, 4960–4968.
- [80] Bowman, J. M.; Wang, D. *J. Chem. Phys.* **1993**, *98*, 6235.
- [81] Bowman, J. M. *Chem. Phys. Lett.* **1994**, *217*, 36–40.
- [82] Poirier, B. *J. Chem. Phys.* **1998**, *108*, 5216–5224.
- [83] Poirier, B. *Chem. Phys.* **2005**, *308*, 305–315.
- [84] Pack, R. *J. Chem. Phys.* **1974**, *60*, 633–639.
- [85] McGuire, P.; Kouri, D. J. *J. Chem. Phys.* **1974**, *60*, 2488–2499.
- [86] Poirier, B.; Light, J. C. *J. Chem. Phys.* **1999**, *111*, 4869–4885.
- [87] Poirier, B.; Light, J. C. *J. Chem. Phys.* **2001**, *114*, 6562–6571.
- [88] Poirier, B. *Found. Phys.* **2001**, *31*, 1581–1610.
- [89] Bian, W.; Poirier, B. *J. Theo. Comput. Chem.* **2003**, *2*, 583–597.
- [90] Burkholder, J. B.; Hammer, P. D.; Howard, C. J.; Towle, J. P.; Brown, J. M. *J. Mol. Spectrosc.* **1992**, *151*, 493–512.
- [91] Xiao, Y. S.; Poirier, B. *J. Chem. Phys.* **2005**, *122*, 124318.
- [92] Colbert, D. T.; Miller, W. H. *J. Chem. Phys.* **1992**, *96*, 1982–1990.
- [93] Huang, S.-W.; Carrington, Jr., T. *J. Chem. Phys.* **2000**, *112*, 8765–8771.
- [94] Poirier, B.; Carrington, Jr., T. *J. Chem. Phys.* **2001**, *114*, 9254–9264.
- [95] Poirier, B.; Carrington, Jr., T. *J. Chem. Phys.* **2002**, *116*, 1215–1227.
- [96] Bowman, J. *J. Phys. Chem.* **1991**, *95*, 4960–4968.
- [97] Huang, S.; Carrington, Jr., T. *J. Chem. Phys.* **2000**, *112*, 8765–8771.
- [98] Pack, R. *J. Chem. Phys.* **1974**, *60*, 663–639.
- [99] McGuire, P.; Kouri, D. *J. Chem. Phys.* **1974**, *60*, 2488–2499.
- [100] Skinner, D.; Germann, T.; Miller, W. *J. Phys. Chem. A* **1998**, *102*, 3828–3834.
- [101] Burkholder, J.; Hammer, P.; Howard, C.; Towle, J.; Brown, J. *J. Molec. Spec.* **1992**, *151*, 493–512.

- [102] Poirier, B. *J. Chem. Phys.* **1998**, *108*, 5216–5224.
- [103] Bačić, Z.; Miller, R. E. *J. Phys. Chem.* **1996**, *100*, 12945–12959.
- [104] Karlický, F.; Lepetit, B.; Kalus, R.; Gadéa, F. X. *J. Chem. Phys.* **2007**, *126*, 174305.
- [105] Petty, C.; Poirier, B. *Applied Mathematics* **2013**, Accepted.
- [106] Poirier, B.; Miller, W. H. *Chem. Phys. Lett.* **1997**, *265*, 77–83.
- [107] Poirier, B. *Phys. Rev. A* **1997**, *56*, 120–130.
- [108] Lung, C.; Leforestier, C. *J. Chem. Phys.* **1989**, *90*, 3198–3203.
- [109] J. A. Bentley, J.-P. Brunet, R. E. Wyatt, R. A. Friesner, and C. Leforestier, *Chem. Phys. Lett.* **1989**, *161*, 393.
- [110] Bramley, M. J.; Carrington, Jr., T. *J. Chem. Phys.* **1993**, *99*, 8519.
- [111] Bramley, M. J.; Carrington, Jr., T. *J. Chem. Phys.* **1994**, *101*, 8494.
- [112] Wang, X.; Jr., T. C. *J. Chem. Phys.* **2001**, *114*, 1473–1477.
- [113] Portable, Extensible Toolkit for Scientific Computation. <http://www.mcs.anl.gov/petsc>, Accessed: 2014-02-30.
- [114] Geus, R.; Röllin, S. *Parallel Computing* **2001**, *27*, 883–896.

# Appendices

APPENDIX A  
STANDALONE GUIDE TO USING *SCALIT*<sup>1</sup>

## A.1 Introduction

*ScalIT*, in principle, can be applied across a broad range of scientific disciplines; however, recent development and application has been geared toward molecular chemical dynamics, performing exact time-independent quantum dynamics calculations. More specifically, it has been applied to computing bound rovibrational energy levels and wavefunctions. The software suite has been designed at the lowest level to scale across a large number of CPUs, and be as general as possible, allowing the scientific community to “tap” into *ScalIT* for use with their own algorithms. In this chapter we focus on the operation of *ScalIT* from the *non-expert* user’s perspective, after a brief description of the underlying numerical methods. If a more detailed analysis is desired, the reader is referred to the literature<sup>1–4;11;25–27;30;34;82;86–89;93–95;106;107</sup>. High level modules have been created for performing calculations on systems up to four atoms; for simplicity, we restrict ourselves to discussing only triatomic molecules, although the procedure described is nearly identical for more difficult systems.

A.2 The “A Matrix” Form, and *ScalIT* Methodology

We present a broad overview of *ScalIT*’s core functionality here. The emphasis is to provide the reader with an understanding of where in the science landscape *ScalIT* lives, as well as how its iterative nature has fueled its success. In order to understand the process of using *ScalIT*, one must have a basic grasp of its problem scope, as well as the fundamental “nuts and bolts” of the machinery used.

We are solving the time independent Schrödinger equation (TISE) formulated for rovibrational dynamics of molecular systems, which is a symmetric eigenvalue/eigenvector problem. It is solved in a variational way, in which the rovibrational Hamiltonian is represented as a matrix,  $\mathbf{H}$ , in a “basis” of grid points (we use a DVR) distributed over position space. For a molecule of  $n$  atoms, there are  $3n - 5$  rovibrational DOF that must explicitly be considered, which *ScalIT* describes using Jacobi coordinates. Therefore, triatomics have 4 DOFs  $(r, R, \theta, K)$ ,  $r$  being the distance between two

---

<sup>1</sup>This chapter has been reprinted and adapted for this dissertation from Ref. [105]

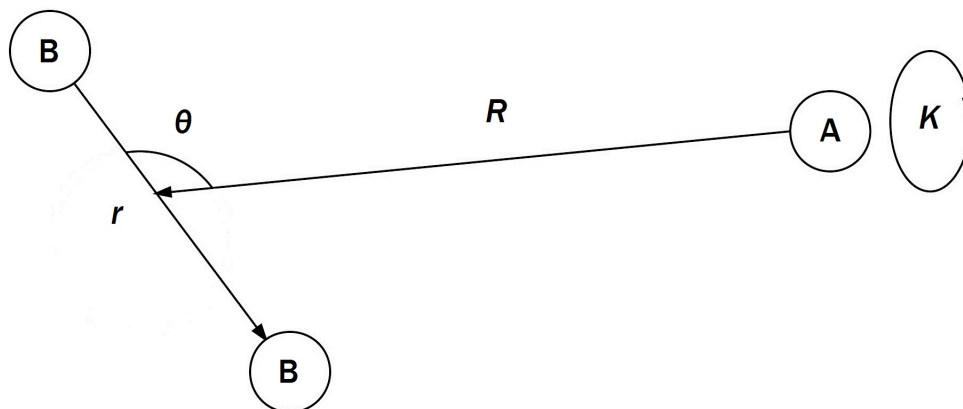


**Figure A.1:** Model of an  $AB_2$  molecule as described by Jacobi coordinates.

atoms, typically taken to be the heavier two.  $R$  is the distance between the center of mass of  $r$  and the third atom, and  $\theta$  the angle between  $r$  and  $R$ .  $K$  is a DOF associated with rotation. Fig. A.1 shows a model of an  $AB_2$  triatomic molecule, meaning two of the atoms are of the same type.

A new Hamiltonian matrix is created and solved for each combination of the symmetry parameters  $J$  and  $\epsilon$ , where  $J$  is the total angular momentum, and  $\epsilon$  is inversion parity. With the coordinate system established, the triatomic Hamiltonian can be expressed as:

$$\mathbf{H} = \mathbf{T}_r + \mathbf{T}_R + \mathbf{T}_{\theta K} + \mathbf{V} \quad (\text{A.1})$$

where  $\mathbf{V}$  is the potential energy matrix, and  $\mathbf{T}_i$  is the  $i^{\text{th}}$  kinetic energy matrix associated with the  $i^{\text{th}}$  DOF.  $\mathbf{V}$  is a diagonal matrix, and each  $\mathbf{T}_i$  is diagonal with respect to all DOFs excluding that of its own subscript(s). This discretized grid-based representation of the molecular Hamiltonian yields a resultant matrix with a highly structured block-form, characterized by diagonal blocks of precisely the same size, and off-diagonal blocks which are themselves diagonal. We term this the “**A** matrix form.” The **A** matrix is sparse, meaning that a large number of the matrix elements are zero. As the number of DOFs increases, a fractal, self-similar pattern is produced which increases sparsity, while maintaining the same structure at all scales. A pictorial representation can be seen in figure A.2.

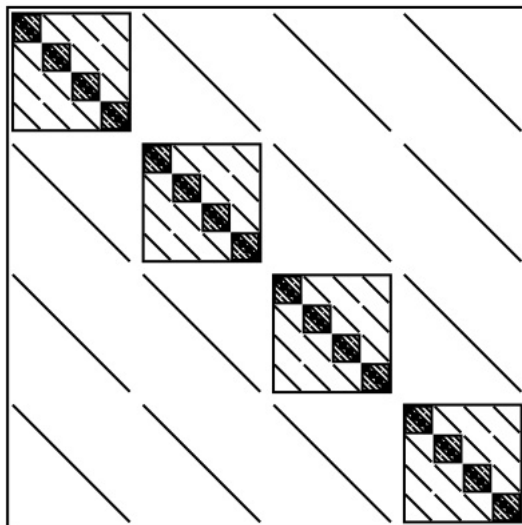


**Figure A.2:** A matrix form with greater than two degrees of freedom. This form is characterized by being block diagonal, with off diagonal blocks being diagonal themselves. Note the self similar pattern of the diagonal blocks.

Sparsity of the  $\mathbf{H}$  matrix is an important numerical consideration, give that the matrix dimensionality,  $N$ , scales exponentially with the number of DOFs. Consequently, direct diagonalization routines such as Householder's algorithm, for which memory requirements scale as  $N^2$ , and computational effort as  $N^3$ , can become intractable, even for triatomics. Sparse iterative approaches have shown to be a viable means for solving linear algebra problems with such large matrices<sup>34;89;93;108-112</sup>, for matrix-vector products scale with the number of nonzero elements, thus reducing computational effort with increasing sparsity. Furthermore, storage of the entire  $\mathbf{H}$  is not necessary, significantly reducing storage requirements. The sparsity and highly structured form of  $\mathbf{A}$  matrices would suggest the use of sparse iterative techniques, yet research has shown the  $\mathbf{A}$  matrix to be a worst case scenario in many respects, that elicits poor performance from all standard iterative methods<sup>31;113;114</sup>. To this end, the algorithms developed in *ScalIT* address the shortcomings, and have proven to be effective and highly parallelizable.

*ScalIT* overcomes the above difficulties in part through the PIST algorithm<sup>93-95</sup>. This approach calculates a window of states around a chosen energy by applying the

Lanczos algorithm to  $F(\mathbf{H}) = (E\mathbf{I} - \mathbf{H})^{-1}$ , where  $\mathbf{I}$  is the identity, rather than to  $\mathbf{H}$  itself. This shift-and-invert strategy extremizes the states close to energy  $E$ , reducing the required number of iterations for convergence, especially in regimes exhibiting a high DOS. The novel aspect of this approach is in not computing the matrix-vector product of  $F(\mathbf{H})$  exactly, but approximately, and subsequently diagonalizing  $\mathbf{H}$  in the basis of the inexact Lanczos vectors iteratively until a given number of states are converged to desired accuracy. Each approximate Lanczos iteration  $\mathbf{x} = (E\mathbf{I} - \mathbf{H})^{-1}\mathbf{b}$  is computed by solving a system of linear equations  $(E\mathbf{I} - \mathbf{H})\mathbf{x} = \mathbf{b}$  using the QMR method to some predefined relative error. After each matrix-vector product, the resultant Lanczos vectors are explicitly reorthogonalized using the Gram-Schmidt procedure, to ensure against spurious eigenvalues. The total number of required matrix-vector products is  $ML$ , where  $M$  is the number of approximate Lanczos iterations, and  $L$  is the number of QMR iterations per Lanczos. Typically,  $M$  is low due to the spectral transform applied, although  $L$  can be large in regions of high spectral density. Although  $ML$  is typically lower than alternative methods, the main advantage is the ability to use preconditioning to substantially reduce  $L$ , and subsequent total computational effort.

It is well known that when solving a system of linear equations  $\mathbf{Ax}=\mathbf{b}$  iterative, using a preconditioner  $\mathbf{P}$  such that  $\mathbf{P}^{-1}\mathbf{A} \approx \mathbf{1}$  can greatly reduced  $L$ . A good preconditioner must therefor be “close” to  $\mathbf{A}$ , as well as easy to invert. It has been shown that for chemical applications, using an adiabatic approximation to the Hamiltonian yields much better results than generic matrix preconditioners<sup>4;30</sup>. *ScalIT* does this via a recursive application of the OSB procedure<sup>1-4;30;82;106;107</sup>. Simply put, OSB is characterized by applying a series of block Jacobi rotations to the Hamiltonian to minimize off diagonal elements, and eliminating the residual off diagonal components. What is left is a zeroth order approximation to the exact Hamiltonian,  $\mathbf{H}_{\text{OSB}}$ , which is diagonal its simplest implementation, thus trivial to invert. To increase preconditioner effectiveness, a “Wyatt” variant of the OSB procedure can be used (OSBW)<sup>4;94</sup>. This corresponds to calculating off-diagonal elements of  $\mathbf{H}_{\text{OSB}}$  in the vicinity of  $E$ , known as a “Wyatt block,” to combat near singularities that occur when eigenvalues are close to  $E$ . Computational burden is increased due to the calculation of these

off-diagonal elements, yet studies have shown that this is greatly overcome by the reduction in  $L$ , especially in high-DOS regimes.

### A.3 Using *ScalIT*

In the context of bound rovibrational spectroscopy calculations for triatomic molecules, a typical *ScalIT* calculation will proceed in three (or four) separate stages:

1. Compute 1D phase space optimized (PSO) effective potentials (defined shortly) and basis sets for radial coordinates,  $r$  and  $R$ .
2. Construct 4D (Coriolis-coupled) rovibrational Hamiltonian matrix for given  $J$  and  $\epsilon$ .
3. Solve the Hamiltonian matrix eigenproblem to compute rovibrational energy levels and (optionally) wavefunctions.
4. (optional) Create plotting data for specified rovibrational wavefunctions.

Each stage has a different high-level *ScalIT* module (or set of modules) associated with it, as well as its own short input file (typically 6–10 lines each).

Stage 1 above is problem- (i.e. PES-) specific. For each of a very large number of uniformly-spaced points for a given radial coordinate (e.g.  $r$ ), the PES is *globally* minimized with respect to all other coordinates, to determine the value of the radial PSO effective potential at that point [e.g.  $V_r(r)$ ].<sup>86–88</sup> Although using *local* minima can, under some circumstances, provide a more efficient PSODVR (and is computationally far less expensive), the global minimum is always reliable, and is therefore safest for use as the default choice for *ScalIT*.<sup>89</sup> In any case, thousands of sampling points are used to avoid spline-ringing problems,<sup>87</sup> and also to ensure that the subsequent PSO variational basis representation (VBR) calculation (an intermediate step towards generating the PSODVR) is *extremely* well converged (i.e., to several digits of precision beyond that of the final calculation, so as to rule out Stage 1 as a significant source of numerical error). Because the number of sampling points (technically sinc-DVR grid points<sup>92</sup>) is so large, the minimization stage of the calculation is somewhat slow (e.g. requires several hours on a single core), but need

only be performed a single time for any given PES. (Parallelization would be trivial, but is not yet implemented in the current version of *ScalIT*.) Once the radial PSO effective potentials are determined, they are used to compute the 1D radial PSO VBR functions via diagonalization of the corresponding 1D effective radial sinc-DVR Hamiltonian matrices; the data is then stored as intermediate output for the later stages. This part of the calculation also only needs to be performed a single time, provided the number of radial PSODVR functions computed (specified by the user in the input file) is larger than or equal to the largest radial PSODVR basis size used in the later Stages 2 and 3. Other user-specified inputs include the masses, the PES, and the radial sinc-DVR coordinate ranges and grid spacings.

Stage 2 employs one of three standard *ScalIT* modules—depending on whether the triatomic molecule of interest is of the AB<sub>2</sub> form (i.e. two identical nuclei) or not, and if so, whether the even- or odd-permutation symmetry block is desired. In the input file, the user specifies  $J$ ,  $\epsilon$ , the PSODVR basis size for both radial coordinates,  $r$  and  $R$ , and the maximum  $j$  value to use in the basis expansion,  $j_{\max}$ .  $j$  is the body-fixed analog of  $J$ . Radial PSO DVRs of the specified sizes are constructed using the PSO VBR data previously computed in Stage 1. The bend-angle basis functions are automatically combined with the appropriate body-fixed rotational states, with optional application of energy truncation to the combined bend-rotation states ( $K$  truncation could also be applied). The various components of the full-dimensional, but sparse, rovibrational Hamiltonian matrix are then stored in separate data files (one for the radial PSODVR grid point and matrix data, the other for the angular contributions). Stage 2 must be repeated for each separate convergence calculation—i.e., for each distinct set of basis parameters used. However, it is quite fast for triatomic systems, typically requiring only seconds to minutes of CPU time.

Stage 3, the “meat” of the *ScalIT* package, employs but a single standard module—designed to accommodate calculations of arbitrary symmetry and dimensionality (i.e., tetraatomic and pentaatomic calculations use this same module). The coordinates may also be combined into “layers,” if desired. The first phase of Stage 3 is the OSB preconditioner construction phase for which the default choice is to treat the radial coordinates as separate inner coordinate layers, and the combined bend-rotation states as a single outermost layer. For standard OSB precondition-

ing, no user parameters are required, although more sophisticated preconditioning schemes do require this (e.g., specification of the Wyatt window center and width, for OSBW preconditioning). In the second phase of stage 3, the PIST method is used to compute a predetermined number of rovibrational eigenstate energies (and wavefunctions if desired) in the vicinity of a specified central energy,  $E$ , to within a predetermined (iterative) error (generally chosen to be far smaller than the basis set convergence error). Note that wavefunction calculations do *not* require a second PIST calculation. Also,  $M$  is small (typically  $\sim 2$  times the desired number of states) thus rendering explicit reorthogonalization feasible. As for the QMR component of PIST, it is hoped that preconditioning has reduced  $L$  to a manageably small value. As input for stage 3, users specify the number of (possibly combined) coordinates, the energy window over which rovibrational states are to be computed, and various other parameters as described above. An output file is generated that lists the computed rovibrational eigenvalues. Also, various optional data files may be written—as may be used, e.g., for wavefunction plotting purposes in Stage 4.

The optional Stage 4 is executed if wavefunction plots are desired. All of the requisite data may be found in the optional output files of Stage 3. However, this data is not presented in a form that would be useful for plotting via standard packages such as *Mathematica*. It is the purpose of Stage 4 to extract and output such information, for selected wavefunctions. Specifically, this module will output explicit values for the eigenstate wavefunction density, as a function of the four coordinates,  $R$ ,  $r$ ,  $\theta$ , and  $K$ . An optional summation over all  $K$  values can also be computed, as well as a transformation from Jacobi to hyperspherical coordinate systems.

The four stages described above are logical, and easy to use in practice. To date, even undergraduate and high school students (with some guidance) have been able to converge triatomic rovibrational state calculations using *ScalIT* as described above.

#### A.4 Applications

Although *ScalIT* can, in general, be used to solve a variety of physical problems, current application and development have been limited to calculating bound rovibrational spectra for triatomic systems. We give here only a few examples of the recent applications.

In a recent publication<sup>35</sup>, the bound states of the hydroperoxyl radical, HO<sub>2</sub>, were calculated up to the highest possible total angular momentum value,  $J = 130$ , corroborating and improving upon the studies previously performed by other researchers (up to  $J = 50$ ). Being a notoriously “floppy molecule”, HO<sub>2</sub> has remained a relatively difficult molecule to study, due to large coupling between rotational and vibrational degrees of freedom, and a deep potential well on the ground PES. Despite this, *ScalIT* was able to efficiently calculate states on a single CPU core in less time than previous studies on parallel platforms, although most calculations performed were done across multiple machines in even less time.

All rovibrational states were converged to an accuracy of  $10^{-6}$  eV or better (five or six digits of precision). For  $J = 50$ , a basis size of  $3.71 \times 10^5$  was used, one *fifteenth* of what was required by the previous study. Much of the basis set reduction was achieved through the use of the PSODVR in radial DOFs. Moreover, approximately 1500 total iterations were required to reach the above accuracy, compared to  $\sim 10^6$  required by Smith<sup>6-9;63</sup>. As one moves up the energy spectrum, the number of iterations required for convergence is increased, regardless of the iterative method employed. To this end, high lying states of  $J = 50$  were computed to test *ScalIT* in what the author considers to be the most difficult area of the HO<sub>2</sub> spectrum. These were seen to be the most computationally expensive calculations performed, due to the increase in QMR iterations per Lanczos from  $\sim 15$  to  $\sim 400$ . The necessary basis size only needed to be increased to  $1.08 \times 10^6$ , about a fifth of the basis size in the previous study for the low lying states. As  $J$  increases, the coordinate range is extended, and the number of relevant eigenstates reduced. At  $J = 120$ , there are only about 20 states for each parity, all of which are very delocalized. To achieve the same accuracy at this high-DOS regime, a basis increase of only  $\sim 8\times$  was required, and only slightly more QMR iterations were necessary. The HO<sub>2</sub> study has proven to be a testament to the efficacy of applying the *ScalIT* suite of codes to efficiently calculating bound rovibrational data to triatomic systems.

*ScalIT* has also been applied to a series of rare gas clusters<sup>11;26;27</sup>: Ne<sub>3</sub>, Ne<sub>2</sub>Ar, Ar<sub>2</sub>Ne, Ar<sub>3</sub>, as well as the neon tetramer, Ne<sub>4</sub>. Study of rare gas clusters in chemical physics gives insight to a variety of phenomena, including Van der Waals interactions, solvation processes, and phase change boundaries. Computationally, rare gas

clusters can be fairly accurately described by pair-wise potentials, obviating the development of a PES. Despite this, their inherent long range interactions yield extremely “floppy” behavior, and typically exhibit a high density of states, both contributing to the difficulty in computation. All rovibrational bound states were computed up to dissociation for each of the respective systems. Due to the relatively heavy nature of  $\text{Ar}_3$ , the difficulty of computing high lying states near dissociation is heavily exacerbated, yet was still accomplished with a modest computational allocation and will be the subject for an upcoming publication. The neon tetramer is currently under investigation by the author and will be, to the author’s knowledge, the most comprehensive rovibrational bound state calculation of rare gas clusters reported to date. This is the subject of Chapter 6

#### A.5 Conclusion

The poor performance exhibited from standard iterative sparse matrix solvers applied to the  $\mathbf{A}$  matrix has fueled the development of *ScalIT*. From the ground up, *ScalIT* has been developed to be a highly parallelizable, robust iterative sparse matrix eigensolver. Furthermore, because parallelization is applied at the level of the matrix-vector product, any level of the software suite can be utilized by the broader community, though we focus here on the high-level use of calculating rovibrational spectra for triatomic molecules. By following the procedure given above, a *non-expert* user can easily compute such spectra. *ScalIT* has been applied to many molecular applications, and has proven itself even in high-DOS regimes. *ScalIT* is available free of charge upon request to the authors.